Thin Film Edge Emitting Lasers and Polymer Waveguides Integrated on Silicon

by

Sabarni Palit

Department of Electrical and Computer Engineering
Duke University

Date:_______________________

Approved:

____
Nan M. Jokerst, Supervisor

____
Richard B. Fair

____
Tuan Vo-Dinh

____
April Brown

____
David R. Smith

Dissertation submitted in partial fulfillment of
the requirements for the degree of Doctor of Philosophy in the Department of
Electrical and Computer Engineering in the Graduate School
of Duke University

2010

ABSTRACT

Thin Film Edge Emitting Lasers and Polymer Waveguides Integrated on Silicon

by

Sabarni Palit

Department of Electrical and Computer Engineering
Duke University

Date:________________________
Approved:

____
Nan M. Jokerst, Supervisor

____
Richard B. Fair

____
Tuan Vo-Dinh

____
April Brown

____
David R. Smith

An abstract of a dissertation submitted in partial
fulfillment of the requirements for the degree
of Doctor of Philosophy in the Department of
Electrical and Computer Engineering in the Graduate School
of Duke University

2010

Abstract

The integration of planar on-chip light sources is a bottleneck in the implementation of portable planar chip-scale photonic integrated sensing systems, integrated optical interconnects, and optical signal processing systems on platforms such as Silicon (Si) and Si-CMOS integrated circuits. A III/V on-chip laser source integrated onto Si needs to use standard semiconductor fabrication techniques, operate at low power, and enable efficient coupling to other devices on the Si platform.

In this thesis, thin film strain compensated InGaAs/GaAs single quantum well (SQW) separate confinement heterostructure (SCH) edge emitting lasers (EELs) have been implemented with patterning on both sides of the thin film laser under either growth or host substrate support, with the devices metal/metal bonded to Si and SiO_2/Si substrates. Gain and index guided lasers in various configurations fabricated using standard semiconductor manufacturing processes were simulated, fabricated, and experimentally characterized. Low threshold current densities in the range of 250 A/cm^2 were achieved. These are the lowest threshold current densities achieved for thin film single quantum well (SQW) lasers integrated on Si reported to date, and also the lowest reported, for thin film lasers operating in the 980 nm wavelength window.

These thin film EELs were also integrated with photolithographically patterned polymer (SU-8) waveguides on the same SiO_2/Si substrate. Coupling of the laser and

waveguide was compared for the cases where an air gap existed between the thin film laser and the waveguide, and in which one facet of the thin film laser was embedded in the waveguide. The laser to waveguide coupling was improved by embedding the laser facet into the waveguide, and eliminating the air gap between the laser and the waveguide. Although the Fresnel reflectivity of the embedded facet was reduced by embedding the facet in the polymer waveguide, leading to a 27.2% increase in threshold current density for 800 μm long lasers, the slope efficiency of the L-I curves was higher due to preferential power output from the front (now lower reflectivity) facet. In spite of this reduced mirror reflectivity, threshold current densities of 260 A/cm^2 were achieved for 1000 μm long lasers. This passively aligned structure eliminates the need for precise placement and tight tolerances typically found in end-fire coupling configurations on separate substrates.

Dedication

Bharati Palit, the artist,

Debiprasad Palit, the engineer,

Sanmita, the earth warrior,

For helping me along, on my own calf-path through the woods.

And Pranav, the other confused kid.

Contents

List of Tables

List of Figures

Acknowledgements

I would like to thank Prof. Nan Jokerst for being such a supportive and positive PhD advisor. Our discussions have ranged from laser processing to paneer buys to positive bank balances to work-life balance, and I am grateful for the advice and help I have received for all these and more. This, in addition to her surviving a nerve and bone shattering jeep ride in a tiger and bear infested jungle, which, I must confess, I arranged.

Prof. David Smith is one of those eminent researchers one can't but help look up to (he is really tall and I am a puny 4'11.5"). I am also grateful to him for giving me many wonderful collaborative opportunities throughout the past 5 years, and ready access to computational resources. The intuition I like to think I have gained in some margin regarding semiconductor processing is because of Prof. Richard Fair's vast knowledge of device fabrication and the fun course he teaches on the subject. The first semester at Duke, I dropped Prof. April Brown's QM class, to only go back and request her to be on my committee. Prof. Tuan Vo-Dinh made me see the light (literally) in biomedical applications of photonics, and I hope for an opportunity to work on SERs with on-chip sources. I am grateful to all of these professors for being on my committee.

Dr. Sang-Yeon Cho, now at New Mexico State University, taught me all the good stuff both in the clean room and the laboratory. We had a great partnership; at least it was great for me, and he was too nice to suggest that it wasn't for him.

I have taken more classes from Prof. Adrienne Stiff-Roberts than anybody else's, not to mention all the other times I have asked her for help. Everyone hears about exploitation of graduate students, but she fits the now-not-at-all-ludicrous idea of "exploitation of a faculty member".

I couldn't have asked for better collaborators on the ARO-MURI grant that supported this project, than Prof. Luke Mawst and his students Dr. Gene Tsvid and Jeremy Kirch. Sorry, guys, but I am still catching up with your wafer-producing speed. Many thanks to them for the tremendous testing help as well. Prof. Kuech's inputs on the materials and thermal modeling were extremely helpful. Thanks also to Dr. Aloyse Degiron, Dr. Stephane Larouche and Dr. Yaroslav Urzhumov for simulation help.

Then, there are my ever suffering present lab-mates, Lin Luan, Matt Royal and Sulochana Dhar; and Feng Li from past days. They, including my office mates Heather Wake, Xin Cai and Arnak Aleksanyan have often been subject to the vagaries of my "mental state of the day". Thanks Matt and Sulochana, for all the useful discussions, and the Egyptian walk and ROTFL respectively. Mengyuan Huang pretty much put together the foundation for the Silvaco simulations during his Masters', and making it much easier for me to build on it. Thanks also to Dr. Talmage Tyler II for being such a good sounding board. There are my ECE buddies Vince Mao, Ashwin Wagadarikar, Shiuan Yeh Chen and Lingling Tang, to name only a few, the ones I am nice to. The list of generous ECE buddies I have been only nasty to in return, is too long to mention.

The SMIF folks at the Duke clean room, Dr. Mark Walters, Kirk Bryson, Jay Dalton and Michelle Gignac have been infinitely patient, immensely helpful, and now possibly equally relieved. Autumn, Tasha, Ellen, Kristen, Samantha and Heather have always been gracious about the paperwork I have kept throwing at them all these years. Thanks to Tom Napoles, for being the software installation go-to-anytime-guy.

Duke would not be Duke without Sathya Gopalakrishnan and Radhika Das. What happens when an environmental economist, an epigeneticist and an electrical engineer get together? Mostly only mayhem. Shoulders to cry on over failed experiments, Dain's to celebrate a success, and tea a bonus. Thanks also to Srinivas Rao Chadaram and Rupa Madalla, my de facto guardians in Durham. Thanks to Soumya, Harsha, Sujatha, Nilesh, Malavika, Sruti, Prachi, Sandeepa, for spoiling me rotten.

I must have done something right to deserve parents-in-law like Dr. Mridula and Dr. Dhirendra Swaroop Gupta (hopefully this is the last time I will commit the sacrilege of referring to them by name!). They and my sister-in law Swati have been constantly supportive during this long process, with my husband Pranav in Minneapolis and I in Durham, working on our respective PhDs. My uncle Prakash and aunt Jyoti Naik have been my biggest cheerleaders. Ma, Baba, sister Sanmita, and Pranav form the bedrock of my life.

Finally, I'd like to thank my guru, Shri P.K. Sardeshmukh Maharaj, who saw my future more clearly than I did, and convinced me to be an engineer.

1 Motivation and Scope of Thesis

Current research in photonic integration not only mirrors the electronic integrated circuit (IC) revolution of yesteryears, but goes beyond it by attempting to integrate both electronics and photonics on a common Si platform to provide new levels of functionality. While it may be possible to utilize a single material to fulfill the requirements of light emission, distribution, modulation and detection, along with electrical signal propagation and processing [1], it is next to impossible ensuring that each of the components of such a system are individually well-optimized . This necessitates co-locating multi-material, multi-functional components in close proximity in a planar fashion. The planar integration of active photonic components such as compound semiconductor lasers, detectors, and modulators; and optical devices based on polymers and inorganics such as couplers, splitters, and gratings onto Si or Si CMOS electronic platforms have a plethora of applications ranging from optical interconnects and signal processing [2-7] to environmental/biological/chemical sensing [8-11].

1.1 Motivation

One of the biggest bottlenecks in the field of photonic integration is the availability of efficient on-chip light sources. Direct bandgap compound semiconductor light emitting materials are the most efficient light emitting materials, however, Si is an indirect bandgap semiconductor that has not demonstrated efficient lasing. To use light on Si or Si-CMOS systems, a great deal of effort has been directed towards determining efficient methods and materials for coupling off-chip sources with on-chip photonic components and circuitry. These span grating couplers [12, 13], tapered and lensed fibers [14, 15], tapered waveguides [16, 17], and spot size converters [18] .

Efforts at integrating on-chip light sources have included methods ranging from bump or flip chip bonded bulk devices [17, 19-22] to heteroepitaxial growth [23-29]. Bump-bonded or flip chip bonded devices are not amenable to planar integration with endface coupling due to the difference in height (50-100 μm) between the laser and the waveguide. Strategies for recessed devices or vertical coupling (gratings, mirrors) are needed. A notable exception to this are flip chip etched facet lasers integrated with fibers at the board level [30], which has the potential for thin film implementation and waveguide integration. However, etched facets with reflectivities comparable to cleaved facets require very stringent process parameters for each material. Heteroepitaxial growth, on the other hand, would be most amenable to planar implementation. However, strategies such as metamorphic/graded buffer layers and low temperature processing to reduce the density of misfit and threading dislocations due to lattice and thermal mismatch have not led to an epitaxial structure on Si that efficiently lases for more than 8000 hours, and that too only with the incorporation of tens of microns of buffer layers [29] . As a comparison, bulk III-V lasers have between 20000 to 100,000 hours of lifetime [31, 32]. These defects lead to dark line defects, surface states/traps at the material interfaces and reduced device lifetime and reliability. The incorporation of graded buffer layers is a complex process that needs to be repeated and individually characterized for each material system that is required to be grown on the substrate.

A middle route is heterogeneous (also sometimes called hybrid integration), which involves the integration of thin layers of compound semiconductors bonded to a host substrate. These substrates include Si, silicon-on-insulator (SOI), SiO_2, glass and ceramics; and bonding techniques including wafer bonding or bonding agents such as metal or adhesives [33-36]. Using these approaches devices of different material systems can be integrated without regard to lattice matching. In the specific case of heterogeneous integration, as pursued in this thesis, devices can be processed (fully or partially) and optimized while on the growth substrate, and then transferred to the final host substrate, where processing and integration with other optical devices can take place.

Details on the different approaches to heterogeneous integration of III-V lasers on silicon are found in Chapter 2. To summarize, the requirement of a low threshold density, simple cleaved facet thin film edge emitting laser integrated onto Si that does not compromise system level strategies for thermal management, and that can also be integrated with other planar optical devices on the same substrate, was a challenge that had not been met, and is addressed in this thesis.

1.2 Objective and Organization of Thesis

The objective of this research is to model, fabricate, and experimentally characterize metal/metal bonded heterogeneously integrated, thin film, cleaved facet strained single quantum well III/V edge emitting lasers onto Si substrates. The goal is for these thin film lasers to have low threshold current densities, while still enabling planar and passively aligned integration with polymer waveguides on the same Si substrate.

Chapter 2 discusses the techniques used by researchers for the heterogeneous integration of thin film III-V lasers and lasers with waveguides on Si. In Chapter 3, the concepts related to low threshold current density thin film edge emitting lasers are discussed, along with a description of the strain compensated InGaAs/GaAs single quantum well epitaxial structure utilized for the lasers in this research. Chapter 4 describes the fabrication processes associated with top and bottom stripe gain guided lasers, with and without broad area metal/metal bonding with silicon, followed by a discussion of simulations in Silvaco™. Two types of index guided structures, namely, the p-ridge n-broad area laser, and the slotted p-ridge n-stripe laser, are discussed in Chapter 5. In Chapter 6, the integration of edge emitting lasers with polymer waveguides on SiO_2/Si is detailed. Concluding remarks and recommendations for future research directions are covered in Chapter 7. Detailed fabrication recipes and code for the simulations are in the appendices.

2 Heterogeneous Integration of Lasers and Waveguides on Silicon

This chapter reviews the methods and the performance of heterogeneously integrated lasers and waveguides on silicon as implemented by other researchers in the field. Section 2.1 briefly describes the two standard structures for Fabry Perot resonator lasers: Edge emitting lasers (EELs) and vertical cavity surface emitting lasers (VCSELs). In Section 2.2.1 some instances of thin film VCSEL integration are given. Section 2.2.2 presents a detailed discussion of some of the heterogeneous methods for thin film edge emitting laser integration on Si or SiO_2 and the associated literature. Section 2.3 discusses the integration of lasers and waveguides on silicon.

2.1 III-V Fabry-Perot Resonator Lasers

The two main types of Fabry-Perot cavity lasers are edge emitting lasers (EELs) and vertical cavity surface edge emitting lasers (VCSELs), as illustrated in Figure 2-1 [6]. In EELs, the cleaved edges (facets) of the device form the mirrors for the resonator. Light is emitted from these cleaved end facets of the device. For a VCSEL, the mirrors are formed by two sets of reflectors, typically distributed Bragg reflectors, which are created at the time of epitaxial growth or post-deposited on the laser.

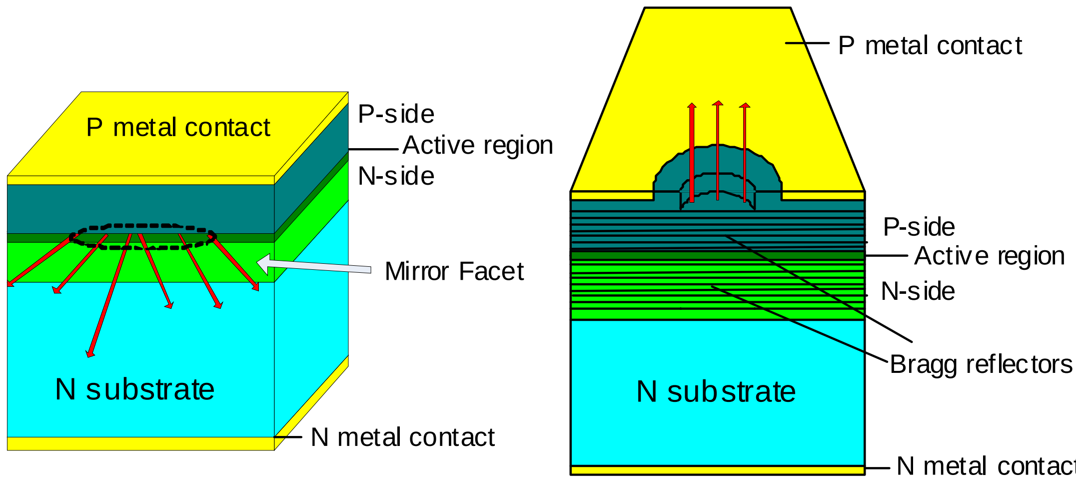

Figure 2-1. (a) Edge Emitting Laser; (b) Vertical Cavity Surface Emitting Laser [6].

2.2 Thin Film III-V Lasers Bonded to Silicon

Research efforts into the heterogeneous integration of III-V lasers onto Si have been directed towards both VCSELs and EELs, as both types have some advantages (and disadvantages) in terms of fabrication and laser performance. VCSELs permit testing at intermediate fabrication steps and simultaneous transfer of arrays of devices. However, they need beam turning optics, since the light emission is perpendicular to the surface of the laser. VCSELs have traditionally been low power, and, while the temperature dependence on wavelength is weak, the high series resistance causes significant heating and dependence of resonance wavelength on current [37]. Drawbacks to EELs include the need to be cleaved, and this makes array integration more difficult than for VCSELs. However, EELs have fewer layers in their epitaxial structures; have good power and thermal characteristics over a wide range of wavelengths and currents, provide in-plane emission, and are capable of very high power.

2.2.1 Vertical Cavity Surface Emitting Lasers Integrated onto Silicon

To provide a complete review of thin film laser integration techniques and the corresponding effect on laser performance, it is necessary to provide a complete picture of the field of III-V Fabry Perot laser integration on Si, which includes both VCSELs and EELs. Thus, a short discussion of the integration of thin film VCSELs onto Si is included herein. A great deal of effort is being directed towards higher power [38] and longer wavelengths [39, 40], which are attractive development in VCSEL technology. Thus, the heterogeneous integration of VCSELs on Si and Si-CMOS substrates is expected to become an active area of research.

Heterogeneously integrated VCSELs on Si have been demonstrated both with simultaneous transfer of an array of processed VCSELs, as well as sparse integration (individual pick and place of devices). Techniques involve flip-chip metal bonding [21, 41, 42], and polymer wafer bonding to a silicon substrate [43]. Substrate removed VCSELs have almost 40% less thermal resistance compared to VCSELs on their growth substrate [44].

In the case of flip chip metal bonding, the VCSELs were processed while still on the GaAs growth substrate [41, 42]. This preprocessed array of lasers was then bonded to a Si circuit patterned with metal pads, as shown in Figure 2-2 (a, b), followed by substrate removal. The dynamic resistance value of 30 Ω in the case of metal bonded VCSELs, shown in Figure 2-2 (a), integrated on small-diameter electroplated posts in

[41] was found to be equal to that of commercial unbonded VCSELs. In the case of large area metal bonds, as shown in Figure 2-2 (b) both the threshold current densities and the differential resistance were found to be lower after the substrate removal and bonding process [42] with a change from 77 A/cm^2, 60 Ω to 22 A/cm^2, 35 Ω respectively. Polymer bonded VCSELs in Figure 2-2 (c) started by bonding a GaAs epitaxial wafer to silicon using polyimide or epoxy as an adhesive. The substrate was etched away, and then the VCSELs were fabricated [41, 43]. In this case the thermally and electrically non-conducting polymer interface caused the thermal resistance go up by 1.8 times as compared to VCSELs left on their GaAs substrates [43], and the dynamic resistance and threshold voltage was doubled [41]. These results indicated that the substrate removed, large area, metal/metal bonded VCSELs have the best performance characteristics. However, low-temperature bonding may be required to prevent thermal stresses due to the different coefficients of thermal expansion for the III-V wafer and the Si or Si CMOS substrate.

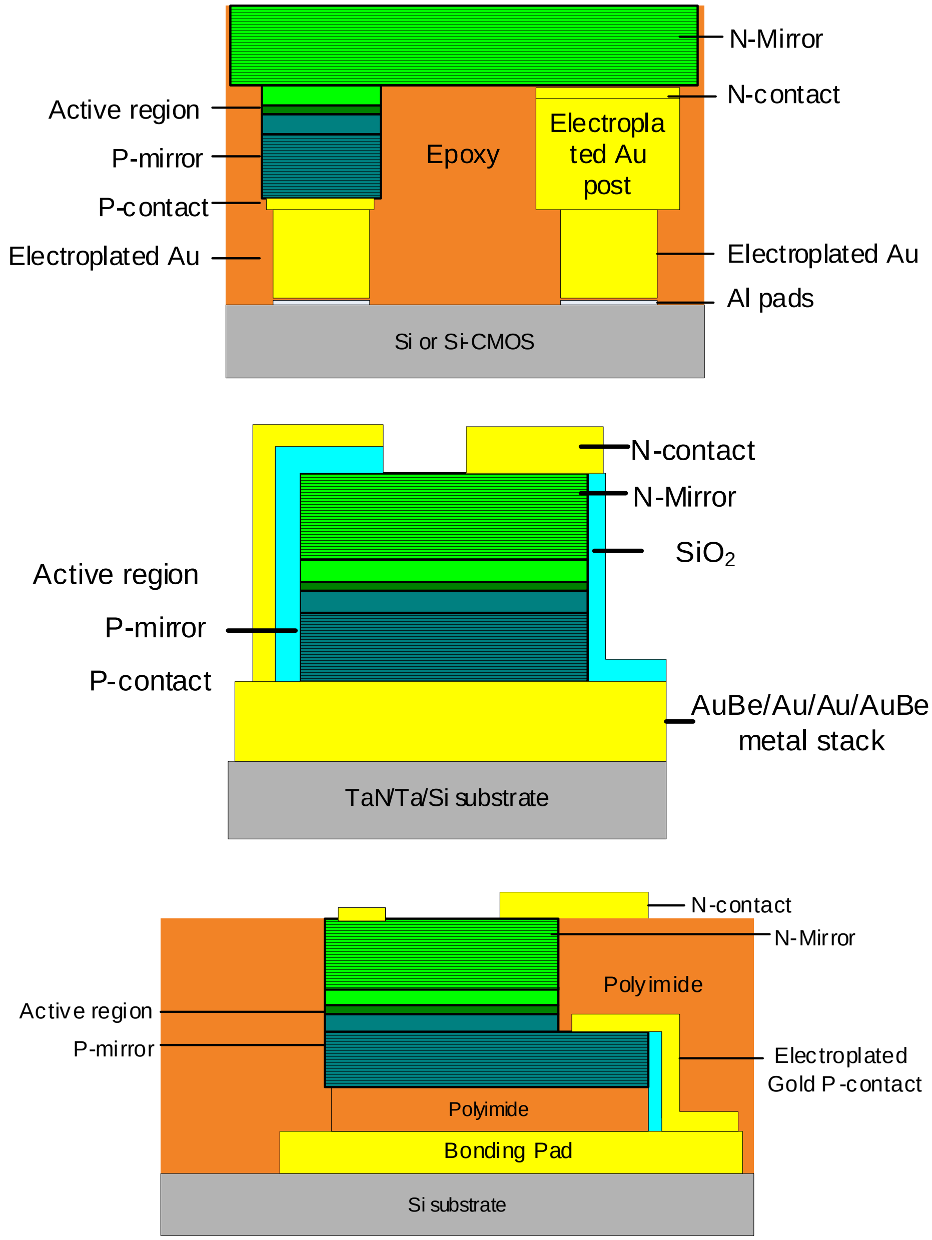

Figure 2-2. Integration of thin film VCSEL arrays on silicon: (a,b) Flip chip metal bonding [41, 42] and (c) Polyimide bonding [43].

Another method that involved preprocessing of the VCSELs is very similar to the sparse integration process to be used in this thesis. In the first case, The VCSELs were bonded to a transfer film with a weak adhesive, followed by substrate removal.

These VCSELs were then positioned and transferred onto polymer adhesive close to a metal pad on Si, and then the device and pad were interconnected using conductive paste [45]. Both differential resistance and the optical power degraded after the thin film laser integration process, and can be attributed to the polymer interface. In the second case also, as shown in Figure 2-3, the p-side of the VCSEL was preprocessed and mesa-etched down to an etch stop layer, followed by encapsulation in a polymer. The substrate was removed, and the n-side was metallized, followed by removal of the polymer material. Using a vacuum pick and place technique, these lasers were integrated into metallized recesses in Si. This was followed by a polymer and SiO_2 encapsulation and planarization, etching, and metallization to connect the devices [46]. The threshold currents remained unchanged, and a 28% reduction in thermal resistance was observed for the thin film VCSELs. This again stressed the importance of using metal as a bonding interface. Also, this highlights that the device handling technique can have an impact on the reliability of the laser.

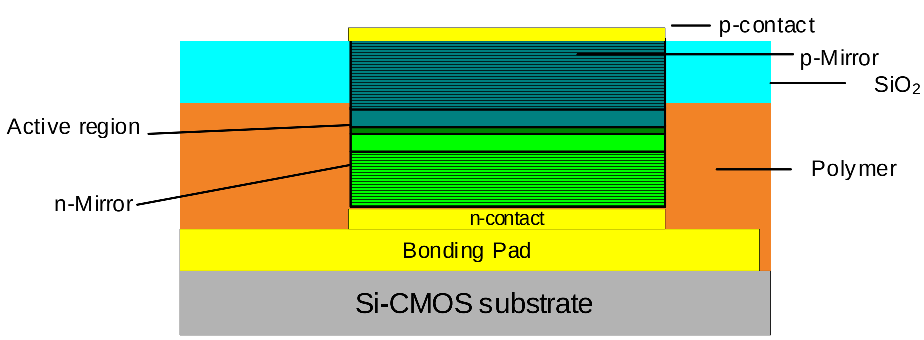

Figure 2-3. Sparse integration of thin film VCSELs on Si-CMOS substrates [46].

VCSELs are attractive from the perspective of test and validation during intermediate steps of the device fabrication process, and also provide a circularly symmetric mode, with narrower linewidths for efficient coupling with optical fibers. However, many more epitaxial growth steps are involved (primarily due to the Bragg mirrors), and beam turning optics need to be incorporated into the photonic circuit to guide light parallel to the surface of the substrate. Also, most VCSELs operate at low powers in the range of tens of mW [47, 48] although some recent advances report VCSEL operation in the range of hundreds of mW to couple of watts for CW operation [38, 49, 50]. In comparison, commercial EELs can emit 20 W CW power at the same wavelengths, i.e. λ=980 nm [51].

2.2.2 Edge Emitting Lasers Integrated on Silicon[1]

There are two approaches to thin film edge emitting laser integration onto silicon, following principles similar to thin film VCSEL integration. The first is the direct bonding of thin film materials and devices to the host substrate, using wafer bonding [35, 52] or with an intermediate layer or layers, such as metals or adhesives [3, 53]. In the cases where intermediate bonding layers are used, the laser or the substrate or both may have the intermediate metal or adhesive [54, 55]. In all cases, a transfer medium

[1] This section appears in a modified form in: N. Jokerst, S. Palit, J. Kirch, G. Tsvid, L. Mawst, T. Kuech, "Thin Film III-V Edge Emitting Lasers Integrated Onto Silicon," in *Proc. SPIE*, 2010, vol. 7616, San Francisco, CA, pp. 76160S 1-12.

can also optionally be used to transport, separate or support processing steps, before or after the substrate is removed.

Direct bonding of the laser material is typically achieved through wafer bonding [52, 56]. Adhesive bonding uses a polymer that acts as an adhesive between the two materials [34]. In the first variation of these processes (Figure 2-4) [34, 52, 56], the bonding occurs first, and then the growth substrate is removed by lapping and/or selective etching. This usually does not require a transfer medium (a carrier for transferring the thin film device). The device is then processed from the newly exposed side of the epitaxial layer. This process typically results in both p and n metal contacts on the same side of the laser, leading to non-optimal current confinement. For EELs, this processing is followed by inductively coupled plasma (ICP) / reactive ion etching (RIE) or cleaving of the laser facets. Etched facets enable planar integration with other optical components on the same substrate. However, threshold current densities are typically high due to higher mirror losses. If the facets are cleaved then the Si substrate is cleaved as well, resulting in EELs that are similar to a laser with the growth substrate, again preventing further integration on the same Si platform.

Continuous wave (CW) results on InGaAsP double heterostructure (DH) lasers have been obtained by wafer bonding the epitaxial material to Si using the procedure outlined in Figure 2-4, resulting in a threshold current density of 2.1 kA/cm^2, [35]. Atomic rearrangement (contact bonding with annealing) was used for integrating

InGaAs/GaAs triple quantum well epitaxial material to Si, with a resulting 1.2 kA/cm^2 threshold current density in pulsed mode (with very high series resistance at the interface), and double the threshold current density under CW conditions [57].

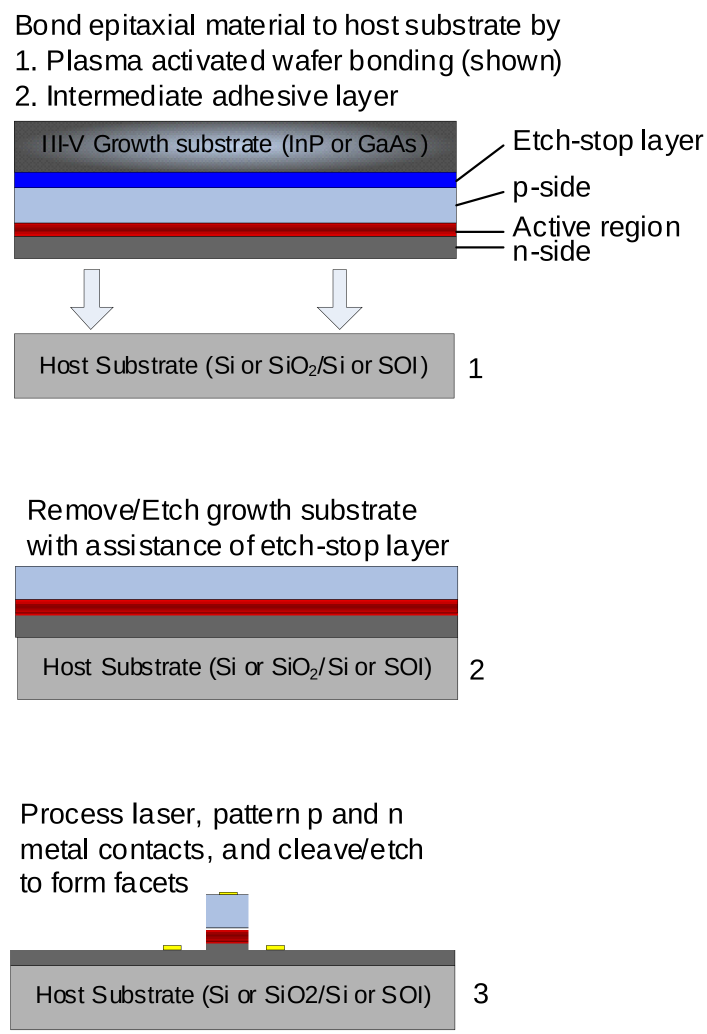

Figure 2-4. Fabrication process for one-side contact thin film EEL integrated on SiO_2/Si without transfer medium (drawing not to scale); (1) Bonding of the epitaxial EEL structure with growth substrate to the host SiO_2/Si substrate; (2) Selective removal of the EEL growth substrate; (3) Processing of the thin film EEL structure to create a laser.

Adhesive bonding can be used to bond very dissimilar semiconductors without consideration for lattice mismatch and orientation. However, when it is used to bond unprocessed wafers, then all subsequent device processing steps are limited to the temperature limitations imposed by the bonding materials, to prevent re-flow or destruction of the polymer or adhesive.

In the second reported variation of the bonding process, as shown in Figure 2-5, the laser material was preprocessed into a device and transferred to the host substrate. The p-stripe and ridge were patterned and etched down to the n contact layers of the laser epitaxial material. The exposed n-layer was then patterned and metallized, followed by etching mesas down to an etch-stop layer to define the laser bars. These lasers were encased in a protective coating (e.g. Apiezon W), and the substrate was removed by selectively etching the substrate entirely off (e.g. GaAs substrate etched off to reach an InGaP etch-stop layer or an InP substrate etched off to stop at an InGaAs etch-stop layer), or preferential etching of an intermediate layer (e.g. $Al_xGa_{1-x}As$ $x>0.4$, with respect to the GaAs substrate). The laser bars were then transferred to a flexible Mylar® transfer diaphragm. The Apiezon W was dissolved away in a chlorinated solvent, resulting in thin film laser bars weakly bonded to the Mylar®. Next, the thin laser bars were flexed to cleave facets in the laser along photolithographically defined wedges. The EELs were then transferred to a host SiO_2/Si substrate. In a recent demonstration of this process on single side contact InP/InGaAsP-based multiple quantum well (MQW) SCH index-guided EELs, a threshold current density of 4.44 kA/cm^2 in pulsed mode was reported [53]. This high threshold current density may be attributed to the contacts for the p-ridge and the n-side both being on the same side, which results in a non-ideal current path.

A variation in this process has also been reported, in which the laser bars were cleaved after preprocessing, and then encapsulated in Apiezon W, after which the growth substrate was removed by selective etching of an AlAs etch stop/selective etch layer in a HF solution. In an early implementation for a GaAs/AlGaAs DH laser, this method was followed [58]. These lasers were bonded with optical cement to a glass substrate. The handling of such small thin film laser dies supported by Apiezon W is a challenge, although these early double heterostructure EELs had a threshold current density in pulsed mode of 1000A/cm^2 that remained unchanged after the substrate separation procedure, indicating that thin film processing did not lead to any structural damage. However, this fabrication methodology has the limitation that all the layers of the epitaxial structure need to be chemically non-reactive with the HF etching solution, as they are exposed on all 4 sides (except the top side, which is covered in Apiezon W), and this limits the choice of materials. This first implementation, however, laid the foundation for sparsely integrated thin film lasers on Si.

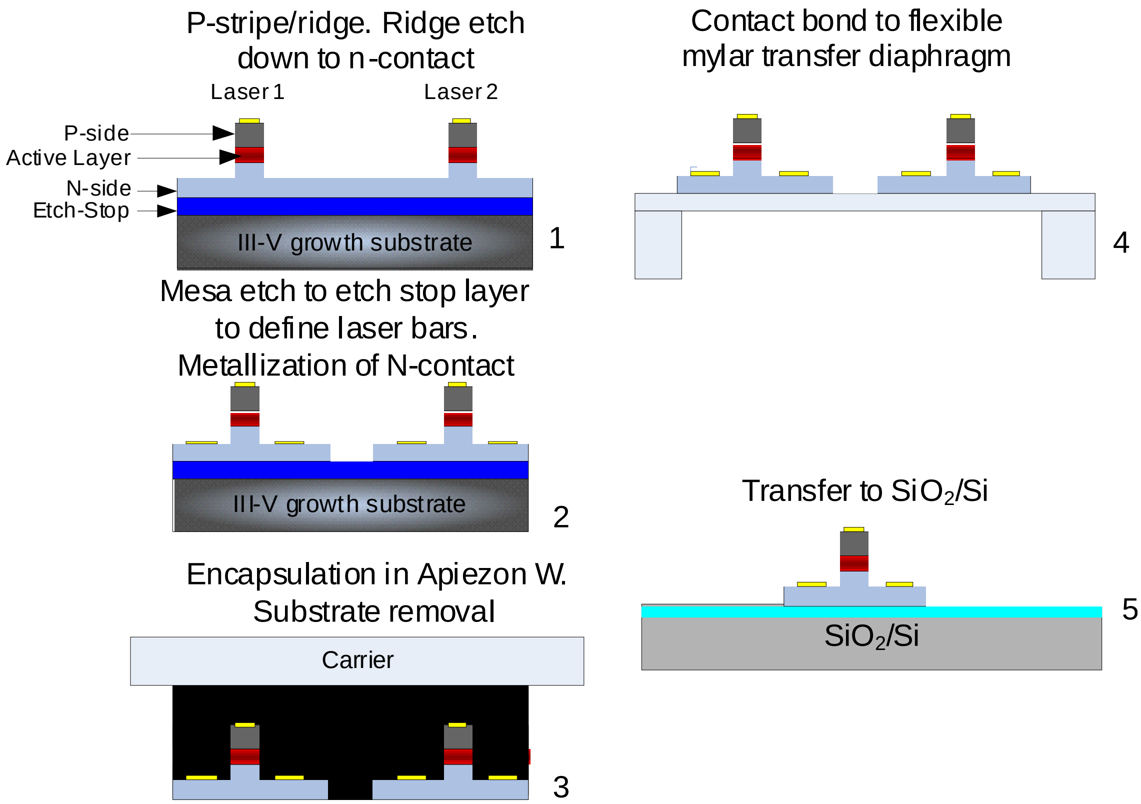

Figure 2-5. Fabrication process for integration of preprocessed lasers with one-side contact onto a host substrate (SiO_2/Si) with the assistance of transfer medium (drawing not to scale): (1) Definition of the p-type contact and ridge etch down to the n-type contact epitaxial layer; (2) Metallization of the n-type contact and the mesa etch to define the bars of the lasers (bars extending in and out of the paper); (3) Application of an Apiezon W protective layer to prevent etching of the EEL epilayers during substrate removal, application of carrier/handle mechanical support, and selective substrate removal; (4) Bonding of thin film EEL bars to a Mylar® transfer diaphragm, and flexing of the diaphragm to create cleaved facets in the lasers; (5) Transfer of individual EELs to host SiO_2/Si substrate [53].

For both wafer level bonding and preprocessed device adhesive bonding, rapid thermal annealing (RTA), which involves high temperatures and is commonly used to form ohmic contacts, will usually prove to be a challenge once the bonding is done, due to difference in coefficients of thermal expansion and material sensitivity at high temperatures. This should not prove to be a problem when a metal/solder layer is used at the interface instead.

Metal contacts on both sides of the laser are more desirable from the perspectives of current distribution and heat dissipation. Such contacts are enabled by metal/metal bonding. Simulations of thin film EELs indicate that better heat removal is possible if a top and bottom contact with heat sinks on both sides is used for the thin film laser [54]. This is also consistent with reports that indicate that a reduction in laser thickness from 100 μm to 6 μm results in a drop in the temperature difference between the junction and heat sink from 50 °C to 3 °C [59].

In one reported variation of a metal/metal bonding process, bare EEL epitaxial wafers were metal/metal bonded to metallized SiO_2/Si [54], following the procedure in Figure 2-6. Depending upon whether the epitaxial growth structure is p or n-side on top (typically p is on top), the laser material may be metallized and bonded p-side down or n-side down to the metallized host substrate. This forms one contact. The growth substrate is then removed, the laser processed, and the other contact is patterned. The structure is then cleaved to form facets, which again causes the Si host substrate to be cleaved, preventing further planar integration on the same Si platform.

A 980 nm graded index (GRIN) separate confinement heterostructure (SCH) strained quantum well (SQW) InGaAs/GaAs was utilized to demonstrate a thin film ridge (index-guided) laser that consisted of bonding the released preprocessed epitaxial layer to a Au-Pd coated silicon substrate [60]. The back side of this highly doped silicon substrate was then metallized to access the n-contact, the integrated device was cleaved, and a threshold current density of 740 A/cm^2 was measured [60]. Since the thin film III-V material was not metallized, and was only van der Waal's bonded to the metallized Si, one would expect a high series resistance in this implementation. However, a good ohmic contact was formed after bonding and annealing [61]. This implementation involved a 30 minute anneal at 400 °C on the bonded structure, but no delamination due to the different coefficients of expansion of the III-V material and the Si substrate was reported. This supports the efficacy of using a metal interface layer, as pursued in this thesis. Such high temperatures cannot be used in the wafer bonding of III-V materials and Si [62]. More recently, a metallized InP epitaxial wafer was bonded to a metallized silicon substrate, followed by processing to create a typical ridge laser. The threshold current densities of the thin film ridge lasers were degraded due to current spreading as compared to conventional broad area lasers, but there was a 3 fold improvement in the thermal resistance [54]. In both these cases, the cleaving of the lasers was performed after bonding to the host substrate, resulting in a laser that was no longer thin film in structure. Consequently, integration (planar or otherwise) with other photonic components on the same (cleaved) Si substrate is very difficult. So, while these implementations indicated the importance of a metal bonding layer, they made the case for research into preprocessed metallized and cleaved lasers that are integrated onto metallized substrates, so that planar integration with other photonic devices would still be possible.

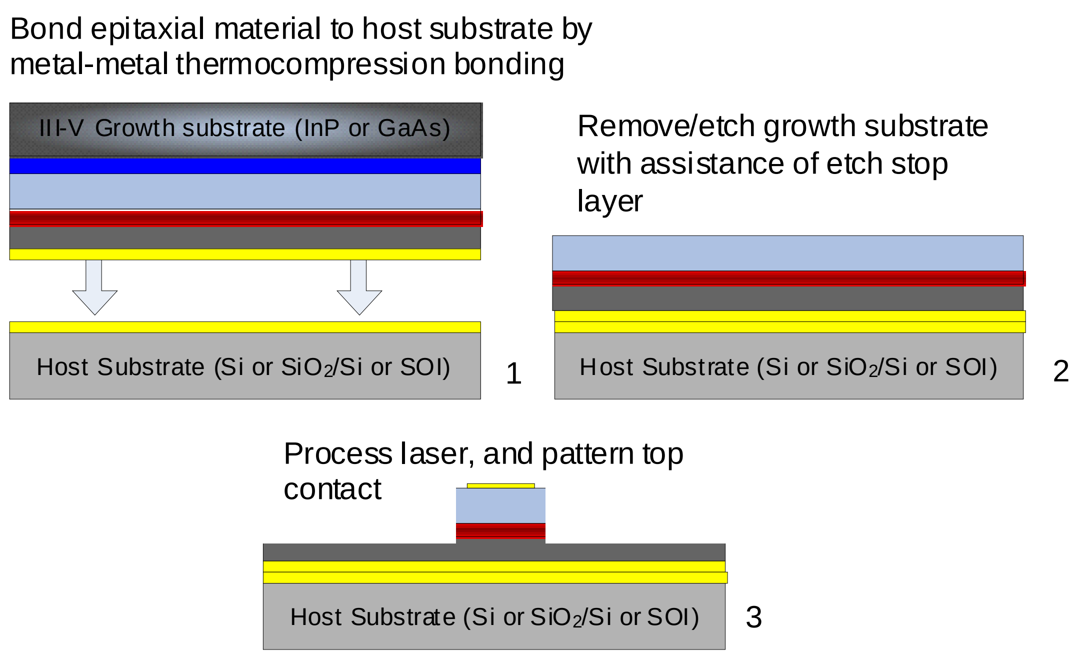

Figure 2-6. Fabrication process for a two-side contact thin film EEL integrated on SiO_2/Si based on bonded epitaxial wafers (drawing not to scale): (1) EEL epitaxial structure is metal/metal bonded to the host substrate; (2) Growth substrate is selectively removed from the EEL; (3) Fabrication and definition of the EEL. Host substrate is cleaved with the EEL.

It is also possible to integrate pre-processed EELs with top and bottom metal contacts with [55], and without a transfer medium [63], as shown in Figure 2-7. Typically the p-stripe or ridge and any associated electrically isolating layers are patterned prior to substrate removal. After this, it is possible to blanket deposit the n-type contact while the EEL structure is still encapsulated in Apiezon W [55], or a protective polymer [63], as shown in Figure 2-7. The EEL is then transferred using a diaphragm [55] or a micropipette to metallized Si or SiO_2/Si [63].

In [64], the first implementation involving cleaving of thin film lasers using photolithographically defined grooves, also called wedge facet cleaving, was reported. A threshold current density of 640 A/cm^2 was measured in pulsed mode for a broad area graded refractive index (GRIN) separate confinement heterostructure (SCH) GaAs/AlGaAs SQW ridge laser integrated on Si. An unstrained InP/InGaAsP two-sided contact laser at λ=1550 nm was implemented [55]. This EEL was a gain guided stripe laser, but with a very low injected threshold current density of 166 A/cm^2. This laser utilized the wedge cleaving procedure, and the thin film lasers were integrated with waveguides and other devices on a Si or SiO_2/Si platform. The cleaving process in both cases was done by the adhesion of the laser bars to a flexible metal carrier with wax, which then had to be dissolved. The dissolution of wax displaces the devices from the metal carrier, potentially causing them to float in solution, reducing yield and making the transfer process more difficult. Also, in both cases, the n-side metallization was done while the thin film devices were embedded in Apiezon W. The broad area metallization connects all the laser bars together, so the n-side metal is subject to damage when the laser bars are cleaved, preventing the formation of a well-defined n-contact. In addition, this metallization step is not reliable, as high metal evaporation chamber temperatures can cause the encapsulating Apiezon W to melt, damaging the thin film lasers.

The metal/metal bonding of pre-processed thin film lasers bonded to Si is very promising, as evidenced by the CW results for thin film EELs [63]. EELs operating at λ=1550 nm were processed on the p-side to form ridges, planarized with benzocyclobutene (BCB), embedded in a spin-coated polymer, and the substrate was removed. The n-side was photolithographically patterned over a broad area, metallized, and then the thin film lasers were cleaved along photolithographically patterned wedges by sonication. A micropipette pick-and-place technique was used to bond the lasers onto a metallized Si substrate, and CW operation was verified, as well as pulsed mode operation for temperatures up to 80 °C. Performance characteristics for these integrated thin film lasers were superior to identically structured lasers left on their InP growth substrate [63]. Ridge lasers with similar structures have been implemented herein [65], and predate the above research. The use of a polymer such as BCB to planarize the p-side has device reliability implications, as delamination may occur in subsequent high temperature steps, such as during a RTA step. In addition, the cleaving process using sonication and micropipette based pick-and-place result in free standing thin film devices in fluid, potentially leading to device damage. As in previously discussed cases, releasing the lasers in solution results in no control over the initial location of the cleaved lasers prior to transfer, limiting options for automation, or simultaneous transfer of multiple devices. In this dissertation, efforts were made to realize reliable cleaving without allowing the laser to be free standing at any point, and using standard semiconductor device handling equipment (such as thermal release tape).

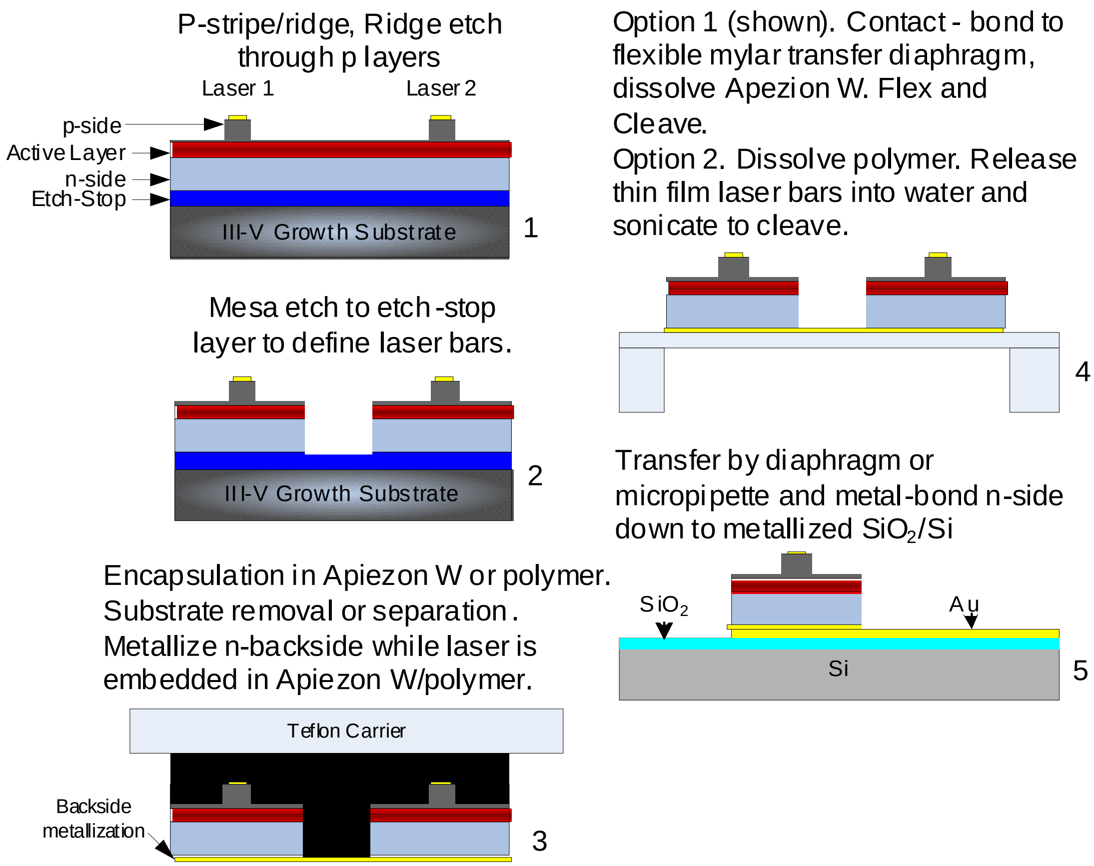

Figure 2-7. Fabrication process for two-side contact preprocessed thin film EELs integrated onto SiO_2/Si (drawing not to scale): (1) Definition of ridges and stripe contacts on EEL structure on the growth substrate; (2) Mesa etch to define the EEL bars; (3) Selective substrate removal; (4) Bonding to a transfer medium, with EEL cleaving options; (5) Transfer to a metallized Si or SiO_2/Si host substrate.

2.3 Thin Film III-V Edge Emitting Lasers Integrated With Waveguides Onto Silicon[2]

The heterogeneous integration of thin film laser diodes with waveguides has been pursued both for the purpose of mode conversion for interfacing with a butt-coupled single mode fiber, as well as for on-chip waveguide coupling and planar integration. Edge emitting laser diodes can butt-couple to a rectangular waveguide, with varying coupling efficiencies. Theoretically and experimentally validated results for a GaAs laser with a light emitting layer as thick as a butt-coupled Ta_2O_5 (n=2) slab waveguide showed that at least 90% coupling of the fundamental mode is possible, albeit with very high precision piezoelectric micrometers to achieve tolerances of 0.1 μm [66]. Reducing the thickness of the light emitting layer with respect to the waveguide thickness can enhance the coupling efficiency further. However, the even larger divergence of the beam for quantum well lasers makes it imperative for the waveguide to be placed as close as possible to the laser facet (<0.1 μm), as the most sensitive parameter to the coupling efficiency is the distance between the laser facet and the waveguide facet. The coupling efficiency goes through a series of maxima and minima as the distance is varied due to Fabry Perot reflections between the laser and waveguide facets, with a 5%-20% variation in power depending on the material composition [66].

---

2 This section appears in a modified form in: N. Jokerst, S. Palit, J. Kirch, G. Tsvid, L. Mawst, T. Kuech, "Thin Film III-V Edge Emitting Lasers Integrated Onto Silicon," in *Proc. SPIE*, 2010, vol. 7616, San Francisco, CA, pp. 76160S 1-12.

Overall efficiencies drop below 50% for a 3 μm gap. Tapered waveguides have also been pursued for mode conversion from an EEL to a single mode fiber (SMF). Using tapers, a 50% coupling efficiency between a polymer waveguide taper and an EEL, and 25% coupling between an EEL and an SMF has been achieved with large alignment tolerance [16] . A spot size converter, following the same principle of tapers, but implemented with the laser semiconductor material, was used to interface to an SMF with 50% coupling efficiency [67].

The integration of a thin film laser with a waveguide on the same substrate is the first step toward chip scale planar photonic integrated systems. Efforts in this direction have been made with both polymer [2, 55, 68] and SiO_2 waveguides[69], and with some SOI implementations [3, 5]. In [68], laser integration was implemented using a polymer slab waveguide on Si, which was etched away on one side. Bars of laser arrays were processed while on the growth substrate with both p and n-contacts on one side. These arrays were then cleaved, the top side encapsulated in Apiezon W, and the substrate was removed by epitaxial liftoff. Channel waveguide were defined by photo-bleaching. A relatively high J_{th}=740 A/cm^2 was obtained for 5 μm laser ridges. This method enabled processing on only a single side of the laser, thus increasing the threshold current, limiting the choice of materials in the epitaxial layer as the sides of the laser bar were not encapsulated, and the handling of individual devices encapsulated in Apiezon W was difficult. In addition, precise control over the thickness of both the core and cladding polymer layers is required to enable good vertical alignment with the waveguides.

A similar method was used wherein a glass waveguide was etched to form a recess into which small laser dies were inserted and metal bonded [69]. The substrate was then etched off, and the top-side patterned. These GaAs/AlGaAs MQW bonded lasers had etched facets with low reflectivity, leading to high threshold current densities of 6.3 kA/cm^2. Also, vertical alignment was an issue, with a mismatch of up to 1 μm.

An integrated thin film laser, a polymer waveguide and a thin film photodetector were integrated onto silicon using transfer and sparse integration [2]. The laser and photodetector were optimized and processed on their separate growth substrate, their substrates were removed, and the devices were then transferred to the silicon host substrate by means of transfer diaphragms. This implementation consisted of lasers which had contacts on the same side, which leads to less efficient current pumping and higher threshold current densities of 4.44 KA/cm^2.

An integrated system based on low temperature polymer (BCB) bonding of an InP/InGaAsP MQW epitaxial wafer to an SOI substrate has also been demonstrated [3]. After bonding, the laser substrates were removed and the III-V lasers and detectors were then processed. The laser facets were formed by dry etching. This was followed by the fabrication of a reverse waveguide taper in the silicon on insulator (SOI) host substrate, and a polyimide waveguide on top of the taper to couple light into the endface coupled

III-V device. The etching of the polyimide waveguide and III-V ridge was done in the same process step. Again, in this case, the etched laser facets and single side contacts led to high threshold current densities of 10.4 kA/cm^2 [70], and the lowest threshold current density, even for lasers bonded on GaAs and then cleaved, was 2.6 kA/cm^2 [34]. The BCB adhesive layer between the SOI and the III-V layer increased the thermal impedance of the laser, preventing CW operation. The authors projected that thick metallization would be required for sufficient heatsinking to achieve CW operation.

In another implementation of low temperature wafer bonding, a III-V MQW-SCH epitaxial wafer was bonded directly to a Si/SiO$_2$ waveguide in an SOI platform, the InP growth substrate was removed, and the laser defined, followed by dicing the structure into small pieces, to form the end facets of the lasers [5, 52, 56]. The evanescent mode of the laser coupled into the Si waveguide below it. Threshold current densities as low as 871 A/cm^2 were reported, among the lowest reported for thin film MQW lasers integrated on Si [5, 52]. However, this is a single side contact laser. The thermal impedance of this integrated EEL was compromised due to the thermally non-conductive SiO$_2$ layer over most of the laser interface and thermal impedance values of 42 °C/W were obtained. For the same lasers, pulsed mode operating temperatures of 50 °C have been reported for 1550 nm thin film Fabry Perot lasers, and for 1310 nm, operating temperatures up to 65 °C and 105 °C for fundamental and second transverse mode thin film lasers have been reported [52, 56]. Thus, while the thin film EEL bonded to an SOI waveguide is self-aligned to the waveguide, heat dissipation continues to be an issue [71]. Efforts to mitigate these thermal issues include the introduction of metal from the sides in the Si layer of the SOI substrate, below the n-contacts [72] . The metal bond does not extend to below the active region of the laser, and although room temperature pulsed operation was obtained for this distributed feedback (DFB) laser implementation, the threshold current density of 2.9 KA/cm^2 is much higher than the DFB implementation of Fang et. al. [73]. There is also a limit to the reduction in threshold current density that can be achieved for this structure, as most of the optical mode resides in the Si waveguide rather than in the III-V wells, reducing the optical confinement factor (overlap of electrical and optical mode) of the lasers. Given this limitation with evanescent coupling, and due to the electrical and thermally non-conducting interface formed by bonding the laser to oxide, end fire/edge coupling, rather than evanescent coupling, has been pursued in this dissertation.

Due to the highly sensitive parameter of the separation distance between the laser and waveguide, a big step forward is to be able to eliminate the gap between the edge emitting laser facet and the waveguide end-face. This can be achieved only in a setup where planar integration of the two components on the same substrate is possible, and in fact would be most desirable for a chip-scale sensor platform with integrated optical sensors and electronics.

3 Top-Bottom Contact Thin Film Lasers Integrated onto Silicon: Theoretical Background and Material Structure

In this chapter, concepts in gain guided and ridge lasers are explained, that can be adapted to heterogeneously integrated thin film laser designs. This is covered in Section 3.1. The strain compensated material structure for the lasers studied in this thesis is discussed in Section 3.2.

3.1 Thin Film Laser Designs

The performance parameters associated with a bulk laser (epitaxial laser on bulk growth substrate) are also applicable to thin film lasers. For example, a simple double heterostructure (DH) laser is considered. The laser oscillation condition is defined by the threshold current density J_{th} (A/cm^2), which is the current density in the active region at which the gain just exceeds the loss (i.e. stimulated emission dominates the emission) and the semiconductor laser starts lasing. The threshold current I_{th} is obtained from an optical power (L) versus current (I) curve (L-I curve) measurement of a laser diode, where the threshold current is observed as a sharp increase in the slope of the L-I curve. The threshold current density, J_{th}, is calculated by dividing I_{th} by the electrically pumped area of the device. Reduction of threshold current density is paramount for power efficient devices, which enable low power integrated portable systems and applications. Also, removal of the substrate reduces the series electrical resistance between the p and the n electrode, improving the power efficiency of the structure. The threshold current density is given by [74]:

$$J_{th} = \left(\frac{\alpha_r + \alpha}{\alpha}\right) J_T \tag{3-1}$$

where α_r is the total loss coefficient, α is the absorption coefficient in the material in the absence of current injection, and J_T is the transparency current density, or the current density in the semiconductor for which the photon energy is just equal to the energy gap or separation of the quasi Fermi levels, corresponding to a point where there is no absorption or stimulated emission [74]:

$$J_T = \left(\frac{ql}{\eta_i \tau_r}\right) \Delta n_T \tag{3-2}$$

where q is the electronic charge, l is the width of the active region as defined in Figure 3-1, η_ι is the internal quantum efficiency of the laser, defined as the ratio of the radiative recombination to the total recombination, $1/\tau_r$ *is* the radiative recombination rate and Δn_T is the steady state excess carrier concentration.

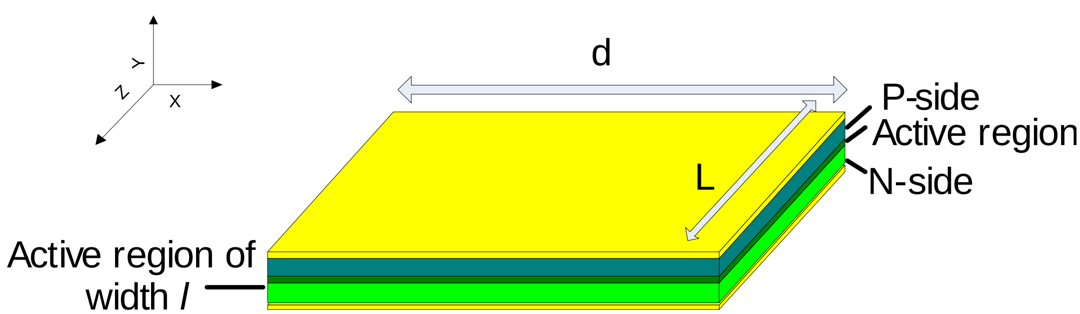

Figure 3-1. Dimensions for a broad area edge emitting laser.

From Equations 3-1 and 3-2, a reduction of the threshold current density dictates a reduction of α_r *or* l or both. The width of the active region, l, can be reduced by choosing double heterostructures to achieve carrier confinement, and by incorporating quantum wells [74]. The loss coefficient α_r is given by:

$$\alpha_r = \frac{1}{\Gamma}(\alpha_s + \frac{1}{2L}\ln\frac{1}{\Re_1\Re_2}) \tag{3-3}$$

where Γ is the optical confinement factor, the fraction of the optical energy within the active region. Increasing the optical confinement reduces the cavity loss. The p and n contact layers in the case of simple DH structures typically have a slightly lower refractive index than the central active region, as they are made from different materials, providing some degree of optical confinement. The variable α_s is the loss from other sources, such as scattering and free carrier absorption, and the second term in the parentheses corresponds to mirror loss as a function of the mirror reflectivities ($\Re_1$ and $\Re_2$) and the distance L between the two mirrors.

The threshold current density J_{th} for a single quantum well (QW) laser is approximated by [75]:

$$J_{th} = \frac{1}{\eta_i}\exp\left(\frac{\alpha_r}{Go}\right)J_T \tag{3-4}$$

where G_o is the gain coefficient that is calculated for a particular laser structure. There are other variations of this equation [76, 77] as well. This is an exponential relationship between the threshold current density and the gain for a quantum well instead of the linear relationship in (Equation (3-1)) for a DH structure. Also, the transparency current density is smaller for a QW, although the gain saturates at a lower current than for a bulk structure.

Thus, reducing the threshold current density of a thin film edge emitting laser requires good overlap between the optical mode and the active pumped region, so that the optical confinement factor (Γ) can be increased. This can be achieved by gain guiding using stripe geometries for current confinement, and index guiding using ridges to further control the current and the effective index of the light emitting region.

A broad area contact laser, such as the one illustrated in Figure 3-1, has many lateral (along the x-direction) optical modes that are equally supported, even though it may be further optically confined in the Y-direction by the incorporation of additional layers of lower refractive index (as in a separate confinement heterostructure, SCH). Also, due to current flowing through the entire width of the laser, filamentation, or the creation of multiple transverse modes due to current density induced index changes, is a problem [78]. Typically the broad area contact is replaced by a stripe contact on the p (epitaxial side) to improve the efficiency of the injected current, and to allow radiative recombination only in a limited region along the x-direction. Figure 3-2 shows simulation results in Silvaco™, a commercial device simulator, where the injected current, and thus gain, is limited mostly to the area below the stripe. As a result, fewer transverse modes are excited across the width of the laser facet, making it easier for coupling to a waveguide or an optical fiber. Details about the use of Silvaco™ for laser simulation problems are discussed in Section 4.3.

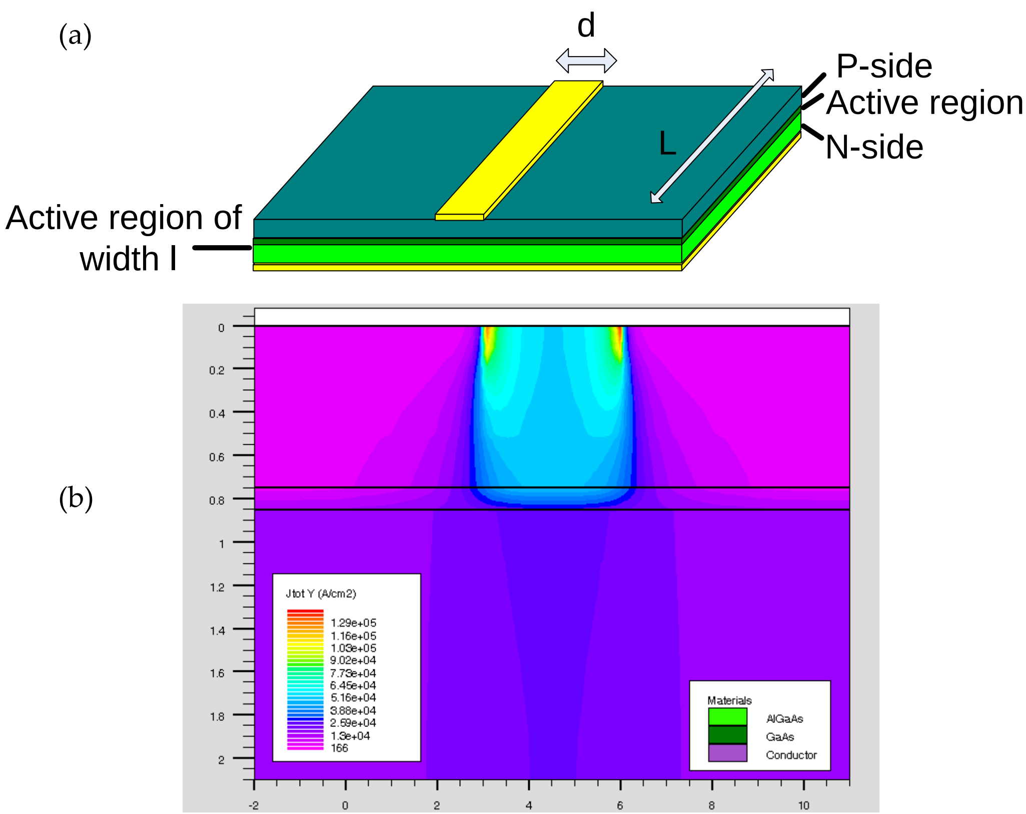

Figure 3-2. (a) Stripe laser, with broad area bottom contact; (b) Current flow in vertical direction.

In both bulk and thin film lasers, the n-contact is typically left as a broad area contact. Since the metal electrodes need to form ohmic contacts with the semiconductor, in practice, highly doped thin contact layers are incorporated on both sides of the laser. This high doping concentration results in current spreading along these layers. Thus, the actual active dimension along the x-direction is larger than the stripe width. This is observed in the gain guided structures simulated and fabricated in this dissertation.

However, a common practice, though not implemented in the gain guided lasers fabricated in this dissertation, is to etch off the thin highly doped p- contact layer to control the current spreading in the p-conductive layer. There is no means of accessing the n-side in bulk lasers, which remains highly conductive and has a broad area contact.

A stripe added on the n-side (that is, stripes on the top and bottom of the thin film EEL) would limit the current in the y-direction, partially reducing the lateral spread of current, as shown in Figure 3-3. Again, in this case, the highly doped contact layers have been ignored for the purpose of simulation. This configuration is possible only for a thin film EEL that can be accessed and patterned on both sides, and not for a bulk laser. These simulations illustrate that current control is possible from both sides of the laser. Simulated L-I curves for unstrained GaAs/AlGaAs DH lasers, as shown in Figure 3-3, show that there is improvement in the threshold current due to incorporation of the n-stripe.

(a)

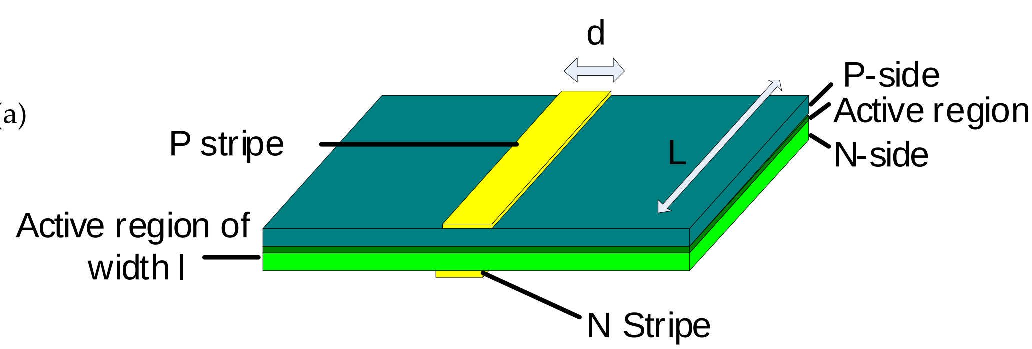

(b)

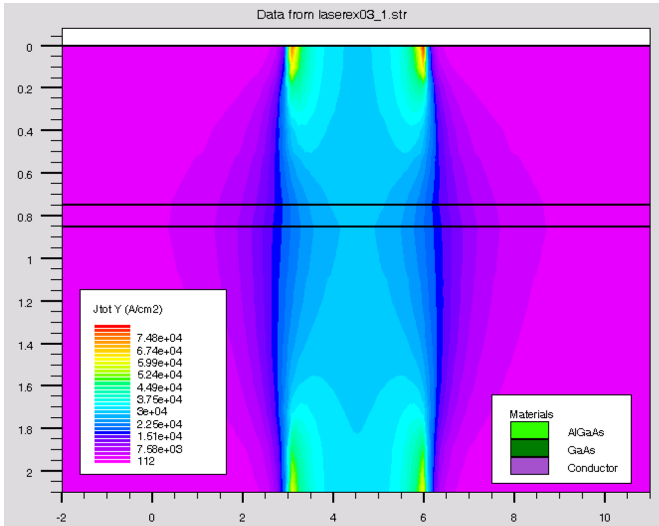

(c)

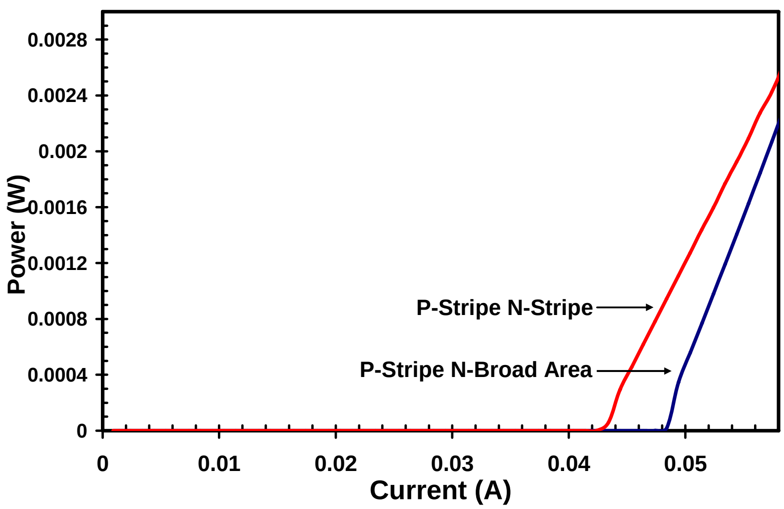

Figure 3-3. (a) Stripes on top and bottom of thin film laser; (b) Current density in the vertical direction; (c)Reduction in threshold current due to incorporation of the stripe on the n-side of a DH unstrained thin film laser.

While it is desirable that only a narrow stripe be patterned to limit the lateral current pumping, whether for a DH or a QW laser, there is an issue of increased threshold current density associated with stripe-defined gain guiding lasers of short cavity lengths, especially for strained quantum well material systems such as

InGaAs/GaAs [79-81]. This is because of a reduction in the real part of the refractive index of the active region due to the injection of carriers below the stripe. This leads to index anti-guiding, causing defocusing, which is manifested as double lobed far field optical patterns. As a result, there is a lower limit on the stripe width that can be implemented without an increase in threshold current density. This factor needs to be taken into account for the design of top and bottom stripe lasers, where the current density in the active region will be even higher for a given injected current density, potentially leading to higher refractive index changes. Thus, it is shown above that current control is possible through designing the placement of electrodes, but the effect of index anti-guiding in the InGaAs/GaAs strained quantum well system used in the dissertation would dominate the performance. As a result, the highly doped contact layers were left intact even after incorporating stripes into the lasers fabricated for this thesis.

Both the weak index guiding in a stripe laser and the current confinement can be improved by etching a ridge around the stripe and forming a channel waveguide, thus providing lateral optical confinement [76, 82]. This is a common form of edge emitting lasers commercially available. Improvement in the optical mode as a result of a ridge structure is illustrated in Figure 3-4. Index loading due to presence of the ridge results in a higher effective index in the central pumped portion of the gain region, confining the optical mode to the width of the ridge. Anti-guiding effects are not present, since the change in the effective index due to index loading is greater than the refractive index reduction due to increased carrier densities. The depth of the ridge determines the index contrast, and consequently, the number of modes supported by the structure. A deeper ridge depth also reduces current spreading in the doped cladding layers of the heterostructure, and thus can improve the threshold current of the laser [83].

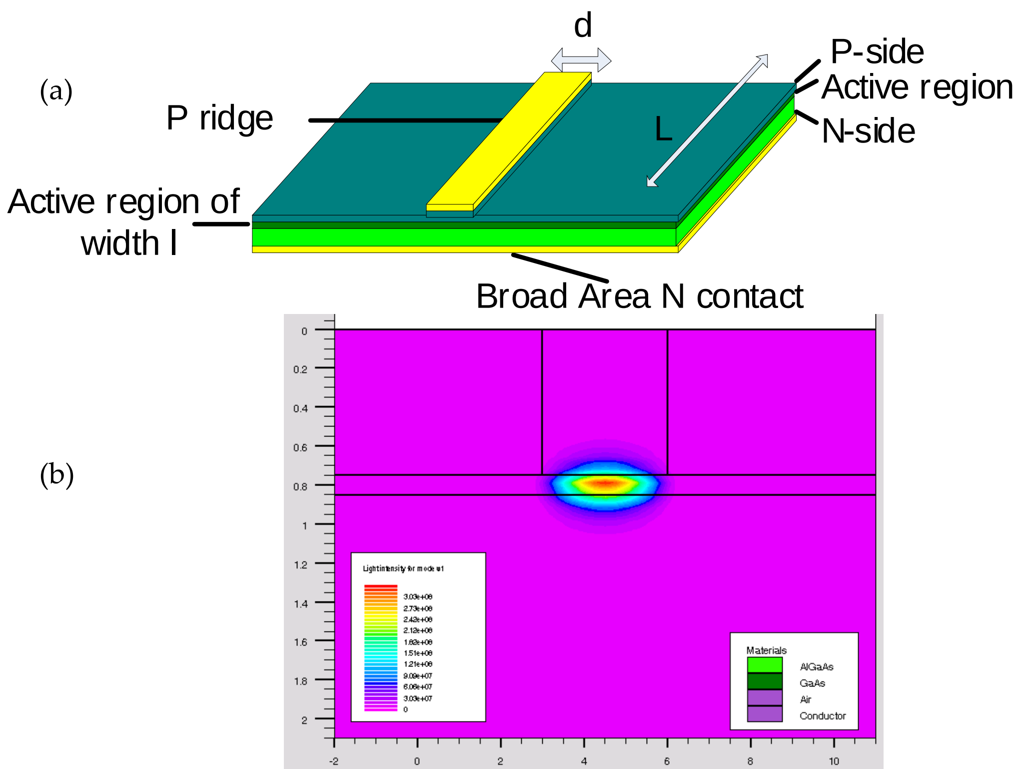

Figure 3-4. (a) Ridge laser, with p-ridge and broad area n contact; (b) Fundamental optical mode.

In addition to gain and index guiding, high reflectivity mirror facets are required for low threshold current density operation, achievable by high reflectivity (HR) coating or cleaving, rather than etching. Reduction of surface or scattering losses by passivation, for example, could further reduce the threshold current density. Also, a laser is a high power device, and system level thermal management strategies should take this into account by having metal interfaces for heat sinking as close to the active region as possible to reduce thermal resistance.

The ability to pattern both sides of the epitaxial structure of a thin film laser provides the opportunity to utilize the configurations described above in unique ways. It is possible to incorporate n-stripes and/or ridges along with p-ridges on the thin film laser to enable control over current and refractive index not only through the p-ridge width and depth but also through the patterning of electrodes (and ridges) on the n-side.

Figure 3-5 gives an overview of the generations of lasers explored in this thesis. As discussed, the state of the art for thin film lasers has largely focused on either all contacts on the top of the device, resulting in non-conducting interfaces with the host substrate, or the laser is typically thicker than typical thin film lasers (≤ 5 μm) when the contacts are on both sides. Patterning on both sides of a thin film laser while under growth or host substrate support has not been reported before the work in this thesis. In this thesis, gain guided lasers formed the first generation of lasers where stripes were incorporated on both sides for the first time, while also having a broad area metal bond with the host substrate (Si or SiO_2/Si). In the second generation, index guided thin film lasers with a broad area n-contact were explored. The fabrication process was difficult and hard to reproduce, though lasing results were demonstrated. Combining both aspects of the gain guided and the index guided broad area contact lasers, the third generation of lasers with slots were defined for index guiding, while having an electrically isolated broad area contact with the SiO_2/Si host substrate. N-stripes were incorporated, and a stable fabrication process was developed. Threshold current densities as low as 244 A/cm^2 were achieved.

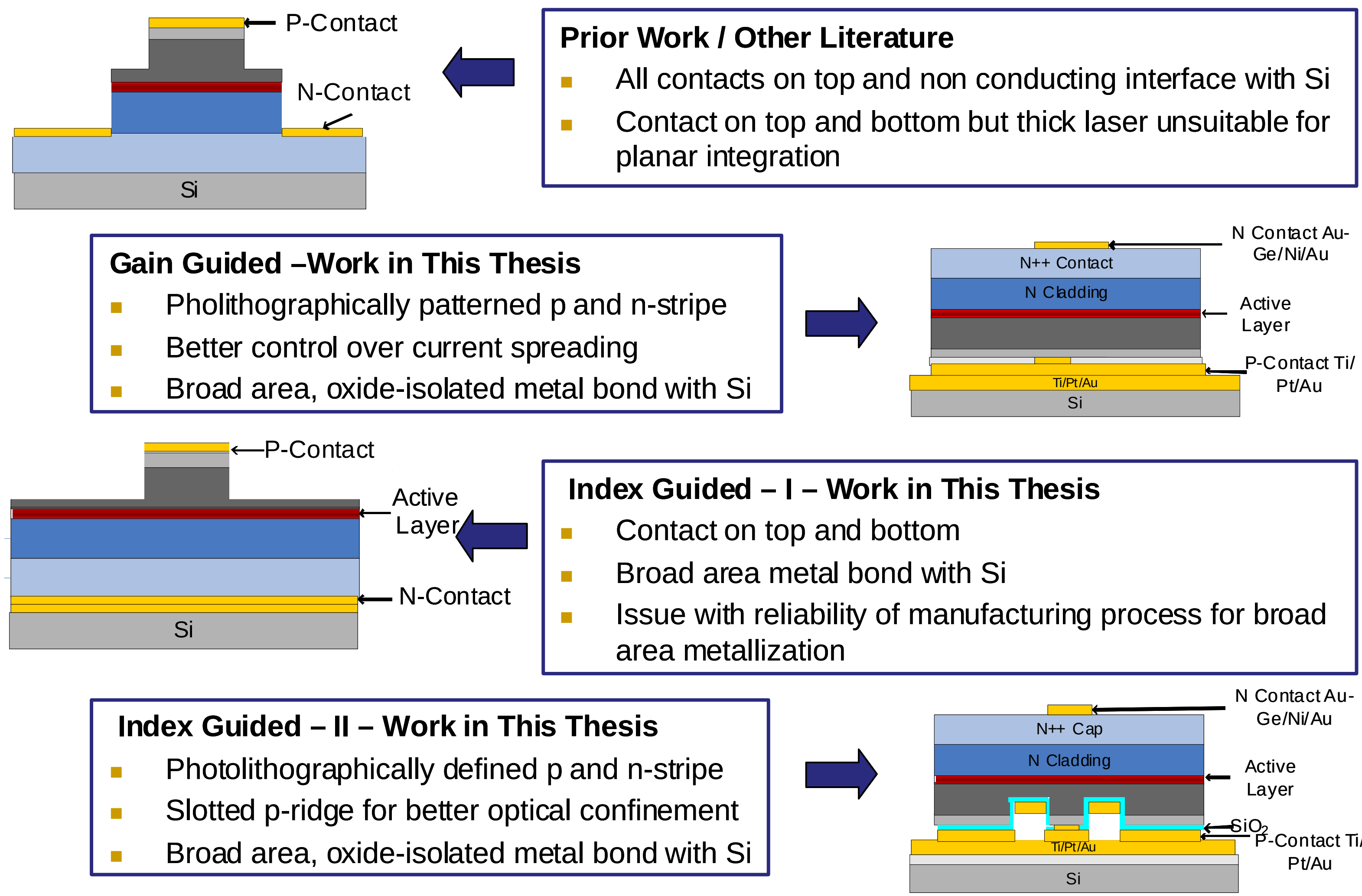

Figure 3-5. State of the art and laser generations implemented in this thesis.

3.2 Material Structure

Lasers with strained active regions are more desirable from the perspective of wider wavelength range, control over polarization and improved threshold current density [76, 84]. However, a strained gain region results in a net strain in the epitaxial structure, and this strain is manifested in the form of physical deformations once the device is released from its growth substrate before bonding onto silicon or any other host substrate. The thin film laser will bow or curl due to the net strain, making it virtually impossible to integrate onto any planar platform.

To address this, a strain compensated laser epitaxial structure, as shown in Figure 3-6 was grown using metal organic chemical vapor deposition (MOCVD) by collaborators, Dr. Gene Tsvid and Jeremy Kirch from Prof. Luke Mawst's group, at the University of Wisconsin-Madison, and calibrated using X-ray diffraction. It is a standard $In_{0.2}Ga_{0.8}As$/GaAs single quantum well structure designed to lase at 980 nm, with a well width of 7.5 nm, barrier width of 10 nm, and a GaAs separate confinement heterostructure (SCH) that is 400 nm wide.

The strain in the quantum well is calculated as follows:

$$\varepsilon_{sqw} = \frac{a_{InGaAs} - a_{GaAs}}{a_{GaAs}} = \frac{5.7343 - 5.65325}{5.65325} = 0.014 = 1.4\% \text{ compressive} \quad (3\text{-}5)$$

To compensate for this, $GaAs_{0.7}P_{0.3}$ tensile barriers were added to the GaAs layer using the formula [85]:

$$N_a t_a \delta_a + N_b t_b \delta_b \approx 0 \tag{3-6}$$

where N_a is the number of quantum wells, which is one in this case, t_a corresponds to the thickness of the well, i.e. 75Å, and δ_a is the difference in lattice constant between the $In_{0.2}Ga_{0.8}As$ well and the GaAs substrate/barrier, which is $5.7343 - 5.65325 = 0.08105$ Å. N_b is the number of strain compensating barrier $GaAs_{0.7}P_{0.3}$ layers, which is two in this case, t_b corresponds to the thickness of the tensile barrier, i.e. 75Å, and δ_b is the difference in lattice constant between the $GaAs_{0.7}P_{0.3}$ layer and the GaAs substrate/barrier, which is $5.592425 - 5.65325 = -0.060825$ Å. This yields a thickness of 50Å for each tensile barrier (t_b). Strain-compensated lasers have also been shown to have better thermal characteristics and lower degradation in bulk lasers [86], and thus provide further motivation for their use in thin film lasers.

The rest of the material structure is composed of a 0.07 µm p^+ GaAs layer (p-contact, Zn doped, p~$5\text{x}10^{19}$ cm^{-3}), 1.1 µm p-$Al_{0.74}Ga_{0.26}As$ (cladding, Zn doped, p~$1\text{x}10^{18}$ cm^{-3}) , 400 nm undoped GaAs SCH (with the strain compensated SQW as mentioned above), 1.1 µm n-$Al_{0.74}Ga_{0.26}As$ (cladding, As doped, n~$1\text{x}10^{18}$ cm^{-3}), 1.5 µm n^+ GaAs (n-contact, As doped, n~$5\text{x}10^{18}$ cm^{-3}), and a 250 nm AlAs selective etch-layer for separating the epitaxial EEL structure from the GaAs substrate. From simulations in RSoft BeamPROP, a numeric finite difference solver using the beam propagation method (BPM) [87, 88], that, in its basic form, solves the scalar form of the Helmholtz wave equation for paraxial conditions, it was found that the optical mode was pulled towards the thick, higher index n^+ GaAs layer. So, in later growths, the 1.5 μm n^+ GaAs was replaced by a thinner 0.4 μm n^+ GaAs layer. Also, it was found that substrate etching where the entire substrate is removed using an etch-stop layer is a more reliable process than substrate removal where a selective etch layer is laterally etched to release the substrate from the thin film. In the case of substrate release/removal, it was found that as the lateral etch progressed; the weight of the substrate deformed the remaining structure, damaging the lasers in the center of the sample. As a result, the selective etch layer of AlAs was replaced by an etch-stop layer of $In_{0.49}Ga_{0.51}P$. Details of the device processing for each of these growths are specified in the individual device sections and appendices.

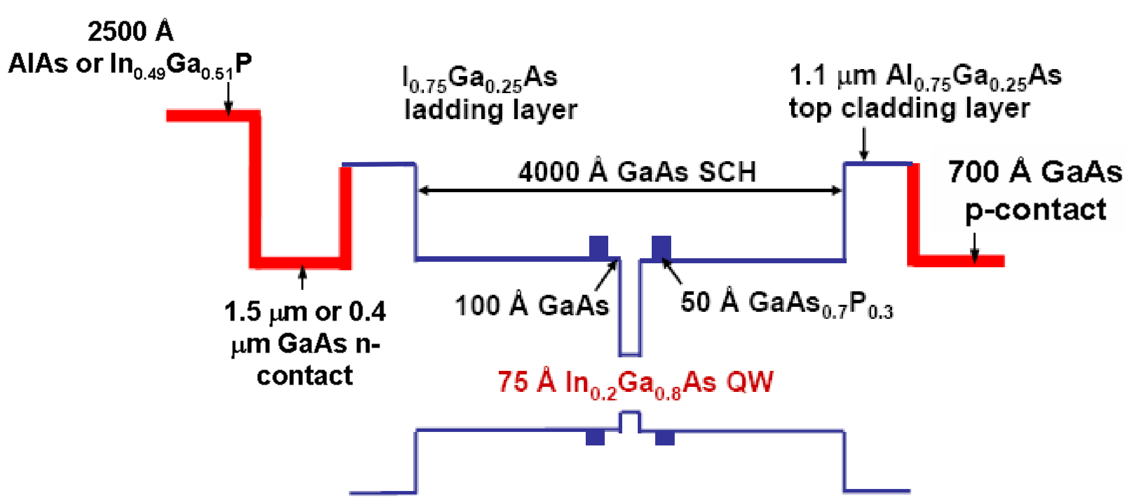

Figure 3-6. Material structure for the strain compensated lasers described in this thesis.

4 Gain Guided Thin Film Lasers Integrated Onto Silicon Substrates

In this chapter, gain guided thin film lasers have been developed and bonded to Si substrates. Section 4.1 describes the first attempt at p and n-stripe lasers, without any broad area metal bonding to the substrate. Section 4.2 describes p and n-stripe lasers where the electrically isolated p-stripe side of the laser is broad-area bonded to the Si substrate. Section 4.3 discusses the simulations for these structures using Silvaco Atlas™, a commercial semiconductor device simulation software package.

4.1 Top and Bottom Stripe[1]

The top and bottom stripe laser was primarily implemented as a proof of concept for thin film EELs with patterned contacts on the top and bottom of the device, but this structure had low yield due to challenges with bonding and alignment. As shown in Figure 4-1, the fabrication process involved patterning the p-stripe (Ti-15 nm/Pt-15 nm/Au-100 nm), followed by mesa etching, encapsulation in Apiezon W, and substrate removal. The laser was then bonded p-side down to the Si substrate. The region of the p-side not covered by the stripe was vulnerable to electrical short when bonded to a broad area Au coated silicon wafer. To prevent this, stripes of width equal to the p-stripe were patterned on the silicon. This required that the laser be aligned and bonded

[1] Excerpts appear in: S. Palit, G. Tsvid, J. Kirch, J. Y.-T. Huang, T. Tyler, S.-Y. Cho, N. Jokerst, L. Mawst, and T. Kuech, "Top-Bottom Stripe Thin Film InGaAs/GaAsP Laser integrated on Silicon," in *IEEE Device Research Conf,* June 23-25, 2008, Santa Barbara, CA, pp. 137-138.

precisely to the bonding pad stripe on the Si substrate. This was followed by a low temperature anneal for metal-metal bonding and standard negative photolithography using a thick photoresist (to enable coverage of the 3.6 μm thick laser), metallization (AuGe 88-22 % wt. alloy-80nm/Ni-10 nm/Au-150 nm,) and liftoff processes. Even though a low-temperature metal anneal was performed, since the bonding area was a very small fraction of the total area of laser, the subsequent process steps such as spin coating of photoresist and metal liftoff caused the laser to delaminate.

The lasers were characterized using L-I measurements by positioning a multimode optical fiber at the laser facet that was nearer to the edge of the substrate, with the other end of the fiber incident on an HP 81521B optical head connected to an HP 8163A power meter. A pulsed current with a 1 KHz frequency and 0.5 μs pulse width from an ILX Lightwave, LDP 3811 laser driver was used to drive the laser, by probing it directly on the n-stripe and the bonding pad stripe on the Si substrate. The L-I characteristics for one of these lasers, shown in Figure 4-2, indicate an apparent threshold of less than 10 mA. However, the measured power was too low to be measured by an optical spectrum analyzer (OSA). OSAs are used for spectral characterization, plotting the light output power as a function of optical wavelength. So, although a knee was observed in the L-I characteristics, spectral verification of lasing was not possible.

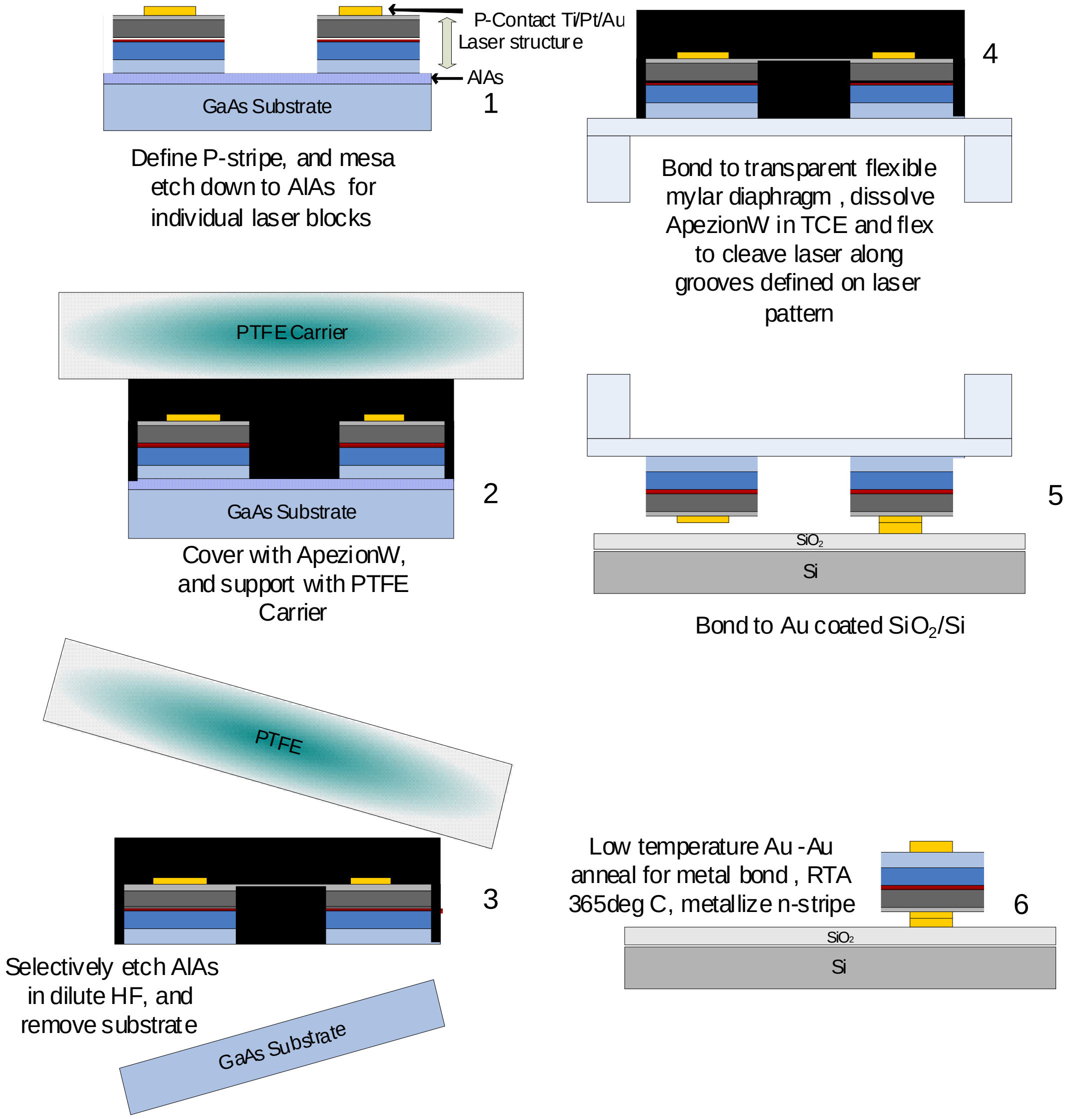

Figure 4-1. Process flow for top and bottom stripe laser (not drawn to scale). (1) Definition of stripes on EEL structure on the growth substrate. Mesa etch to define the EEL bars; (2) Encapsulation of mesas in Apiezon W and attachment to a PTFE carrier. (3) Selective substrate removal; (4) Bonding to a Mylar® transfer medium; (5) Transfer to a metallized Si or SiO_2/Si. The p-side stripe is aligned and bonded to an Au-stripe patterned on the host substrate, followed by a low-temperature diffusion anneal at 180 °C; (6) Photolithography, n-stripe metallization and liftoff, followed by RTA for forming ohmic contacts.

(a)  (b) 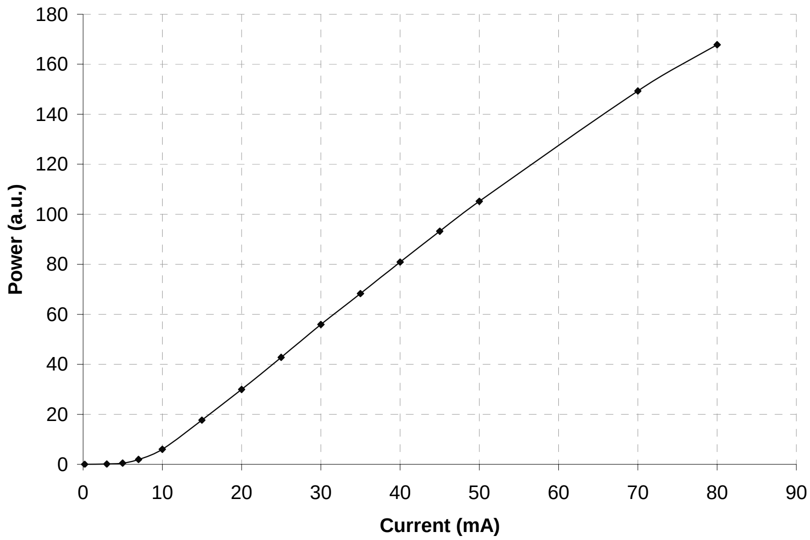

Figure 4-2. (a) Photomicrograph of top and bottom stripe laser, with p-stripe W= 40 μm, n-stripe W =50 μm, and laser cavity L=710 μm. (b) L-I characteristics measured with a photodetector and power meter.

4.2 Top and Bottom Stripe, with Broad Area Bonding[2]

The challenges faced with the top and bottom stripe lasers were alleviated by making some major design changes. To address the issue of electrically isolating the p-side outside the stripe after bonding, the p-side was passivated with plasma enhanced chemical vapor deposited (PECVD) SiO_2 after metallizing the p-contact stripe, the oxide over the stripe was removed by a buffered oxide etch, and then metal was deposited over the entire p-side of the laser bars. The oxide and broad area metal addressed the issue of alignment, as electrical shorts would no longer occur by improper alignment of the p-side with a bond pad on the host substrate. Also, when bonding the laser to the

[2]Excerpts appear in: S. Palit, G. Tsvid, J. Kirch, Juno Yu-Ting Huang, L. Mawst, T. Kuech, N. M. Jokerst, "Broad area metal/metal bonding of thin film edge emitting lasers to silicon," in *Proc. 21st Ann. Mtng. of the IEEE LEOS*, Newport Beach, CA, USA, Nov 9-13, 2008, pp. 123-124.

host substrate, i.e. Au coated SiO_2/Si; broad area metallization could be used on the SiO_2/Si instead of a patterned stripe. Second, the challenge of a small bond area that was unstable for further processing was also addressed by the broad area metallization, as it enabled a larger area, and thus, stronger bond between the laser and the host substrate, making n-side processing easier. Lastly, the broad metallization enabled a larger contact area for greater heat dissipation.

The broad area contact laser was fabricated using two process flows. The first utilized a broad area oxide deposition on the p-side of the laser material, etching trenches into the oxide for p-side metallization, and then depositing a broad area metallization that filled the trenches and formed the p-stripe contact. This had the disadvantage that if the trenches for the p-stripes were not aligned and etched precisely, a thin layer of oxide could still remain between the p-GaAs of the laser material and the metal contact, resulting in a non-ohmic, highly resistive contact. The second process, as outlined in Figure 4-3, began with an additional step, wherein the p-stripes were first deposited on the p-GaAs, followed by oxide deposition, etching of trenches to reach the p-stripe metal, and broad area metallization. These were followed by mesa etching, encapsulation in Apiezon W, and substrate removal. The embedded laser array was then transferred to a Mylar® diaphragm. The devices adhered to the Mylar® due to van der Waal's forces. The Apiezon W was dissolved away using trichloroethylene (TCE). The lasers on the Mylar® were cleaved by flexing the diaphragm, and these were then transferred to Au pads on the Si substrate. This was followed by negative photolithography, metallization and lift-off for the n-stripe. A step-by-step fabrication recipe is described in Appendix A.1 for this structure.

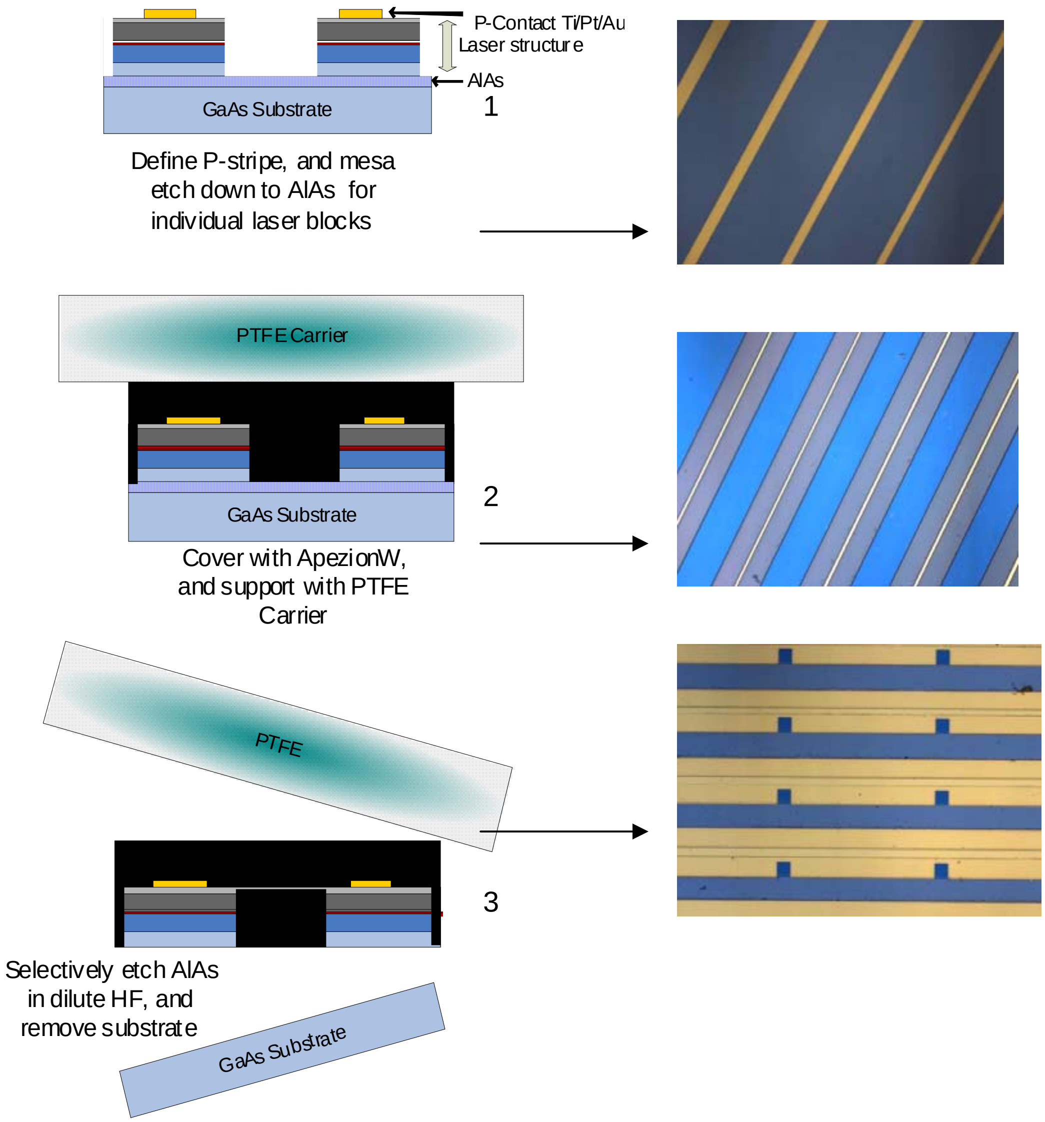

Figure 4-3. Process flow for top and bottom stripe, broad area bonded laser (not drawn to scale) with associated photomicrographs; (1) P-stripe metallization and oxide deposition; (2) Pattern and etch oxide to separate laser bars and expose p-stripe; (3) Broad area metallization across width of laser bar; (4) Mesa pattern and etch to etch-stop layer.

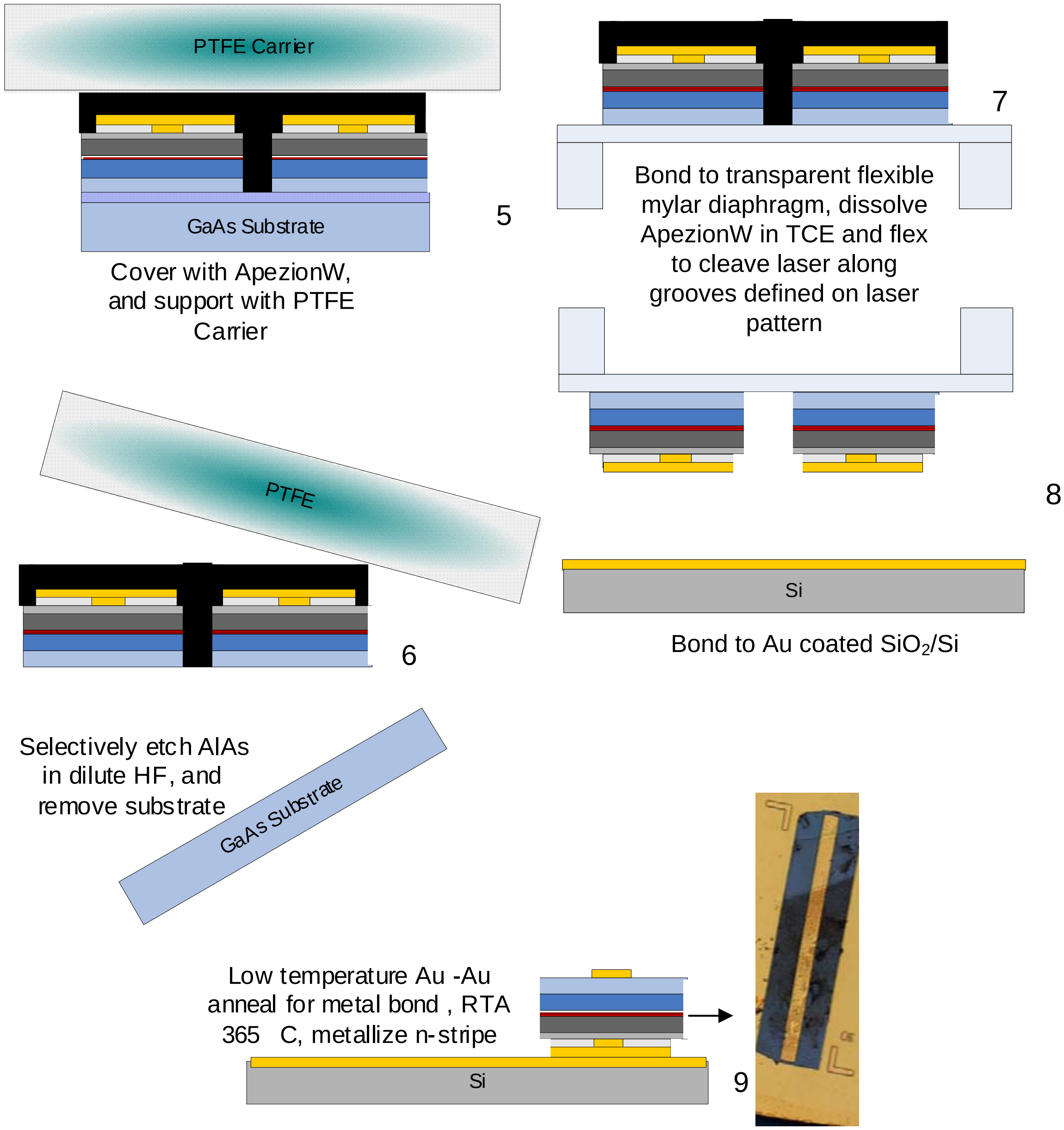

Figure 4-3. Process flow for top and bottom stripe, broad area bonded laser (continued): (5) Encapsulation of mesas in Apiezon W and attachment to a PTFE carrier; (6) Lateral etch of etch-stop/selective etch layer of AlAs to release substrate; (7) Transfer to Mylar® diaphragm; (8) Dissolve Apiezon W and transfer to bond pad on metallized Si; (9) Low-temperature diffusion anneal at 180 °C. Photolithography, n-stripe metallization and liftoff, followed by RTA at 365 °C for forming ohmic contacts.

The L-I curves for the top-bottom stripe broad area contacts were measured by driving the device with a 1 KHz 1 μs pulse width drive current using probes, and coupling the light from one device facet to a multimode optical fiber. The output of the fiber was incident on a photodetector which then led to a power meter. The results from these devices were not encouraging. The L-I characteristics did not exhibit a clear threshold.

In the case of the "p-metal first" version, where the host substrate was Au on bare silicon mounted on a copper heat sink, the measurements were performed at University of Wisconsin-Madison by Jeremy Kirch. The multimode fiber was replaced by an integrating sphere to capture absolute power values. A change in the slope of the L-I curve in Figure 4-4 was observed for two lasers, which could potentially be a lasing threshold. The power output from these lasers was extremely low. This may be explained by lack of optical confinement in the lateral direction and possibly index anti-guiding, as discussed earlier. Also, the lasers could not support high currents, which may have been due to the high current confinement or poor electrical contacts. The stripe widths were on the order of 8 and 10 μm and cavity lengths were 500 μm. In strained quantum well InGaAs/GaAs lasers, there is an anomalous increase in threshold current density for narrow stripe widths (≤ 8 μm) and short cavity lengths (≤ 510 μm) [79], and the value of 1250 A/cm^2 as calculated for the 8 μm wide stripe may be a result of this phenomenon.

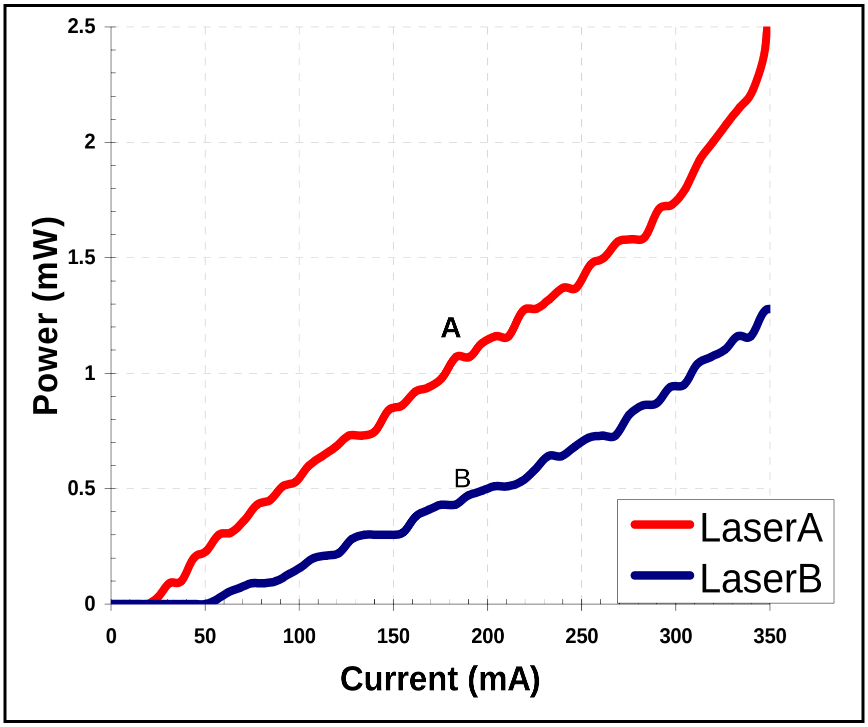

Figure 4-4. L-I characteristics for top and bottom stripe, broad area bonded laser, p-side metallized first. Laser A has p-stripe width=10 μm, n-stripe width=30 μm, cavity length L=500 μm. Laser B has p-stripe width=8 μm, n-stripe width=30 μm, cavity length L=500μm. Laser A has an apparent threshold of 20 mA, and Laser B of 50 mA.

A final set of measurements was performed with broad stripes of 50 μm on both the p and n-side, with a cavity length of 800 μm. The L-I characteristics are as shown in Figure 4-5, indicating a threshold current density of 420 A/cm^2. This lower threshold current density is expected for a laser with such broad stripes, however, the laser would be highly multimode and would also suffer from filamentation effects due to the large cross-sectional area over which the current is pumped.

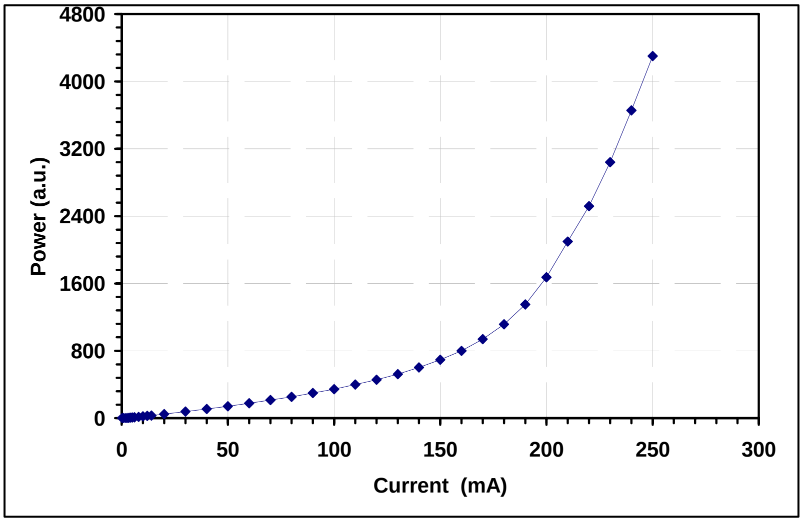

Figure 4-5. L-I characteristics for 800 μm thin film broad area bonded laser with 50 μm wide p-stripe and 50 μm wide n-stripe.

These values of J_{th}, calculated conservatively using the p-stripe width, would be lower if current spreading across the p^+ and n^+ contact regions were included. A realistic measurement of the increase in threshold current density due to the narrow stripe width would be possible only by etching away the highly conductive layers outside the stripe.

4.3 Numerical Simulations and Discussion

The gain guided lasers fabricated and tested in Sections 4.1 and 4.2 were simulated using the Silvaco™ Atlas 2D device simulator with the LASER and Blaze advanced material system module. A laser requires simulations that couple the electrical and optical behavior of the device by solving self-consistent carrier continuity equations (electrical model) with the Helmholtz equation (optical model) [89].

The electrical model consists of Poisson's equation:

$$div(\varepsilon \nabla \psi) = -\rho \tag{4-1}$$

where ψ is the electrostatic potential, ε is the local permittivity, and ρ is the local space charge density. In addition, the carrier continuity equations that relate the change in carrier concentrations with the change in current density, generation, and recombination rates of electrons and holes, are used along with the drift-diffusion current model. The carrier continuity equations are defined as [82, 89]:

$$\frac{\partial n}{\partial t} = \frac{1}{q} div \vec{J}_n + G_n - R_n \tag{4-2}$$

$$\frac{\partial p}{\partial t} = \frac{1}{q} div \vec{J}_p + G_p - R_p \tag{4-3}$$

where n and p are electron and hole carrier concentrations, respectively, q is the electron charge, $\vec{J}_n$ and $\vec{J}_p$ are electron and hole current densities, respectively, G_n and G_p are electron and hole generation rates, respectively, and R_n and R_p are electron and hole recombination rates, respectively. The current densities $\vec{J}_n$ and $\vec{J}_p$ are given by the drift-diffusion current model:

$$\vec{J}_n = qn\mu_n \vec{E}_n + qD_n \nabla n \tag{4-4}$$

$$\vec{J}_p = qp\mu_p \vec{E}_p + qD_p \nabla p \tag{4-5}$$

where μ_n and μ_p are electron and hole mobilities respectively, D_n and D_p are diffusion coefficients calculated from the Einstein relationship respectively, and ∇n and ∇p are concentration gradients for electrons and holes, respectively.

The optical model consists of the reduced scalar Helmholtz equation:

$$\frac{\partial^2 E}{\partial x^2} + \frac{\partial^2 E}{\partial y^2} + \left(\frac{\omega^2}{c^2} \varepsilon - \beta^2 \right) E = 0 \qquad (4\text{-}6)$$

where $E(x,y)$ is the transverse optical field component, ω is the lasing frequency, $\varepsilon(x,y)$ is the local high frequency permittivity, which is a function of the quasi Fermi levels, and β is the propagation constant, and c is the speed of light.

The electrical and optical models are connected by the optical gain which, for zinc blende structures is defined by the following function [89, 90]:

$$g(hv) = \left(\frac{\pi q^2 \hbar}{\varepsilon_o n_r c m_o^2 E} \right) \left| M(hv) \right|^2 D_r D_{opt} (f_j - f_i) \qquad (4\text{-}7)$$

where q is the charge of an electron, $\hbar$ is reduced Planck's constant, m_o is the electron mass, ε_o is the permittivity of vacuum, n_r is the refractive index, $\left| M \right|^2$ is the transition matrix element, (anisotropic for quantum wells, and thus dependent on polarization), D_r is the reduced density of electron states, D_{opt} is the optical density of states and f_j and f_i are Fermi functions corresponding to a high and low energy level respectively, the energy difference of which is $h\nu$.

The permittivity ε in Equation (4-6) is a function of gain $g(h\nu)$ and loss parameters as described in Equations (3-1) and (3-3). As the gain is a function of Fermi levels, this involves the carrier continuity equations. In other words, the carrier and photon rate equations for a laser are dependent on gain, enabling the self-consistent solution of these equations to yield optical power as a function of electrical input.

Although a 2D simulation is performed in Silvaco™, the cavity length in the z-direction is also provided as an input to calculate the longitudinal modes (for spectral information) and mirror losses. The simulator calculates quantum well bound states by using a 1-D solver for the Schrödinger equation. For laser simulations, the highest valence band bound state and lowest conduction band bound state is used.

The simulations for the lasers in this dissertation calculate the band gap energy and electron and hole effective masses for the InGaAs quantum well using the influence of compressive strain and provided this as an input parameter. The strain effects of the GaAsP tensile barrier were calculated by the simulator. The electrical and optical parameter values for the epitaxial structure were taken from existing literature [90-95]. Thermal effects were not considered in these simulations.

The first set of simulations were performed for the 8 μm p-stripe and 30 μm n-stripe thin film laser, which had a cavity length of 500 μm. Only one vertical half of the laser was simulated to reduce computational time, which is possible because the laser had vertical symmetry. Simulations were performed at a constant optical frequency (i.e. at a peak wavelength - the laser spectrum was not calculated) for multiple transverse modes. The simulated threshold current was doubled to take into account the full structure. From Figure 4-6 (a), the threshold current was ~60 X 2 = 120 mA, as compared to an experimental value of 50 mA. Kinks, i.e. changes in the slope of the L-I curve, were observed at higher currents, and were expected for stripe lasers [96]. This again, is a result of self focusing and filamentation. The cross sectional view of the plot of current density in the vertical direction in Figure 4-6(b) indicated that there is high amount of current spreading in the highly doped contact layers. The effect of current control by the n-stripe was limited due to the thick n+ GaAs contact layer, which caused current spreading. The plot of the optical gain for the structure in Figure 4-7 (a) indicated that it was highest in the center of the device for the stripe laser. However, lateral mode instability due to index anti guiding was a problem for the stripe laser, and this manifested itself in most of the lower order modes. Figure 4-7 (b) shows that the fundamental mode was heavily anti-guided since the highest optical intensity was not located under the stripe, while Figure 4-7 (c) shows the results of a simulation of a higher order mode in the laser. Thus, higher order modes do overlap the high gain region under the stripe, although the fundamental mode does not.

(a)

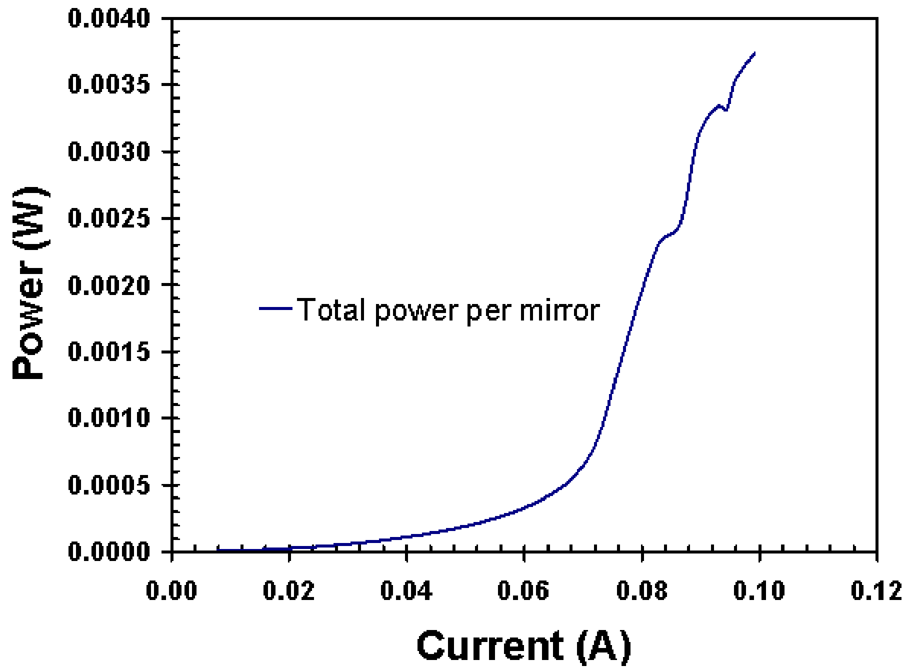

(b)

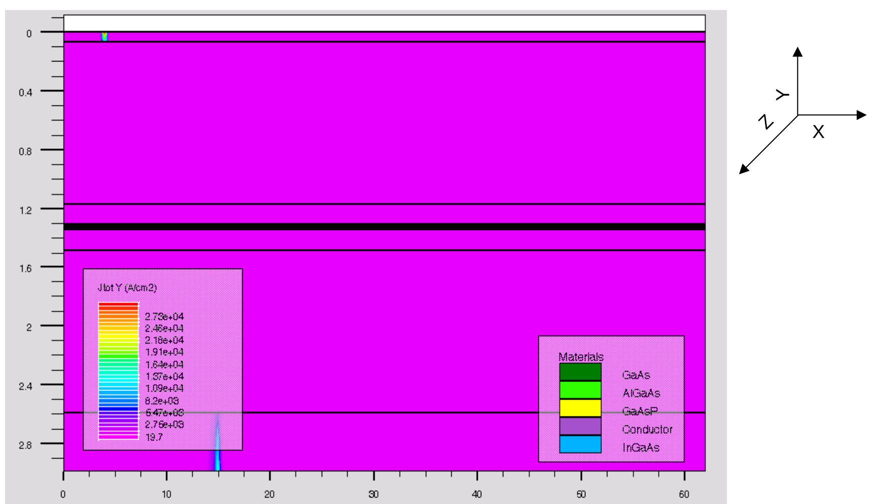

Figure 4-6. (a) Simulated L-I curve for 8 μm wide p-stripe and 30 μm wide n-stripe thin film laser of cavity length = 500 μm; (b) Simulated plot of current density in cross-sectional view of the EEL.

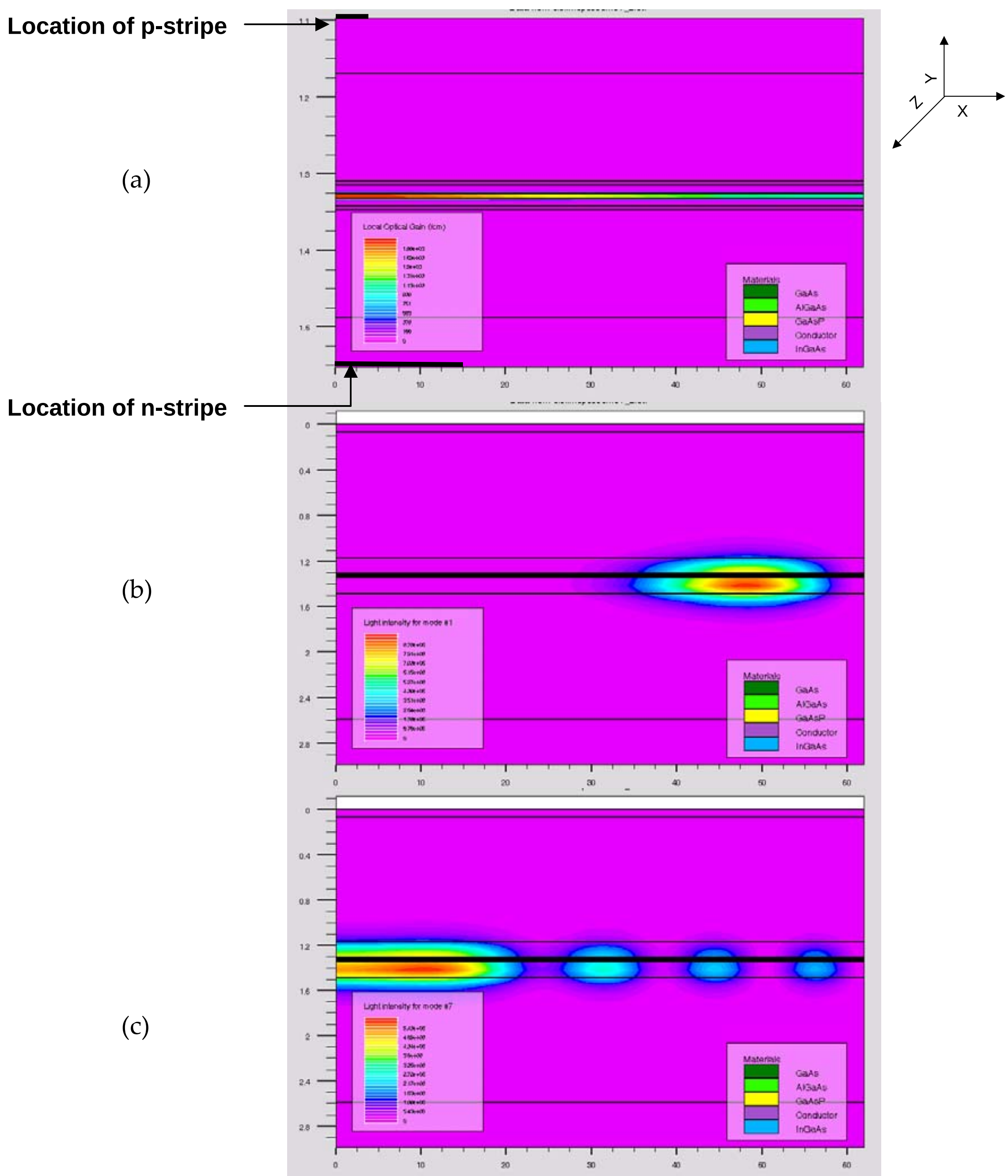

Figure 4-7. (a) Local optical gain in the quantum well for 8 μm wide p-stripe and 30 μm wide n-stripe thin film EEL of cavity length = 500 μm; (b) Fundamental mode, with index anti guiding exhibited, as the mode is split and pushed away from the center of the laser; (c) Example of higher order transverse mode indicating higher optical intensity towards the center of the laser. Center of the laser corresponds to x=0

The 50 μm wide p-stripe and 50 wide μm n-stripe laser, with a cavity length of 800 μm, was also simulated. Again, one half of the structure was simulated to decrease computational time, a constant optical frequency was used, and multiple transverse modes were calculated. A threshold current of 130 mA was obtained for the structure, as shown in Figure 4-8, compared to an experimental threshold current of ~160 mA (Figure 4-5). Again, in this case, higher modes are supported, and the lower order modes are degraded by index anti-guiding, as seen from the simulations in Figure 4-9.

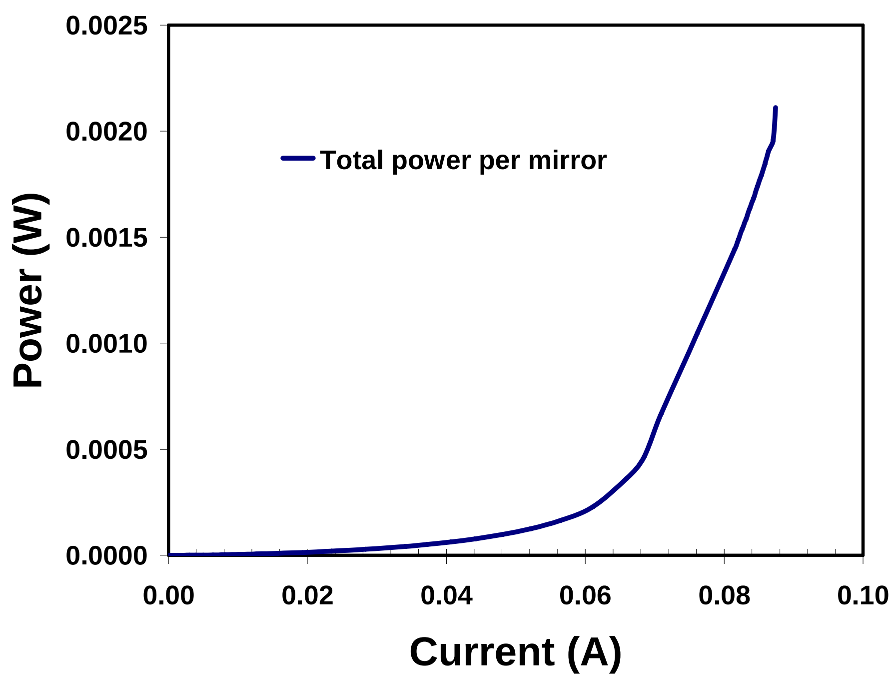

Figure 4-8. Simulated L-I characteristics for one half of a 50 μm wide p-stripe and 50 μm wide n-stripe laser, with cavity length of 800 μm. Since this is simulation of one half of the EEL structure, the threshold current is double that indicated (i.e. 65 mA x 2 = 130 mA. The experimental threshold current value was ~160 mA.

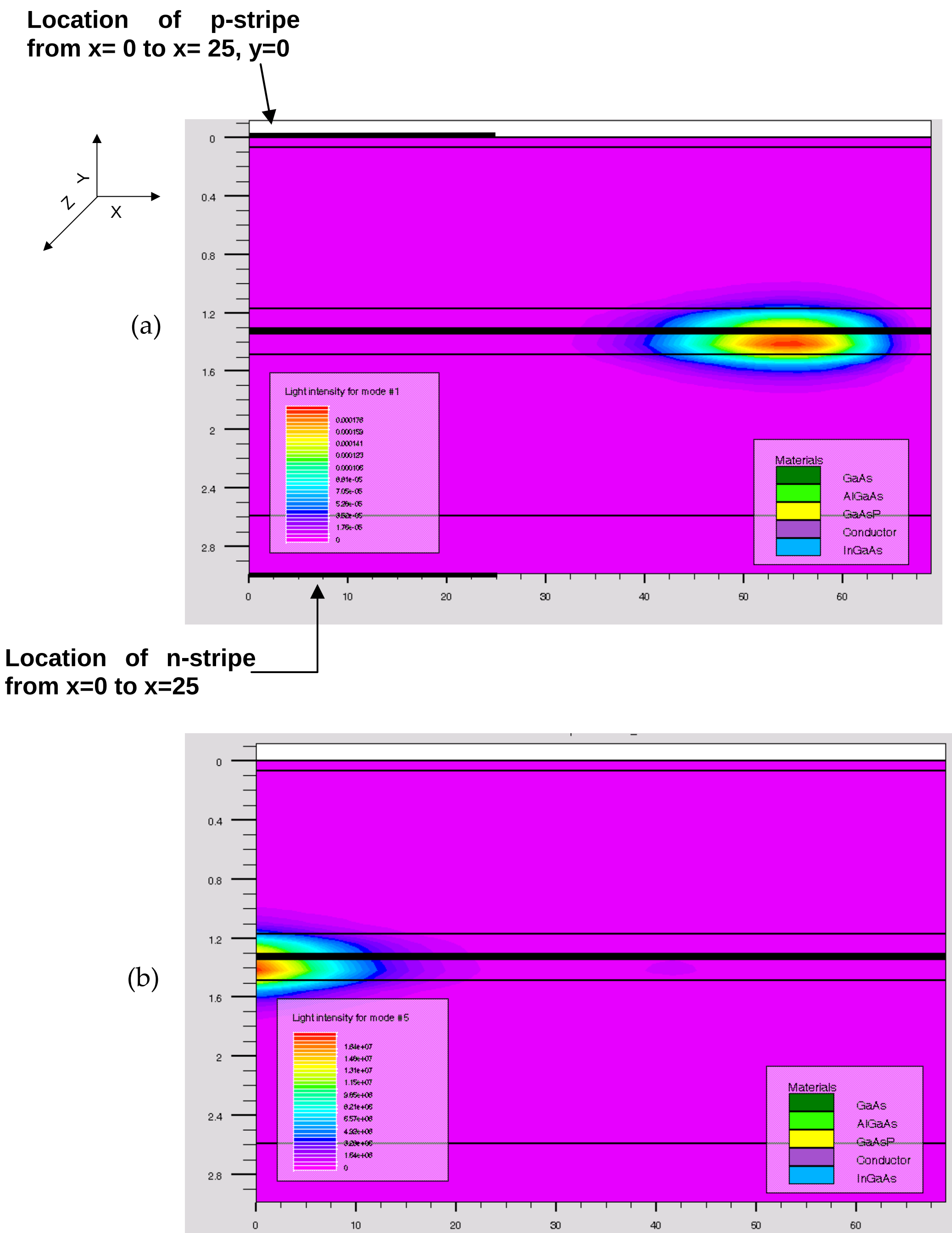

Figure 4-9. Simulation of transverse optical modes of the 50 μm wide p-stripe and 50 μm n-stripe laser, with cavity length of 800 μm. (a) The fundamental mode is affected by index anti guiding and not supported by the laser (b) Supported higher order mode below stripe.

The simulations underestimated the threshold current of the 50 μm wide p-stripe and 50 μm wide n-stripe laser and overestimated the 8 μm wide p-stripe and 30 μm wide n-stripe laser. This may be attributed to the large number of transverse optical modes that are usually supported by these stripe lasers, and the fact that the effective indices and longitudinal frequencies associated with each of them are different, factors which were not taken into account in the simulation, since these structures were simulated at a fixed frequency and with the effective refractive index of the fundamental mode as an input parameter. In addition, the laser (optical) mesh of the simulation covered only part of the AlGaAs cladding layers to reduce computing time. This was valid for the index guided lasers, but may have increased the source of error in these simulations for the gain guided lasers, because the optical mode spread over a much larger cross sectional area in these lasers than in the index guided lasers. Another source of error was the thickness of the n^+ GaAs layer. Since the first laser material had a 1.5 μm thick n^+ GaAs layer, and since ≤0.4 μm of n^+ GaAs was required for an optimized structure, as discussed previously herein, these simulations focus on a 0.4 μm thick n^+ GaAs layer. Thus, the error between the thickness of the n^+ GaAs layer of the fabricated device and that of the simulation may be as high as 15%, and this could be another reason for the discrepancy between the experimental and simulation results. An n^+ GaAs layer thinner than 0.4 μm could result in further reduction of the threshold current. On the other hand, an excellent match was found for the threshold current in the simulations for the p-ridge n-broad area structure with the same material structure and parameters in the next chapter, in Section 5.3.

5 Index Guided Thin Film Lasers

Index guided lasers are the commercial workhorses of optoelectronic applications because of their better spectral and spatial characteristics in comparison to gain guided lasers. The spatial characteristics are especially compatible with efficient coupling to optical fibers. Two designs for index guided thin film edge emitting lasers were fabricated and tested, both of which have broad area metal/metal bonds to Si or SiO_2/Si substrates. The first generation of index guided lasers, consisted of a self aligned p-ridge and a broad area metal contact, as discussed in Section 5.1. In Section 5.2, a slotted ridge structure more suited for manufacturing and planar integration is presented. Numerical simulations of these laser structures are presented in Section 5.3.

5.1 Index Guided I: Top p-Ridge, Bottom n-Broad Area Lasers[1]

The first index guided laser structure designed and fabricated was the top p-ridge, bottom n-side broad area contact laser bonded to Si. The process flow, along with photomicrographs of the fabricated structure is shown in Figure 5-1. First, the Ti/Pt/Au p-stripe was patterned and used as a self-aligned mask for wet chemistry etching of the ridge. After mesa etching to define individual laser bars, also with wet chemistry etching, the structures were encapsulated in Apiezon W, and the substrate was

[1] Excerpts appear in: S-Y. Cho, S. Palit, D. Xu, G. Tsvid, N. Jokerst, L. Mawst, T. Kuech, "Strain Compensated InGaAs/GaAsP Single Quantum Well Thin Film Lasers Integrated onto Si Substrates" in *20th Ann. Mtng. of the IEEE LEOS,* Lake Buena Vista, FL, USA, Oct 21-25, 2007, pp. 829-830. And
S. Palit, G. Tsvid, J. Kirch, J. Y.-T. Huang,, T. Tyler, S.-Y. Cho, N. Jokerst, L. Mawst, and T. Kuech, "Top-Bottom Stripe Thin Film InGaAs/GaAsP Laser integrated on Silicon," in *IEEE Device Research Conf.,*Santa Barbara, CA, USA, June 23-25, 2008. pp. 137-138.

selectively removed. At this point, the exposed n-side was blanket metallized with AuGe/Ni/Au. Next, a Mylar® diaphragm was used for device transfer. A double transfer was required so as to bond the n-broad area to the metallized Si substrate. A detailed fabrication recipe is available in Appendix A.2.

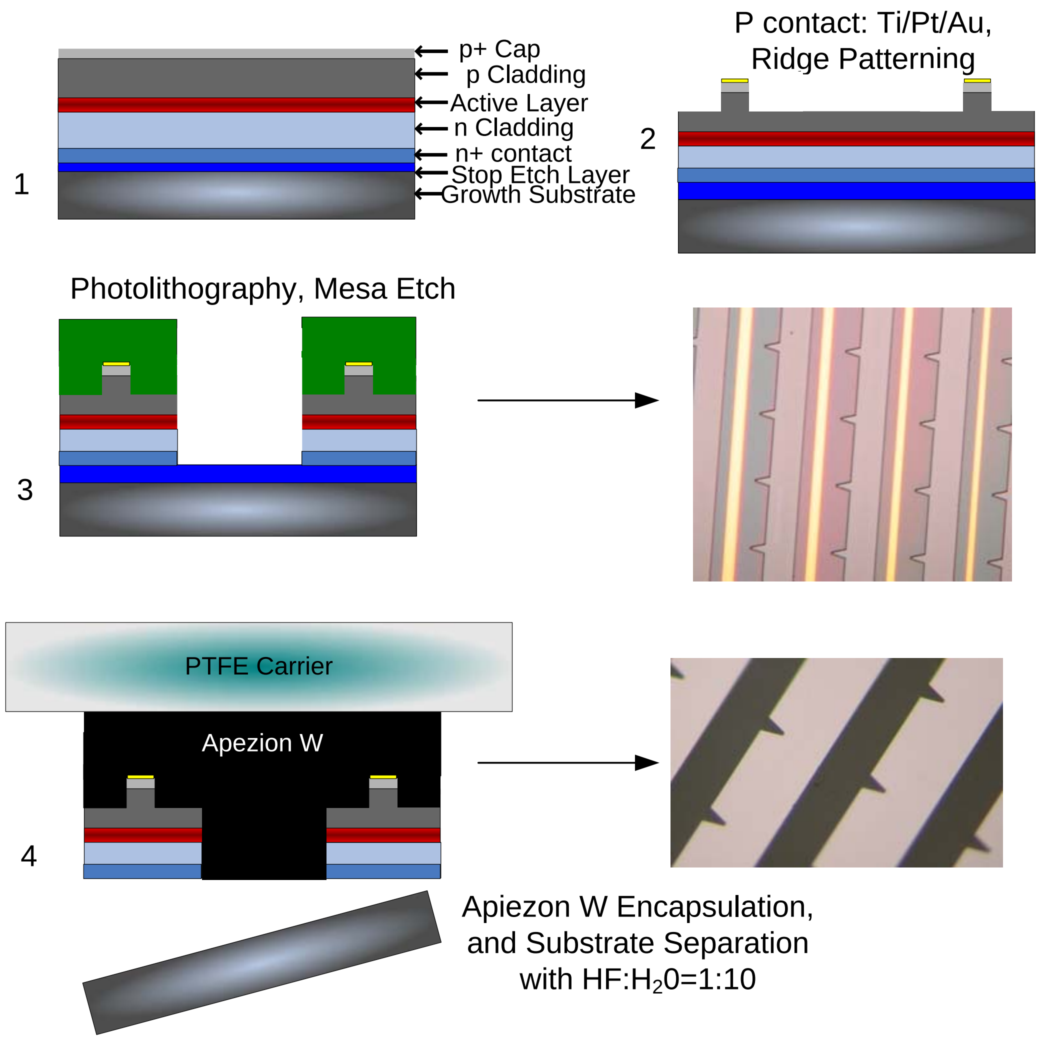

Figure 5-1. Process flow for top ridge bottom broad area contact laser; (1) Epitaxial structure of laser; (2) P stripe metallization and ridge etching; (3) Mesa etch to etch-stop/selective etch define individual laser bars; (4) Encapsulation of mesas in Apiezon W followed by selective etch of etch-stop layer to release substrate.

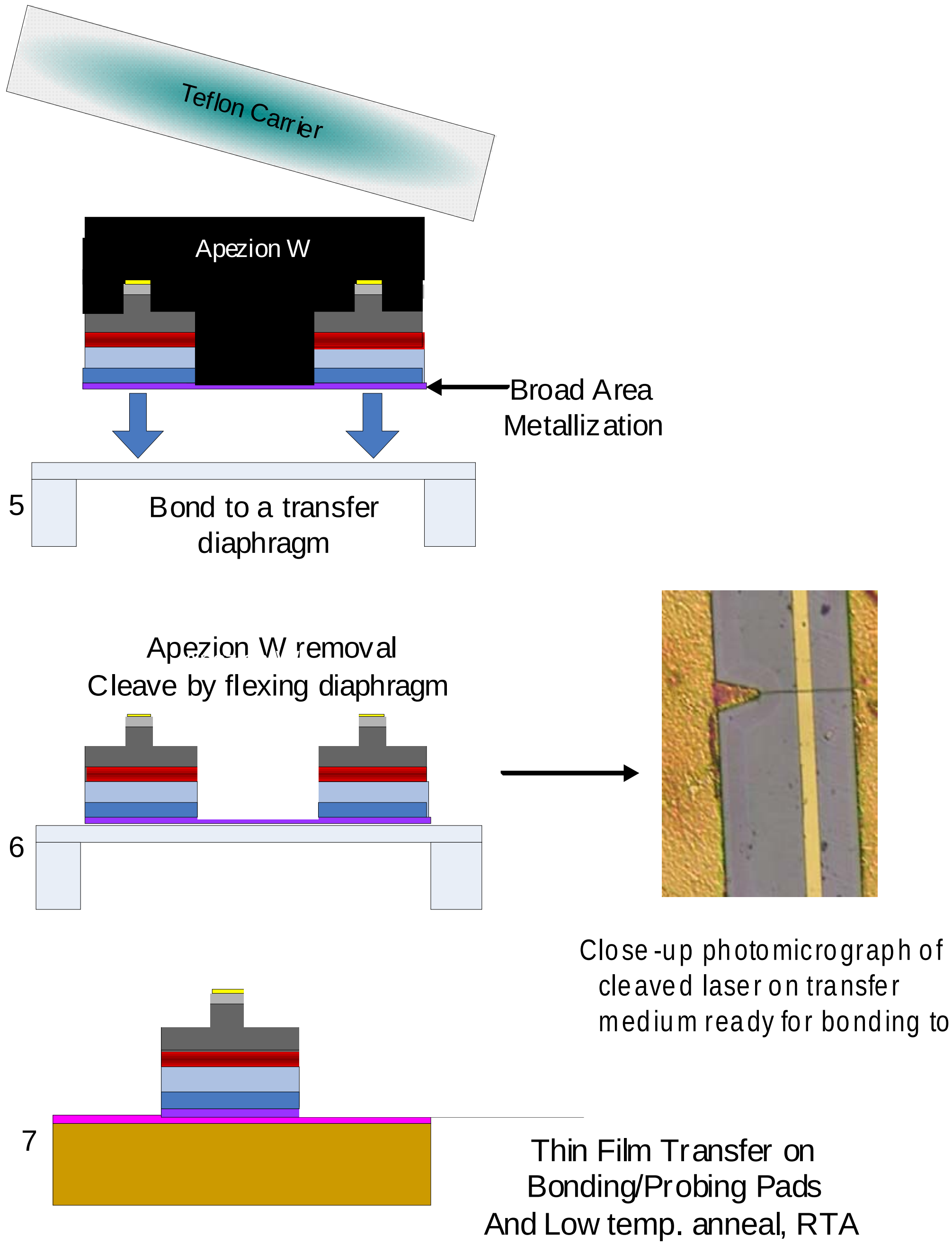

Figure 5-1 (continued). Process flow for top ridge bottom broad area contact laser; (5) Broad area metallization of n-side, followed by van der Waal's bonding to transparent Mylar® diaphragm; (6) Removal of Apiezon W; (7) Transfer to metallized Si via intermediate transfer diaphragm. Low temperature diffusion bonding at 180°C is followed by RTA at 365°C.

Figure 5-2 shows (a) a photomicrograph and (b) a scanning electron microscope (SEM) image of the top p-ridge bottom n-broad area contact thin film laser that was bonded to a Si substrate. The wedges on the edge were used to cleave the EELs to form mirror facets for the Fabry-Perot cavity, and were spaced 200μm apart. The cavity length is a multiple of this spacing, though masks designed for later fabrication runs (see, example, in Section 6) had larger cleaving edge spacings of 800 and 1000 μm.

(a) (b)

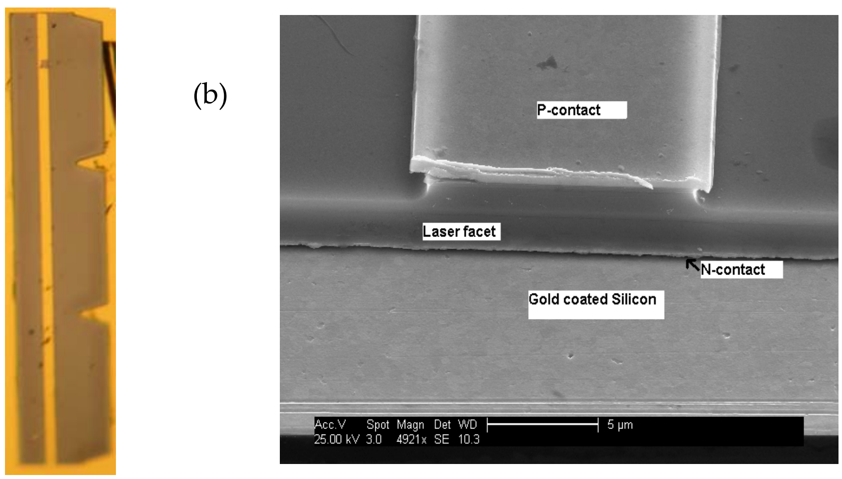

Figure 5-2. (a) A top p-ridge bottom n-broad area laser bonded to Au-coated silicon, with ridge width W=15μm, and cavity length L=600 μm (b) Scanning electron microscope (SEM) image showing one cleaved laser facet.

These lasers were probed and driven using a pulsed current source (ILX Lightwave, LDP 3811), which delivered a pulsed current of 0.5 μsec duration and 1% duty cycle. The output was measured by endface coupling the output to a single mode optical fiber connected to an optical spectrum analyzer (Ando AQ-6315E). The L-I characteristics were obtained by measuring the spectrum for different currents, and integrating the power over a fixed wavelength range. Since the outputs of these lasers were divergent, due to the narrow dimensions of the SCH in the vertical direction (a narrow aperture leads to a larger divergence, as discussed later in Section 6.2), only a fraction of the light was collected by the fiber. Results for one such laser, with a 25 μm stripe and ridge width, 1.1 μm ridge depth, 610 μm cavity length, and 130 μm mesa width are presented in Figure 5-3, indicating a lasing wavelength of 992 nm. The full-width half maximum linewidth of 0.6 nm was limited by the spectral resolution of the OSA (which was set at 50 pm). The measured threshold current of 37 mA, corresponding to a threshold current density of 242 A/cm^2, could be further reduced by reducing the width of the ridge. An 800 μm laser, also with a p-stripe and ridge width of 25 μm, was measured to have a threshold current of 75 mA, leading to a threshold current density of 375 A/cm^2. Thus, some device to device variability in the current density was observed, which is attributed to handling issues, especially due the step of cleaving these devices on the transfer diaphragm, where the broad area n-side metal connects all the thin film laser bars together.

The threshold current density of 242 A/cm^2 achieved for this lasers is the lowest reported that has been found in literature for thin film III/V ridge lasers integrated onto a silicon substrate. This low threshold current density is attributed to the strain compensated epitaxial structure employed for these lasers, and the placement of metal contacts that are on the top and the bottom, mimicking bulk lasers and enabling more efficient current pumping.

One of the drawbacks of this fabrication process, although it has been used by other researchers in the field [55, 64], is that the n-side metallization is performed while the device is still embedded in the supporting material (Apiezon W). While this process step does allow all the lasers to be metallized at the same time, it is an unstable step because Apiezon W starts to melt if the temperature in the vacuum deposition system is high. While deposition of Au/Ge/Ni/Au for the n-side contact was possible in the electron beam evaporation system, when the process change was made such that a AuGe (88-12 % wt) alloy was deposited using the thermal evaporation system, the Apiezon W softened and damaged the embedded thin film lasers. This is because the thermal evaporation system causes the evaporated alloy to have a much higher temperature than the electron beam evaporation. In one recent implementation of this kind of a ridge laser [63], the p-ridge side was planarized with the polymer benzocyclobutene (BCB) and then protected with a polymer that was later dissolved after substrate removal. The CW results are very encouraging. However, handling of these BCB planarized lasers in fluids with micropipettes obviates the transfer of large numbers of devices, though this is a possibility with thermal or UV release sheets (i.e. using industrial thin die handling techniques) [97, 98]. The cross-section of the p-top ridge n-broad area lasers is not rectangular, requiring planarizing techniques when integrating these lasers into planar systems. BCB, as discussed above [63], has been used as planarizing polymer, but the thermal CTE mismatch between the laser, the BCB, and the Si can cause stresses in the structure.

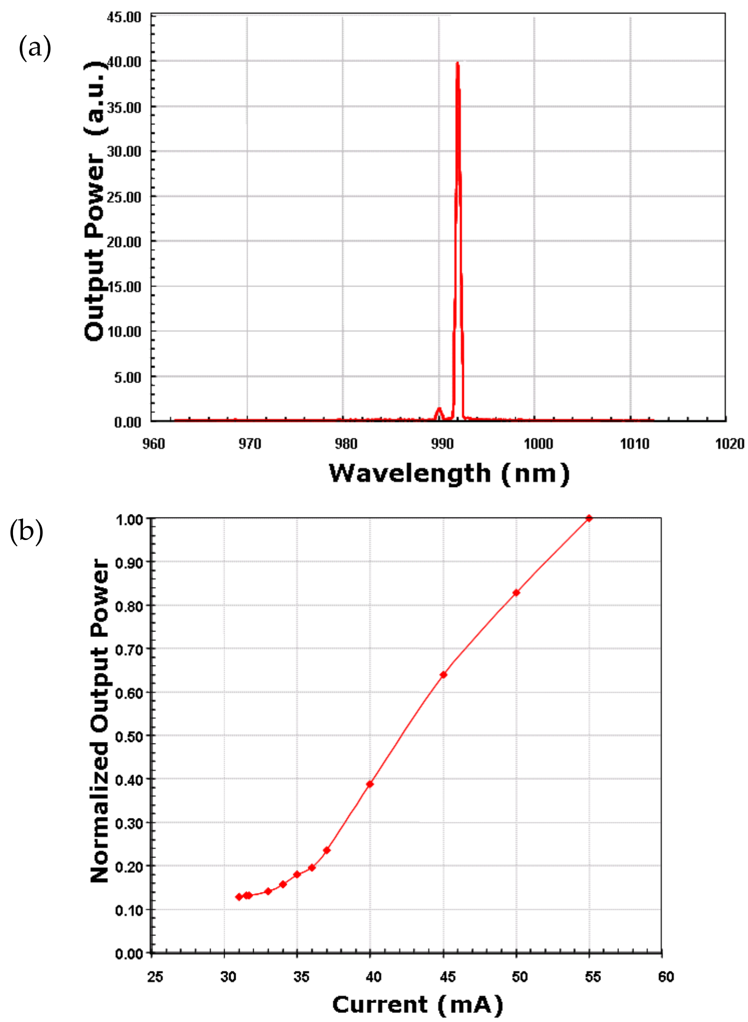

Figure 5-3. (a) Output spectrum for 610 μm top p-ridge bottom n-broad area laser, with a ridge width of 25 μm. A FWHM of 0.6 nm was obtained at a peak wavelength of λ=992 nm; (b) L-I for the laser indicates a threshold at 37 mA, corresponding to a threshold current density of 242 A/cm^2.

The temperature dependent characteristics of a laser are important to determine its behavior at CW measurements. The junction temperature of a laser increases during high-duty-cycle pulsed and CW measurements, leading to degradation in the L-I characteristics which manifests itself as an increase in the threshold current and a decrease in the slope efficiency. Thermal measurements were performed on this laser structure at the University of Wisconsin-Madison by Gene Tsvid and Jeremy Kirch. The dimensions of this structure differed from that reported above. The p-ridge was 50 μm wide and 1 μm deep (s shallower ridge than in the previous case), with a cavity length of 800 μm. The integrated laser was attached to a thermo-electric cooler and thermistor mounted on a copper chuck. The measurement system used a temperature controller to control the temperature, and an integrating sphere for calibrated power measurements. Pulsed mode operation was verified up to a stage temperatures of 67 ºC, indicating that the junction temperature could rise to 67 ºC (e.g. by using higher duty cycles), and, with no active cooling, the lasers would still lase. Further discussion regarding thermal measurements follows in the next section. The L-I results, as shown in Figure 5-4 (a), indicated a threshold current density of 400 A/cm^2, which was higher than threshold current density shown in the L-I characteristics in Figure 5-3 (b). This higher threshold current density may be attributed to a shallower ridge depth of 1 μm for this laser, compared to a 1.1 μm for the laser in Figure 5-3 (a), and imperfect cleaved facets, as discussed above. The I-V characteristic of the laser, as seen in Figure 5-4 (b), yields a high series resistance of 10-12.5Ω, indicative of poor electrical contacts. So, it is suspected that the ohmic contacts degraded over time.

(a)

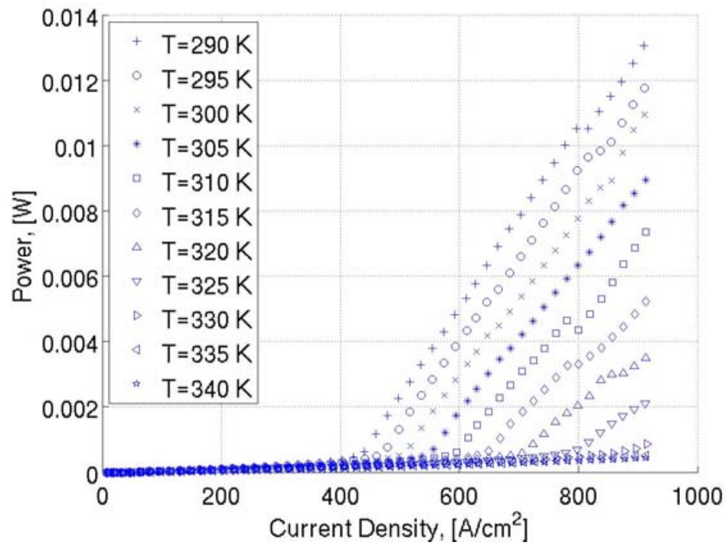

(b)

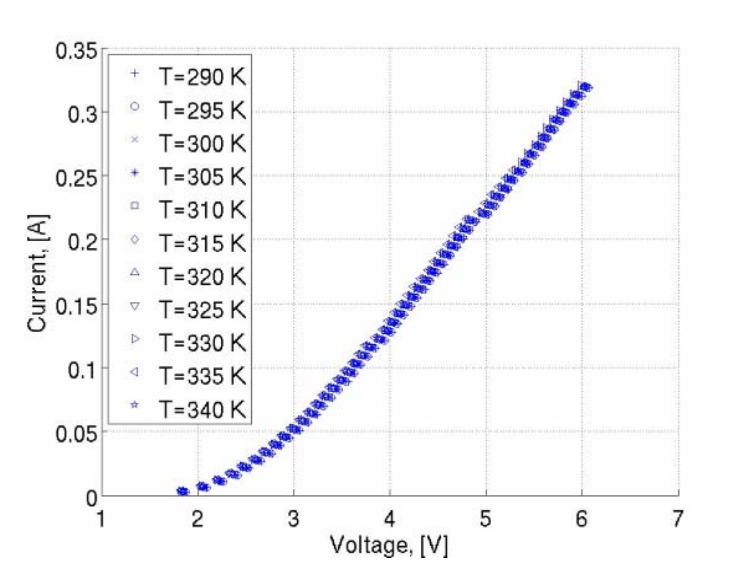

Figure 5-4. (a) Temperature controlled L-I characteristics for top ridge bottom broad area laser bonded to Si. Stripe width W= 50 μm, L= 800 μm, ridge depth 1 μm; (b) Corresponding I-V characteristics. Lasing operation is confirmed till 67 °C.

5.2 Index Guided II: p-Slotted Ridge, n-Stripe Lasers[2]

P-slotted ridge, n-stripe lasers combine the best aspects of both the rectangular cross sectional structure of the broad area bonded gained guided lasers in Section 4.2 with the p-ridge, n-broad area lasers in Section 5.1, as shown in Figure 5-5. In this EEL structure, slots are patterned on both sides of the p-stripe to form the p-ridge, enabling the rest of the oxide-isolated p-side to be broad-area bonded to the host substrate.

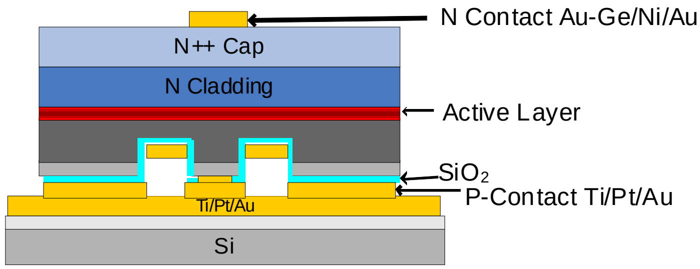

Figure 5-5. Schematic of p-slotted ridge, n-stripe thin film laser bonded to Au-coated SiO_2/Si.

Simulations later in this chapter indicate that there are electrically un-pumped areas outside the slots where optical modes are supported, however, despite this drawback; the threshold current density is comparable to that obtained from the p-ridge, n-broad area laser discussed in Chapter 4. In contrast to the lasers reported in Section 4, a stable fabrication process for patterning both sides of the index guided laser occurs while the laser is under the support of either the growth or host substrate, which is

---

[2] Excerpts appear in: S. Palit, J. Kirch, G. Tsvid, L. Mawst, T. Kuech, N. M. Jokerst, "Low Threshold Thin Film III-V Lasers Bonded to Silicon with Front and Back Side Defined Features", *Opt. Lett.*, vol. 34, 2802-2804, Sep 2009. and
S. Palit, J. Kirch, L. Mawst, T. Kuech, and N. Jokerst, "Thin Film P-Ridge N-Stripe III-V Laser Broad Area Metal-Metal Bonded to Silicon," in *CLEO/IQEC*, OSA, JWA38, June1-5, 2009, Baltimore, MD, USA.

superior to the process described in Chapter 4. A step-by-step process flow for these lasers is available in Appendix A.3.

As stated previously herein, GaAs substrate removal (by etching off the substrate from the laser epilayer) was more repeatable than selective lateral etching of an AlAs layer to separate the substrate from the epilayers. So, a new epitaxial laser structure, with a thinner GaAs n^+ contact layer of 0.4 μm, with an $In_{0.49}Ga_{0.51}P$ etch-stop layer was grown by Jeremy Kirch at University of Wisconsin-Madison.

Laser fabrication, as illustrated in Figure 5-6, began with p-stripe metallization of Ti/Pt/Au using lift-off photolithography, followed by dry etching 10 μm wide slots on both sides of the 40 μm wide p-stripe to define a 45 μm wide, 1 μm deep ridge to enable index guiding. This was followed by PECVD SiO_2 and patterning to electrically isolate the laser everywhere except at the p-stripes. Thereafter, the entire width of the laser was metallized. A mesa (defined by a photoresist mask) was selectively etched down to the InGaP etch-stop layer. After encapsulation in Apiezon W, and using a Teflon carrier, the GaAs substrate was etched away completely using a 1:8:1 solution of H_2SO_4: H_2O_2: H_2O. The InGaP etch-stop layer was then etched off selectively in concentrated HCl, leaving the p-side processed lasers embedded in Apiezon W with the n-side exposed, as shown in step 4 of Figure 5-6. The structure was then transferred to a Mylar®/transfer diaphragm where it adhered due to van der Waal's forces. The Apiezon W was removed using TCE, leaving the thin film devices bonded to the transfer diaphragm.

The laser device array was then peeled off of the Mylar® using a heat release sheet (Revalpha 319Y-4MS, Semiconductor Equipment Corp.), which could be flexed to cleave along previously photolithographically defined and etched wedges. Thereafter the sheet was heated to 120 °C to reduce the adhesion, such that individual lasers could then be bonded to a Mylar® transfer diaphragm. From the Mylar, the lasers were individually aligned and bonded to Ti/Pt/Au bonding pads on SiO_2/Si or Si. The lasers were placed close to the edge of the substrate to enable efficient light collection from the lasers, which was difficult if the lasers were located far from a host substrate edge. It is not possible to place the laser at the extreme edge of the substrate, since edge bead during photolithography for the n-stripe causes the n-stripe to resolve irregularly. The use of the thermal release sheet ensured greater adhesion during the flex/cleave process, and improved handling, significantly increasing the yield of the lasers available per process run. The threshold current densities for lasers of identical dimensions fabricated and cleaved using this procedure were very similar, confirming the reliability of the cleaving process. A diffusion metal/metal bond is created by heating the integrated structure to 180 °C for 10 minutes. The n-side was then patterned using a thick negative photoresist (> 3.6 μm, i.e. the thickness of the integrated laser). Next, the n-contact stripe of the laser was vacuum deposited and patterned using AuGe/Ni/Au and liftoff.

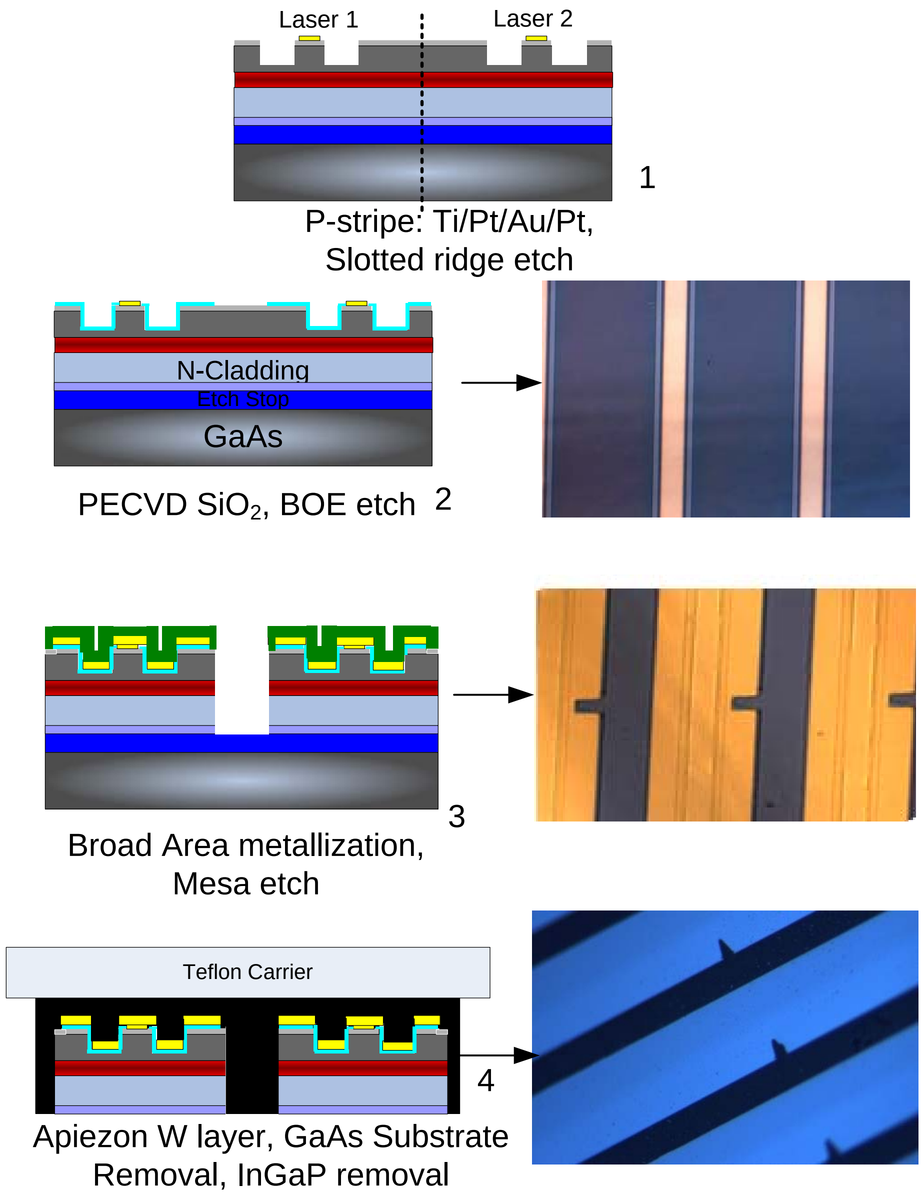

Figure 5-6. Fabrication process for p-slotted ridge n-stripe lasers integrated on Au-coated SiO_2/Si: (1) P-stripe metallization, and etching of slots on either side of stripe to form p-ridge; (2) Deposition of PECVD SiO_2 and BOE etch to remove SiO_2 from between lasers and to expose the p-stripe metal; (3) Broad area metallization, followed by mesa etch to etch-stop layer; (4) Encapsulation in Apiezon W, etching off of GaAs substrate and InGaP with chemically selective etchants.

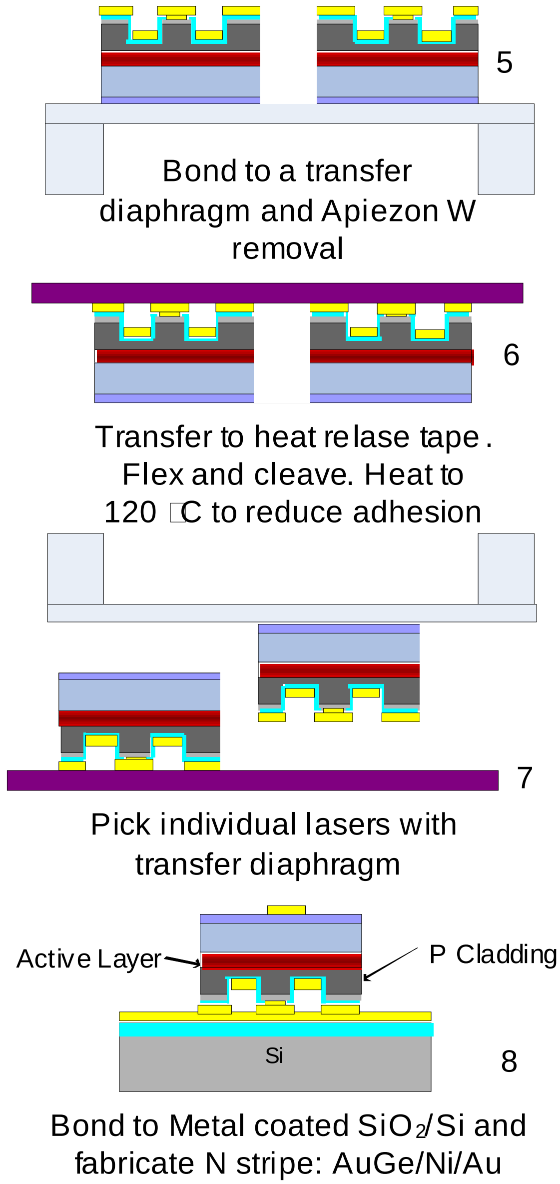

Figure 5-6. Fabrication process for p-slotted ridge n-stripe lasers integrated on Au-coated SiO_2/Si (continued): (5) Transfer to Mylar® diaphragm, removal of Apiezon W; (6) Transfer of laser array to heat release tape. Flex tape to cleave lasers. Heat to reduce adhesion; (7) Pick individual laser using transfer diaphragm; (8) Transfer and bond to metal pad on SiO2/Si. Anneal at low temperature for metal/metal bond. Perform negative photolithography, metal evaporation and lift off for n-stripe. RTA to achieve ohmic contacts.

(a)

(b)

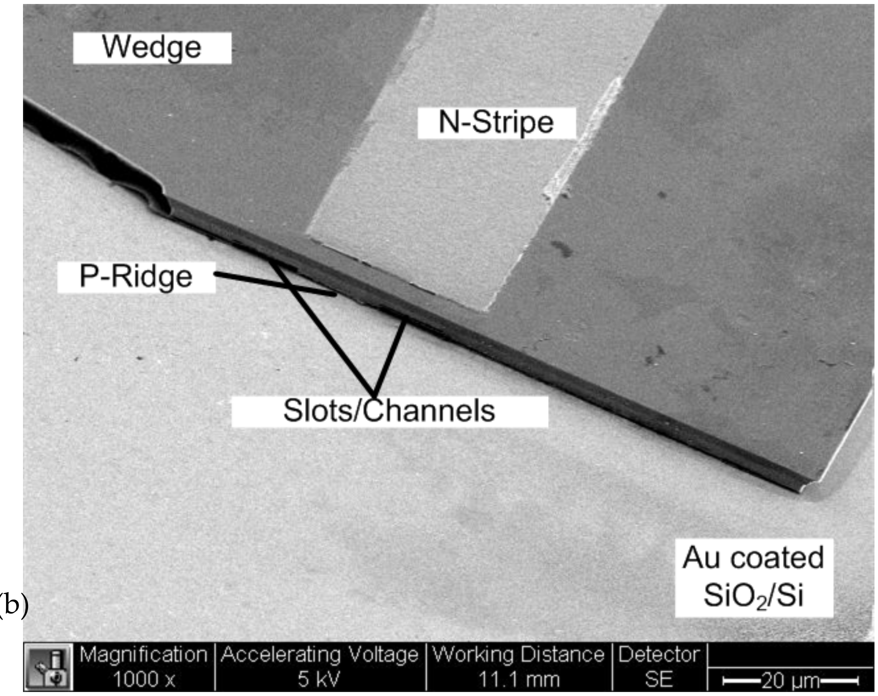

Figure 5-7. (a) Thin film p-slotted ridge, n-stripe laser on silicon (b) SEM image of one facet of the laser, showing the location of the p-ridge and n-stripe.

These lasers were tested with a 0.5 µs pulse width drive current at 1 KHz repetition rate from a laser driver (ILX Lightwave, LDP 3811). The L-I curves, obtained with Labview™ control of the experimental setup, were measured by collecting the optical output of the thin film laser integrated on Si with a HP 81521B optical photodetector head (a free space optical measurement) connected to a HP 8163A power meter. To capture the laser output spectrum, the laser output was incident on an aspheric lens coupled to a multimode fiber. This was connected to an OSA (Ando AQ-6315E) with spectral resolution of 50 pm. Due to the laser being recessed from the edge of the silicon substrate, and multiple reflections from the broad area gold pads on the silicon, it was difficult to reliably capture all of the light from the laser, dictating the use of an aspheric lens. However, this still did not capture all the light, hence, as in previous cases, this also is a measurement of relative power.

The spectrum and L-I curves in Figure 5-8 are for a slotted ridge laser with a 10 μm wide p-stripe, p-slotted ridge width of 15 μm and slotted ridge depth of 0.63 μm. The n-stripe is 30 μm wide. The laser cavity length is 1000 μm. The lasing wavelength is 995.05 nm and the threshold current density is 620 A/cm^2, calculated using the p-stripe width. This is a conservative estimate; the p contact/cap layer is highly conductive, so taking the entire ridge width into consideration would result in a threshold current density of 590 A/cm). The high threshold current density is a result of the shallow ridge depth because greater current spreading takes place into the p-cladding outside the shallow ridge, thus reducing the optical confinement factor.

A threshold current density of 250 A/cm^2 was measured for a slotted ridge laser with a p-stripe of 40 μm, p-slotted ridge width of 50 μm, and slotted ridge depth of 0.98 μm, as shown in Figure 5-8 (b). This is the lowest reported threshold current density for a narrow linewidth thin film laser, and second lowest for all thin film lasers, as shown in Figure 5-10. The width of the n-stripe is 40 μm and the laser cavity length is 800 μm. The threshold current density was calculated taking into account the entire p-ridge width of the laser due to the lateral current spreading in the highly doped p-AlGaAs contact layer. The variation in the center wavelength is attributed to growth variations between the two different parts of the wafer from where the devices were processed.

Figure 5-10 is a plot of threshold current densities, as found in literature, in comparison with this work. This is also the first set of thin film lasers integrated on silicon that are based on strain compensation in the active region.

(a)

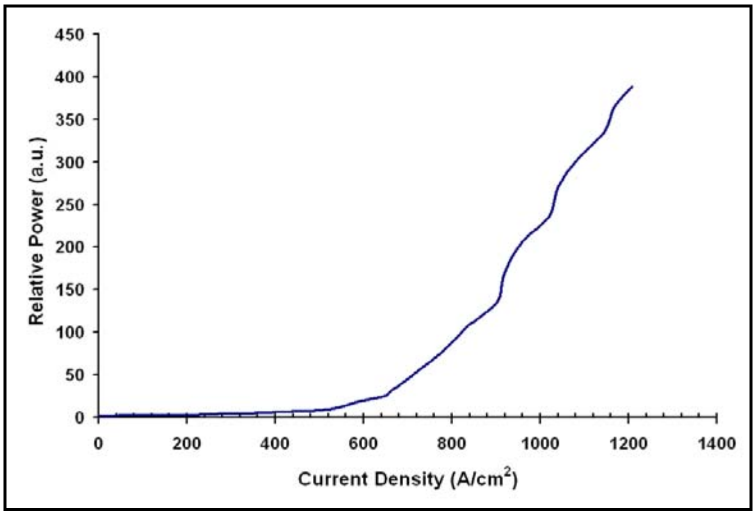

(b)

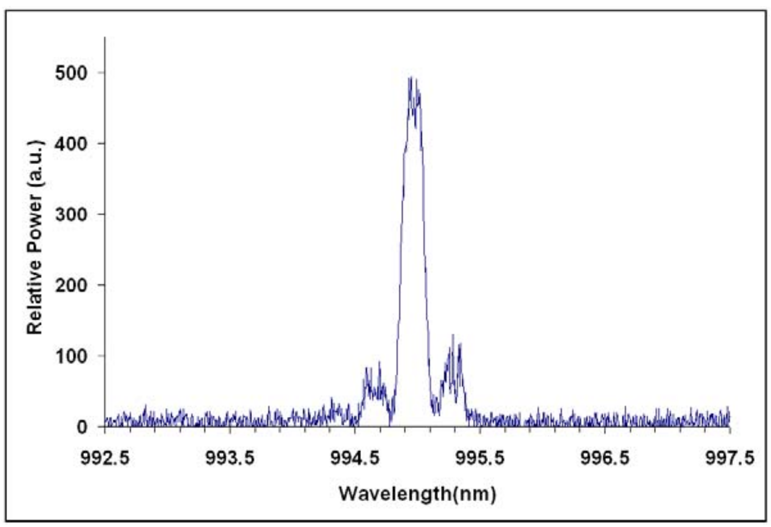

Figure 5-8. (a) L-I characteristics for p-stripe= 10 μm, slotted ridge width = 15 μm; (b) Spectrum with center wavelength at 995.05 nm, with a linewidth of 180 pm.

(a)

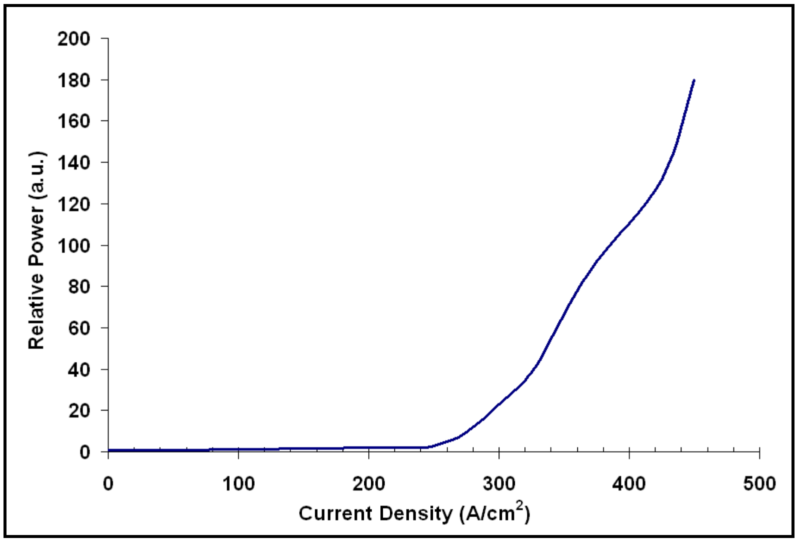

(b)

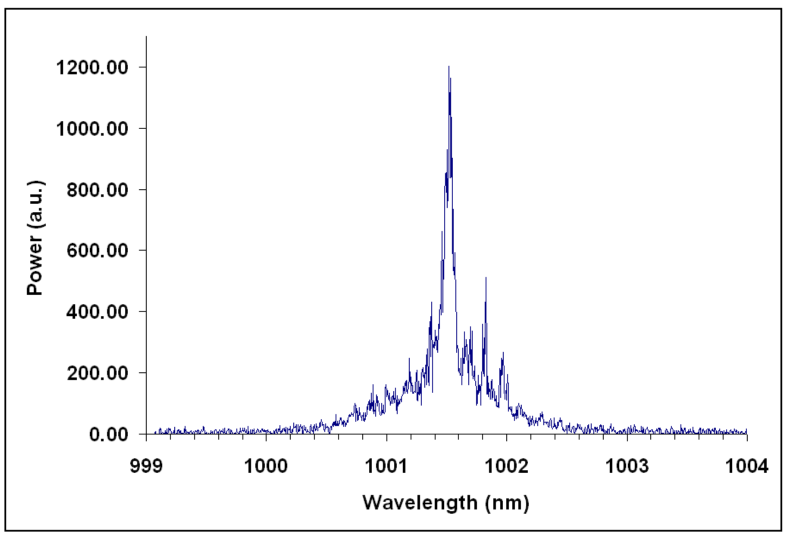

Figure 5-9. (a) L-I characteristics for p-stripe= 40 μm, ridge = 50μm; (b) Spectrum with center wavelength at 1001.52 nm with a linewidth of 78 pm.

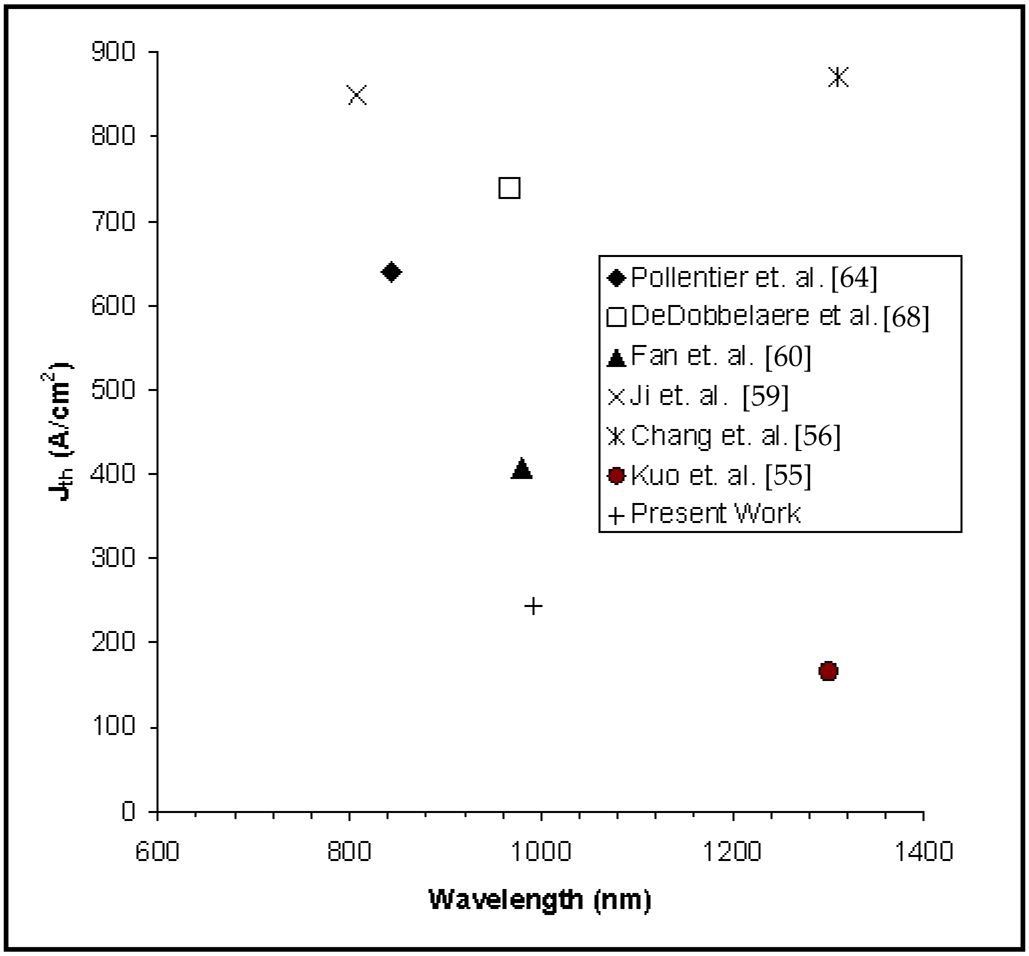

Figure 5-10. Comparison of threshold current densities for thin film lasers bonded to host substrate, with threshold current densities less than 1000 A/cm².

Thermal measurements on these lasers were also performed, as shown in Figure 5-11. These measurements were performed by bonding the integrated laser onto a copper block using thermally conductive grease. The copper block was mounted on a thermoelectric cooling (TEC) element with a 10K thermistor controlled by a Thorlabs TED 350 temperature controller. The temperature of the stage was varied from 22 °C to

60 °C and L-I curves were captured using Labview™. The values were fitted to the characteristic temperature equation:

$$I_{th} = I_0 e^{T/T_0} \qquad (5\text{–}1)$$

T_o was 49.8 ºK and I_0=67.2 mA. The T_o is low given the material system and is attributed to leakage from the shallow well, although it should be offset to some degree due to the GaAsP tensile barriers, which can also act as electron blocking layers. The value is comparable to the values of T_o for thin film lasers integrated on silicon [71], but the InGaAs/GaAs material used for these lasers typically has higher T_o value based on bulk laser measurements. The dependence of lasing wavelength on temperature was also measured, as shown in Figure 5-12 and is 0.389nm/ °C. This is typical for multimode single quantum well lasers based on bulk laser operation for this material system, and much better wavelength characteristics (essentially a smaller value of dλ/dT) can be obtained by the use of multiple quantum wells, operating in single mode, for example, DBR or DFB lasers [74, 99].

(a)

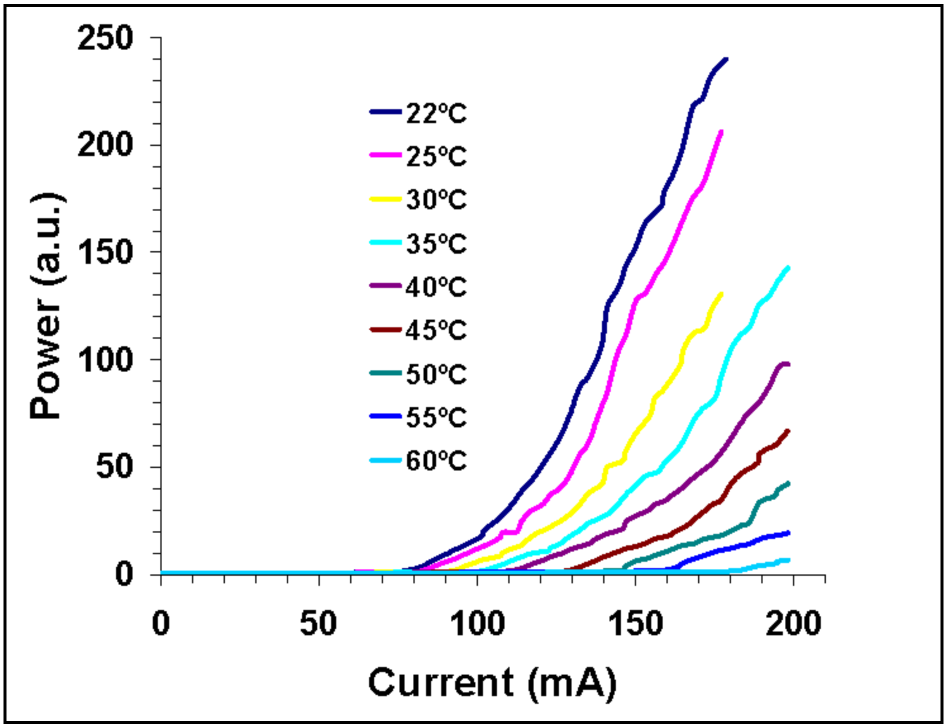

(b)

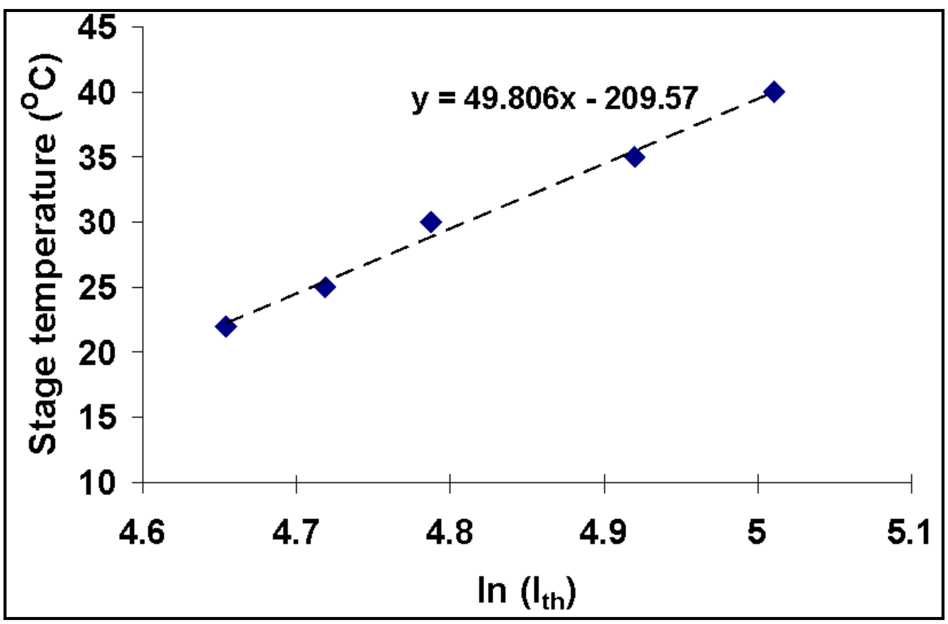

Figure 5-11. (a) L-I characteristics as a function of stage temperature; (b) Plot of stage temperature versus natural log of threshold current density.

(a)

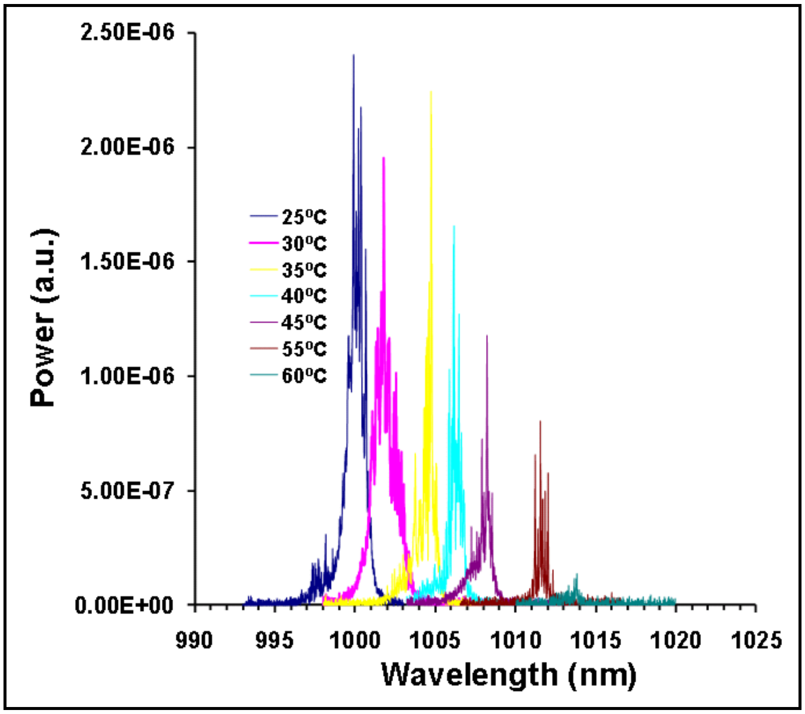

(b)

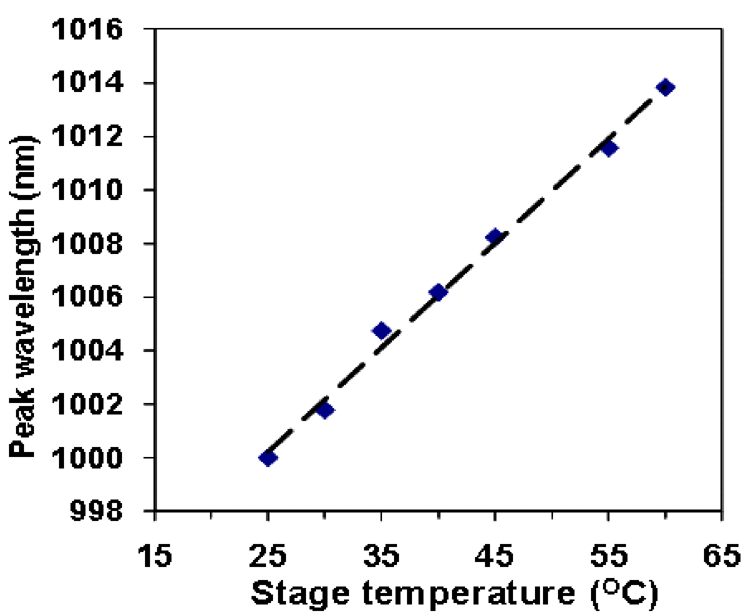

Figure 5-12. (a) Change in lasing spectrum with temperature, measured at 190 mA; (b) Plot of peak wavelength versus stage temperature leading to dλ/dT = 0.389 nm/ °C

Simulations done by our collaborators (Prof. Thomas Kuech) at UW-Madison predict a junction temperature of 67°C when integrating this on metallized Si. Based on the experimental results here, and for the p-ridge n-broad area lasers in Section 5.1, where the lasers were tested upto 340 K (67 °C), it will be possible to run these lasers in CW mode. The lasers herein were directly probed (positive probe on the metallized substrate as it is electrically connected to the p-contact, and negative probe on the n-stripe). The high current density at the probe tip when in contact with the thin laser contact metal led to rapid local heating and contact failure in the CW mode. In addition, the physical contact between the broad p-side metal contact and the metallized Si host substrate may have been non-uniform, since as only contact bonding and annealing without pressure was used, which could lead to local hot spots. This can be addressed in the future by using thermocompression bonding or AuSn solder to prevent the formation of voids in the metal/metal interface. I-V characteristics for the p-slotted ridge, n-stripe laser were also measured, and poor electrical contacts are evident from the jitter in the data (Figure 5-13). Derivative analysis, of both this data, and that for the p-ridge broad area laser (from Figure 5-4 (b)) did not indicate a smooth slope of $I\frac{dV}{dI}$ [100], indicating a changing series resistance. These poor electrical contacts could be to be fixed by using thermocompression bonding, ohmic contact characterization and process optimization, and wire bonded electrodes to enable reliable CW operation.

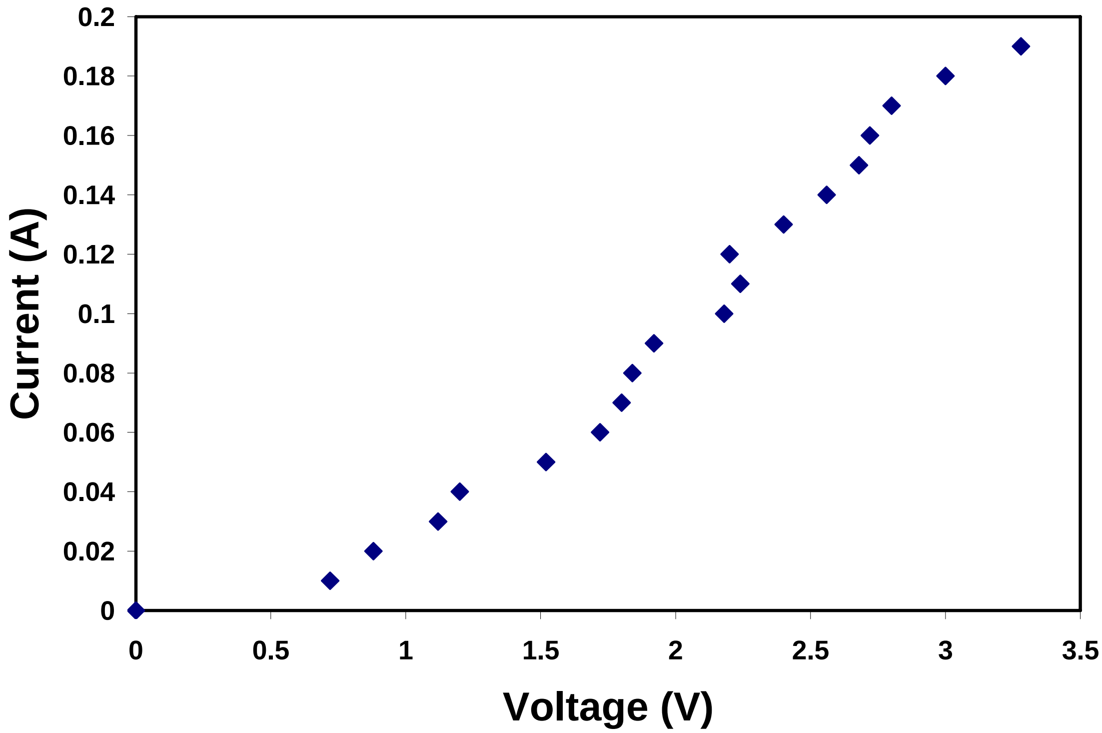

Figure 5-13. I-V characteristics for slotted p-ridge laser bonded on SiO_2/Si.

5.3 Simulations and Discussion

Silvaco™ simulations were performed both for the p-ridge n-broad area and the p-slotted ridge n-stripe lasers. Simulations for multiple longitudinal modes (calculated based on the cavity length by the simulator), as well as multiple transverse modes, resulted in comparable threshold currents. Simulations were performed for a single frequency while calculating multiple transverse modes, since this was computationally less intensive and time consuming, and yielded more information about the distribution of modes across the facet of the laser.

The index guided p-ridge n-broad area index guided laser was simulated first. The device and material losses (outside of mirror losses), lumped into the LOSSES parameter, was set to a value of 5 cm^{-1}, to obtain the best threshold current match with experimental data, and this was not changed between these simulations and the gain guided laser, as they both came from the same wafer growth. Typical values for this parameter range from 5 cm^{-1} to 30 cm^{-1} [101-103]. The material used was the same as in the case of the gain guided lasers, and all material parameters, including the loss factor, were kept identical. The code for this simulation is available in Appendix B.2. From the simulated result in Figure 5-14 (a), a threshold current of ~35 mA is predicted, as compared to the experimentally observed result of 37 mA. This ridge structure supported most of the lower order modes (1-4) and some higher order modes as well, as indicated in the Figure 5-14 (a). The number of modes that were supported was a function of the ridge depth and width. A deeper ridge would support a larger number of higher order modes, due to the increased difference in the effective index between the ridge and the rest of the laser, unless accompanied by a corresponding reduction in ridge width. Figure 5-14 (b) shows a plot of the fundamental transverse mode, which is supported by the laser since it is located below the ridge, and overlaps with the pumped region, further supporting the L-I characteristics in Figure 5-14 (a) where the theoretical I_{th} is well predicted for the fundamental mode. It must be noted that in this laser, similar to the p-slotted ridge n-stripe laser to be discussed next, the optical modes are a function of the changing refractive index due to current injection, and for any particular application, must be characterized for the particular current and the optical power that they are operated at.

(a)

(b)

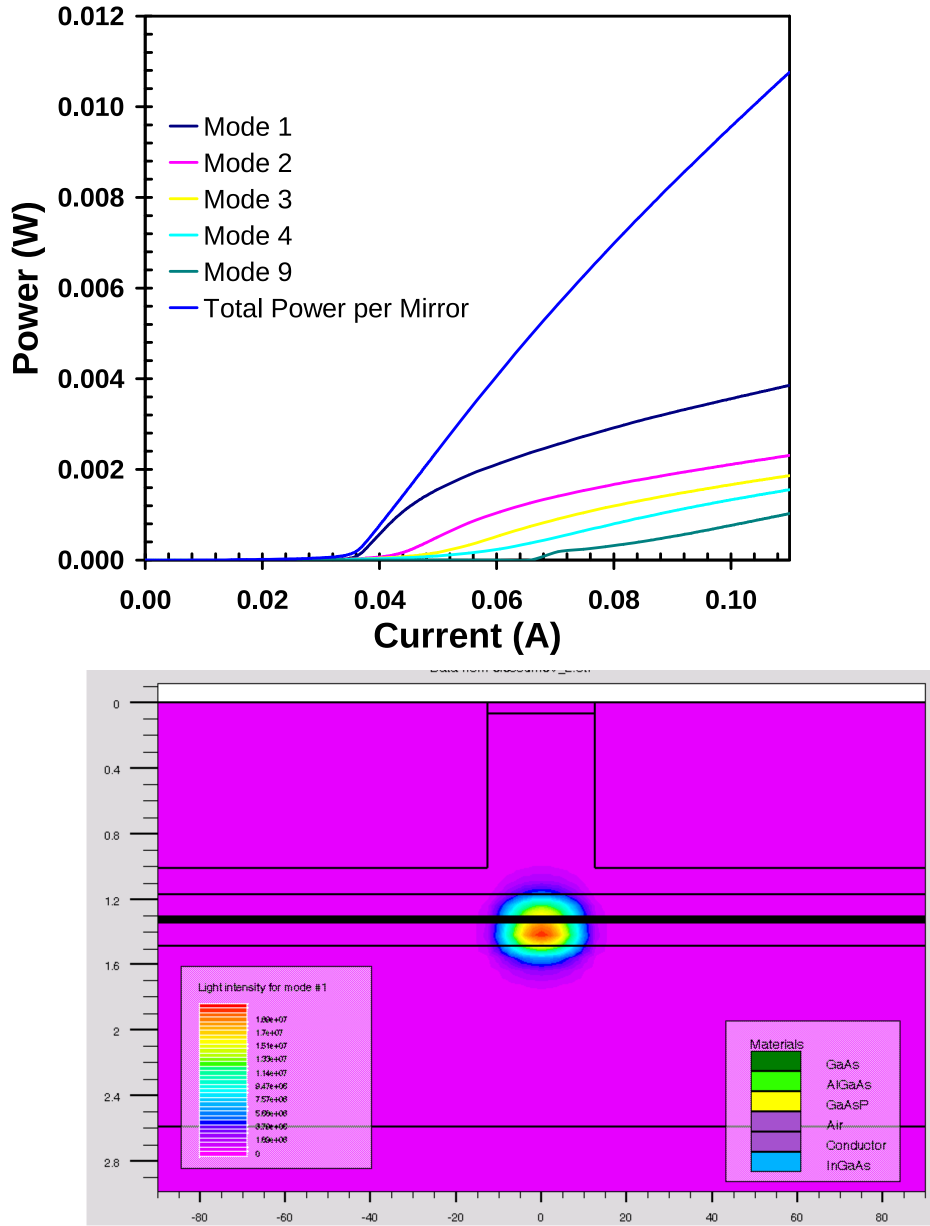

Figure 5-14. (a) Simulated L-I curve for the p-ridge n-broad area laser, with p-ridge width = 25 μm, depth = 1.1 μm, indicating I_{th}=35 mA, compared to experimental value of 37 mA. (b) Fundamental optical mode supported by the laser.

A new wafer growth was used in the case of the second index guided laser, i.e. the p-slotted ridge, n-stripe laser, in which the thickness of the n^+ GaAs layer was reduced from1.5 μm to 0.4 μm, and the composition of the etch-stop layer was changed to InGaP from AlAs, for reasons discussed in Section 5.2. The device and material losses (lumped into the LOSSES parameter), the only fitting parameter that is being used in the simulations, was estimated to be 10 cm^{-1} in this case, as opposed to 5 cm^{-1} for the gain guided lasers and for the p-ridge, n-broad area lasers, both of which used the same (first) wafer growth. The simulation code is available in Appendix B.3. Figure 5-15 is a simulation for an 800 μm p-slotted ridge, n-stripe laser with p-slotted ridge width = 50 μm, p-stripe width = 40 μm, ridge depth = 0.98 μm, and n-stripe width = 40 μm. The threshold current was calculated to be 92 mA, corresponding to a threshold current density of 230 A/cm^2, compared with the experimental value of 250 A/cm^2. The fundamental and lower order modes are not supported as a result of the wide ridge, and the narrow slots. The current density in the vertical direction is shown in Figure 5-15 (b). Again, in this case, the current spreading due to the highly doped n^+ GaAs contact layer is evident.

Similar simulations were performed for a 1000 μm laser with all parameters remaining same (Figure 5-16), and the corresponding supported modes are shown. The lower modes go into the unpumped regions on either side of the slots. The simulated threshold current is found to be 130 mA, corresponding to a threshold current density of 260 A/cm^2.

(a) (b)

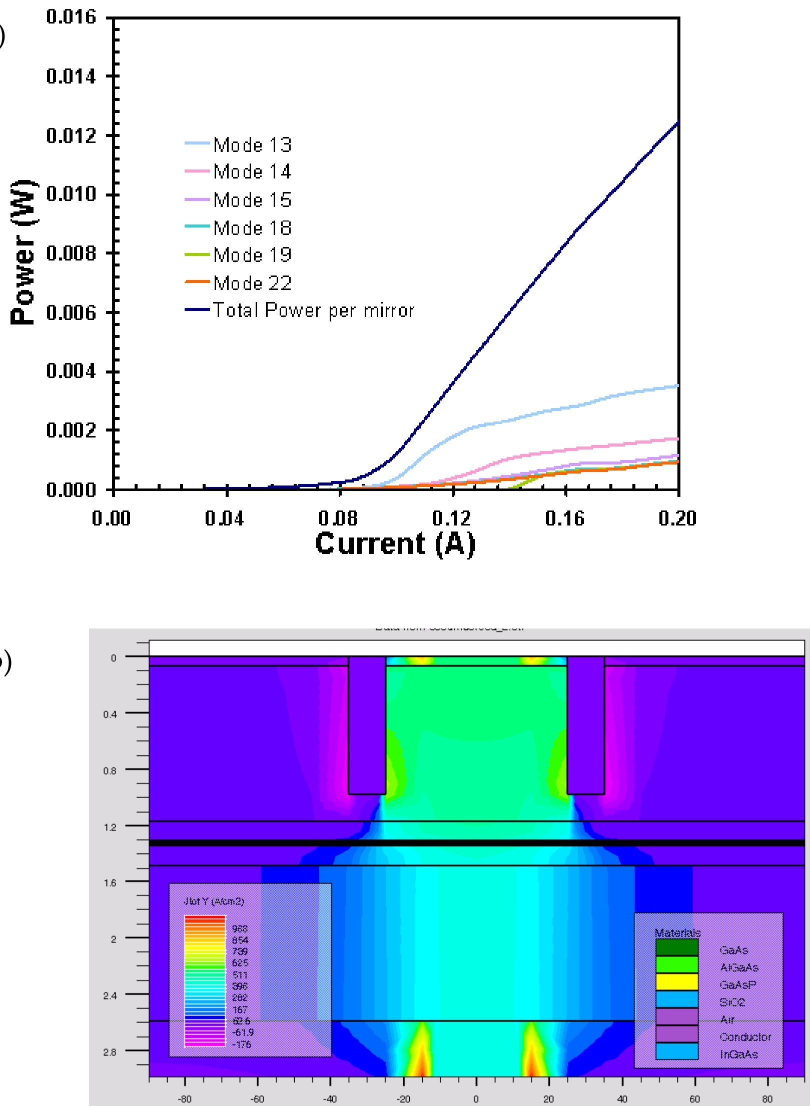

Figure 5-15. (a) L-I characteristics for p- slotted ridge n-stripe 800 μm laser with ridge width = 50 μm, p-stripe width = 40 μm, ridge depth = 0.98 μm, and n-stripe width =40 μm, indicating supported higher order modes (b) The current density in the vertical (Y) direction.

(a)

(b)

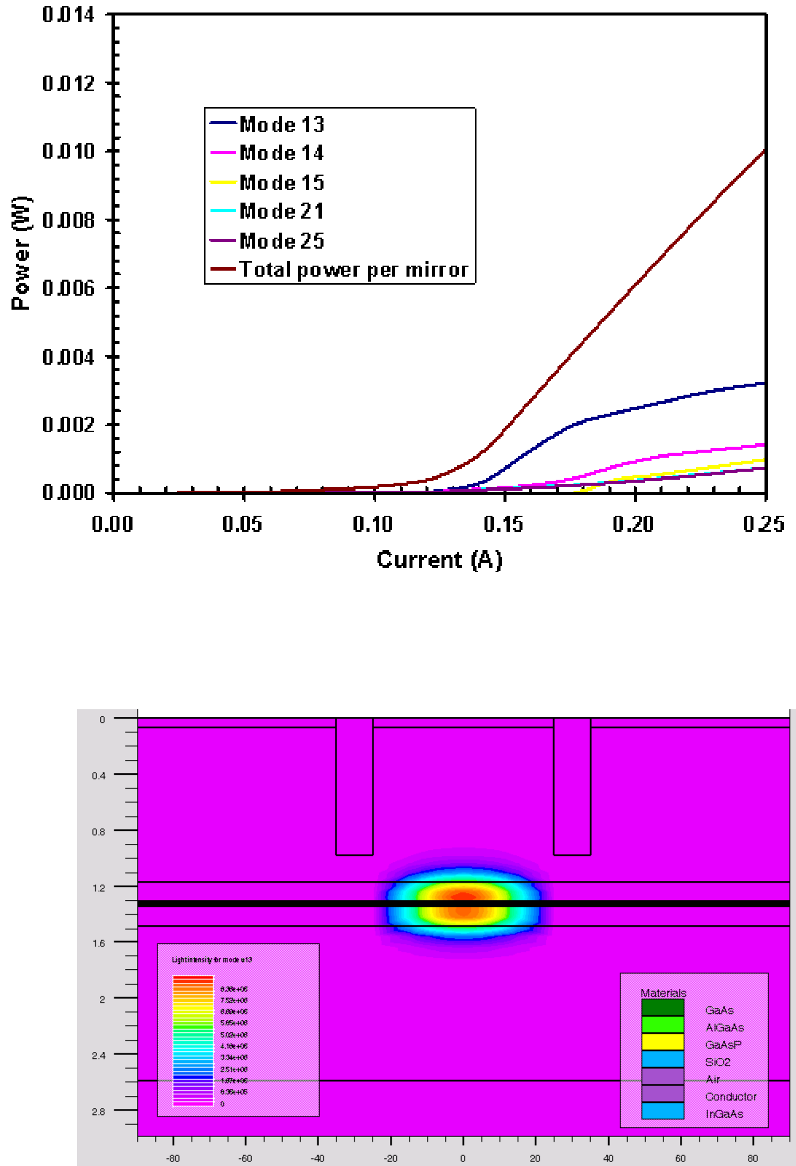

Figure 5-16. (a) L-I characteristics for p-ridge n-stripe 1000 μm laser with ridge width = 50 μm, p-stripe width = 40 μm, ridge depth = 0.98 μm, and n-stripe width =40 μm, indicating supported higher order modes (b) Supported higher order transverse mode

5.3.1 Incorporation of N-ridge

Another aspect that was theoretically explored was the incorporation of a ridge on the n-side in addition to the p-side. This is possible for a thin film EEL implementation, as the n-side can be etched after patterning the n–stripe electrode. For this, two configurations were theoretically simulated. One was the existing slotted ridge structure with 1 μm ridge depth, with an additional ridge etched into the 0.4 μm n^+ GaAs contact. This is shown in Figure 5-17 (a). In Figure 5-17 (b), a symmetric ridge of 0.5 μm is etched on each side, i.e. the ridge depth of the slotted p-ridge was also reduced.

(a)

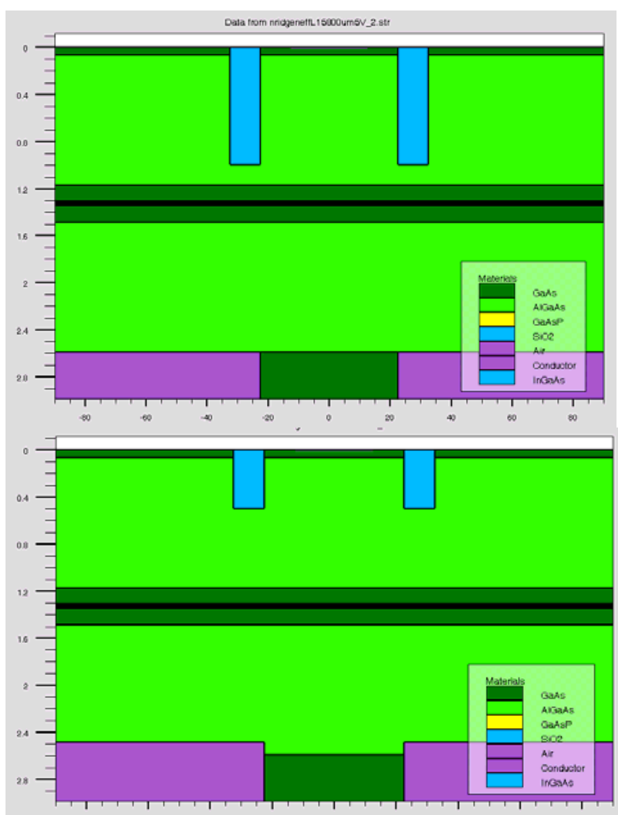

(b)

Figure 5-17. p- slotted ridge n-ridge structure. (a) Existing p-slotted ridge structure of 1 μm p-ridge depth with 0.4 μm n- ridge etch depth. (b) "Balanced" ridge structure where the original ridge depth of 1 μm is divided equally between the p and n-side.

The L-I characteristics of both were compared to the 1 μm slotted p-ridge n-stripe structure, and this is shown in Figure 5-18. This figure shows that there is very little change in the threshold current due to the n-ridge, indicating that the reduction of the threshold current is primarily driven by controlling the current flow in the p-region using the ridges. However, the higher refractive index difference due to etching the n-ridge would cause higher order modes to be supported.

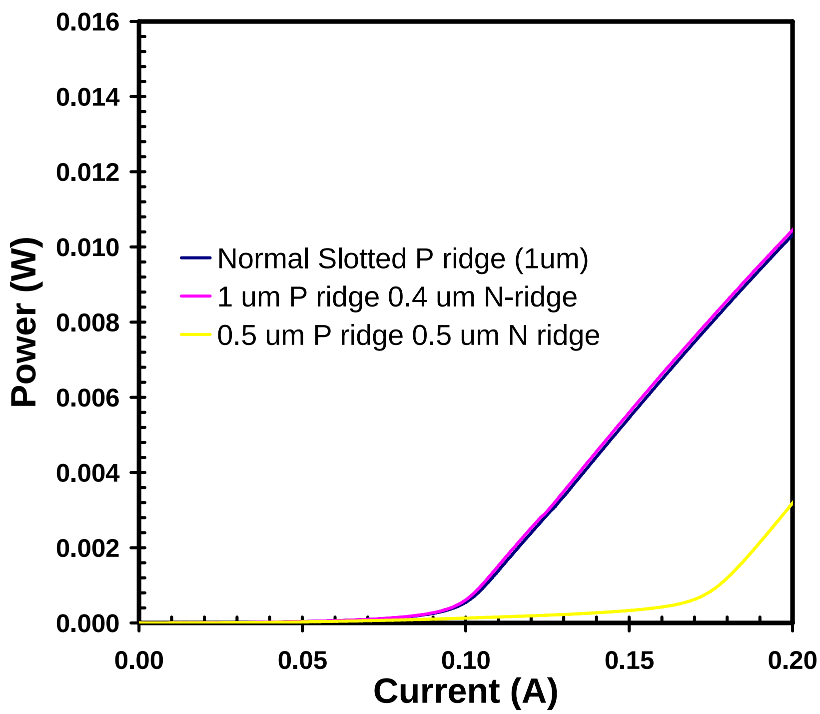

Figure 5-18. Comparison of L-I characteristics of p-slotted ridge of 1 μm, p-slotted ridge of 1 um with 0.4 μm n-ridge, and p-slotted ridge of 0.5 μm depth with 0.5 μm n ridge.

Alternate configurations might be advantageous, for example, where the p-ridge is narrow and shallow, and slots are wide, so that the fundamental mode can be supported. Then the effect of the n-ridge would need to be reexamined. However, for the configurations explored in this thesis, where the slots are fairly narrow and the ridges are wide (essentially to have a good bonding area with the Si substrate), the simulations indicate no advantage for the implementation of the n-ridge.

It is interesting to contrast results from the two types of index guided lasers. In the p-ridge n-broad area laser, a smaller loss parameter of 5 cm^{-1} was required for the simulations to agree with the experiment, as compared to the higher loss parameter of 10 cm^{-1} for the p-slotted ridge lasers. This can be attributed to the wafer growth, as well as the differing device structures, since the p-slotted ridge, n-stripe laser supported higher order, lossier modes. Also, there was a drop in simulated slope efficiency for the p-slotted ridge, n-stripe lasers (approximately 0.1 W.A as compared to 0.15 A/W in the p-ridge broad area lasers), which can again be attributed to the support of higher order modes in the p-slotted lasers. In general, the slope efficiencies of these lasers were low, indicating that there may be other loss mechanisms, for example, due to light absorption in the metal. In the p-slotted ridge n-stripe laser, the simulation does not take into account the loss mechanisms due to the broad area metal that is patterned on top of the SiO_2. This may an additional loss factor for the p-slotted lasers which demanded the use of a larger loss factor when comparing experiments to simulations.

6 Thin Film Edge III-V Edge Emitting Lasers Integrated with Polymer Waveguides on SiO_2/Si

The planar integration of lasers and waveguide structures are a critical step toward the realization of chip-scale optical integrated systems. This chapter reports on this integration, and presents results for a passively aligned waveguide structure while maintaining low threshold current densities and decreasing the tight alignment tolerances typically required to align lasers to waveguides in the direction of light propagation. The results herein are the lowest threshold current densities reported to date for an EEL integrated with a waveguide. Section 6.1 describes the tapered SU-8 waveguides used for this dissertation. In Section 6.2, the conventional implementation of thin film lasers and waveguides is described, where there is a separation between the laser facet and the waveguide. In Section 6.3, leveraging the ability to integrate both the laser and waveguide onto the same substrate, an embedded facet/overlapping waveguide configuration has been demonstrated.

6.1 Polymer Waveguides

Polymer waveguides are very attractive from the perspective of ease of processing (particularly for photoimageable polymers) and low cost for integrated systems. In addition to their ease in processing using standard spin coat and photolithography techniques, they have a range of refractive indices between 1.3 and 1.8 [104] to choose from and have well characterized optical performance [105, 106]. A great deal of research effort has also been directed towards polymer-based sensing elements for chemical and biological sensors. Polymer- based chemically selective membranes can be used as a coating on other optical sensors [107], and polymer micro ring/disk resonators [108-112] and Mach Zehnder interferometers have been used as optical sensing components [113-115]. However, the refractive index contrast for polymer-based waveguides is lower than that achievable for crystalline semiconductors, requiring larger footprints on the substrate and lower quality factors (10^5) for microring resonators, for example [116]. However, this is outweighed by the ease of fabrication, and material costs for some applications, and clinically relevant detection limits, for example, of glucose, are possible [109]. Also, 3D stacking of devices and circuits can be made possible using polymers as filling layers.

SU-8-2002 was selected for the waveguide core material due to its low optical loss at λ=990 nm, bio-compatibility [117] and photoimageability. It has a refractive index of 1.56 at λ=990 nm. An asymmetric tapered waveguide composed of air/SU-8/SiO_2/Si was implemented for this thesis. RSoft-BeamPROP simulations were performed to characterize power coupling and propagation through the tapered waveguide. Wide angle 3D BPM (in contrast to basic paraxial BPM) was performed due to the high index contrast and taper. The SU-8 waveguide was adiabatically tapered from 86 μm wide to 8 μm wide over a length of 1.6 mm, resulting in very little loss due to the long taper of the waveguide itself. However, the dimensions and shape of the mode launched into the waveguide have a profound impact on the power coupling as is shown in Figure 6-1.

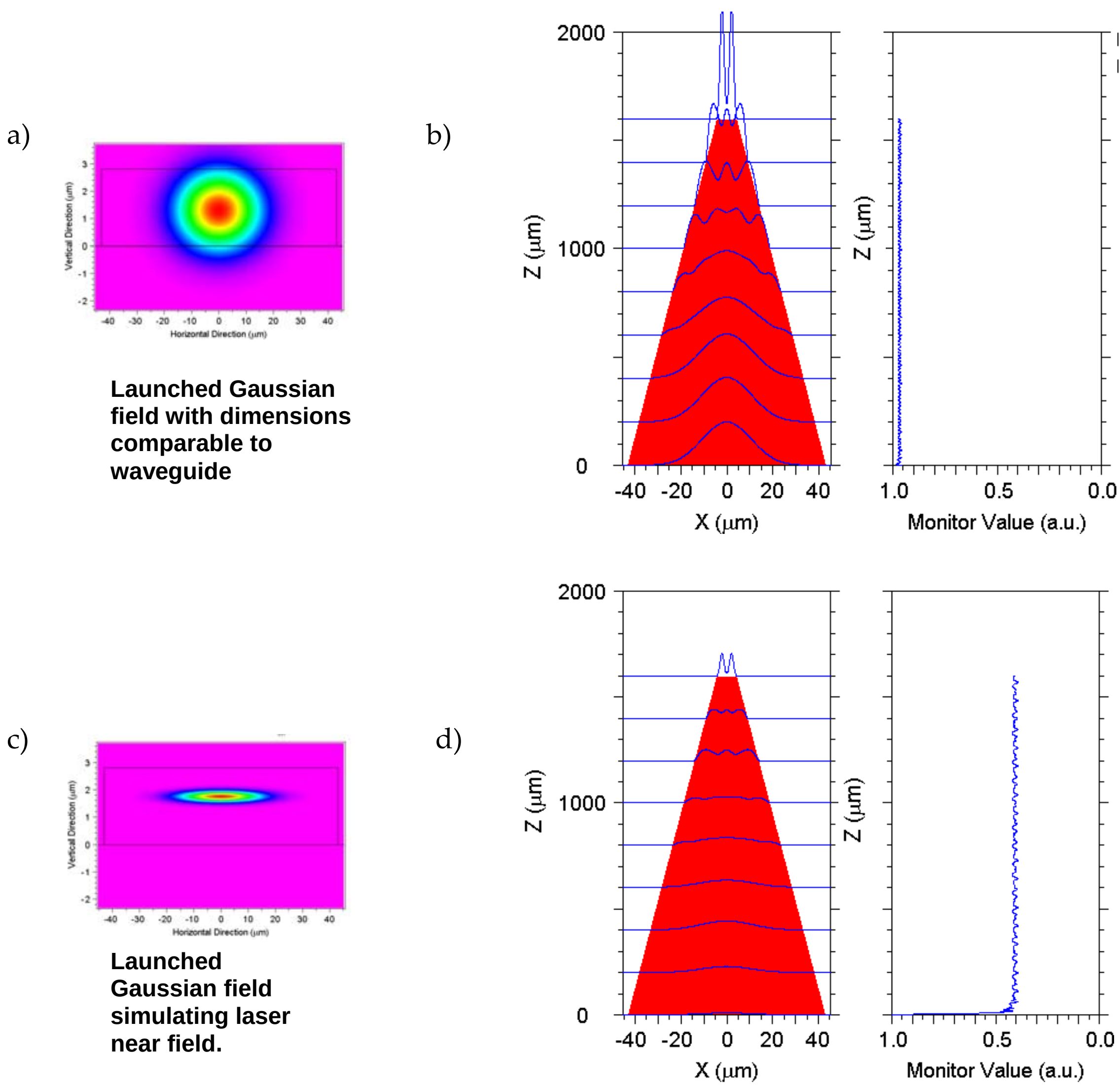

Figure 6-1. 3D RSoft BeamPROP simulations for tapered waveguide: (a) Launch field is a Gaussian mode with dimensions comparable to the height of the waveguide; (b) Corresponding propagated wave and waveguide power; (c) Launch field with a Gaussian mode simulating the laser facet output; (d) Corresponding propagated wave and waveguide power.

Figure 6-1 illustrates a comparison for two different launched modes: in the first case, a Gaussian mode with vertical dimensions comparable to the waveguide is launched. There is very little loss. In the second case, a Gaussian mode that is highly compressed in the vertical region (essentially dictated by the core width of the SCH laser structure) is launched. The mode mismatch results in a significant initial loss.

6.2 Thin Film Lasers End Fire Coupled into Polymer Waveguides[1]

2D laser to waveguide coupling simulations were also performed using COMSOL™, a commercial finite element method (FEM) solver. In this case, the laser epitaxial structure was also included in the simulation; it was modeled as a passive semiconductor waveguide, with an output that was incident on the SU-8 waveguide. The low index contrast between the SU-8 and the SiO_2 and high divergence of the laser resulted in significant cladding modes as shown in Figure 6-2. The divergence of a laser diode in the vertical dimension is given by the approximation [74]:

$$\theta = \frac{\lambda}{2w_0} \tag{6-1}$$

where θ is the half angle of divergence, λ is the wavelength of light in air, and ω_0 is the thickness of the active layer. For the 0.4 μm thick SCH structure, for λ=0.99 μm, the divergence angle θ in the vertical direction is 70.9°. The half-acceptance angle θ_a for the waveguide is given by the formula:

$$n \sin\theta_a = \sqrt{n_1^2 - n_2^2} \tag{6-2}$$

---

[1] Excerpted from: S. Palit, J. Kirch, L. Mawst, T. Kuech and N. M. Jokerst, "Heterogeneous integration of thin-film compound semiconductor lasers and Su-8 waveguides on SiO2/Si", in *Proc. SPIE*, 2010, vol. 7607, San Francisco, CA, pp. 76070S 1-8.

where n is the refractive index of the medium, in this case, air (i.e. the gap between the laser and the waveguide), n_1 is the refractive index of the SU-8 core, i.e. 1.56, and n_2 is the refractive index of the cladding, which is air on top, and SiO_2 on the bottom. From the formula, θ_a decreases with increasing n_2, hence, in this asymmetric waveguide, the SiO_2 cladding will limit the acceptance angle, and n_2 is assigned the value of the SiO_2 cladding, i.e. 1.48. This results in θ_a =29.5°. Now, $\theta > \theta_a$, and so the light of the laser outside the acceptance cone of the waveguide projects into the air on the top, and manifests itself as substrate modes in the SiO_2 cladding.

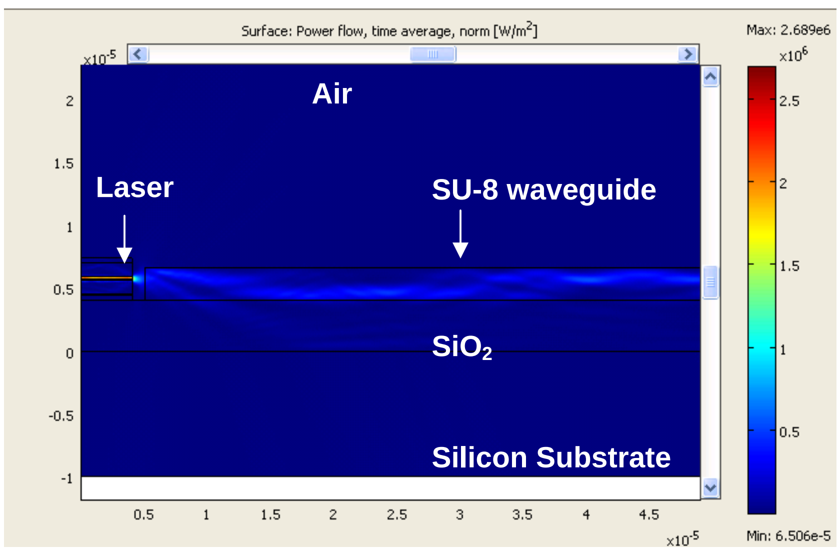

Figure 6-2. 2D COMSOL simulation illustrating propagation of laser light through Air/SU-8/SiO_2/Si waveguide. An air gap of 1 μm exists between the laser and the waveguide facet. Significant cladding modes are seen.

The fabrication process for the integrated laser/waveguide system involved first bonding a cleaved thin film p-slotted ridge n-stripe laser (without the n-stripe) onto a square metal pad on SiO_2/Si, followed by photolithography and metallization for the n-stripe on the exposed surface of the bonded thin film laser. This was followed by spin coating SU-8 2002 and photolithographically patterning it after aligning the negative photomask pattern with the facet edge of the laser, as shown in Figure 6 (a-c). A photomicrograph of the final fabricated system is shown in Figure 6 (d). The p-slotted ridge laser ridge is 50 μm wide, p-stripe width is 40 μm, n-stripe width is 30 μm, the cavity length is 800 μm and the waveguide tapers linearly from 86 μm to 8 μm over 1.6 mm. The distance between the laser and the waveguide is >25 μm.

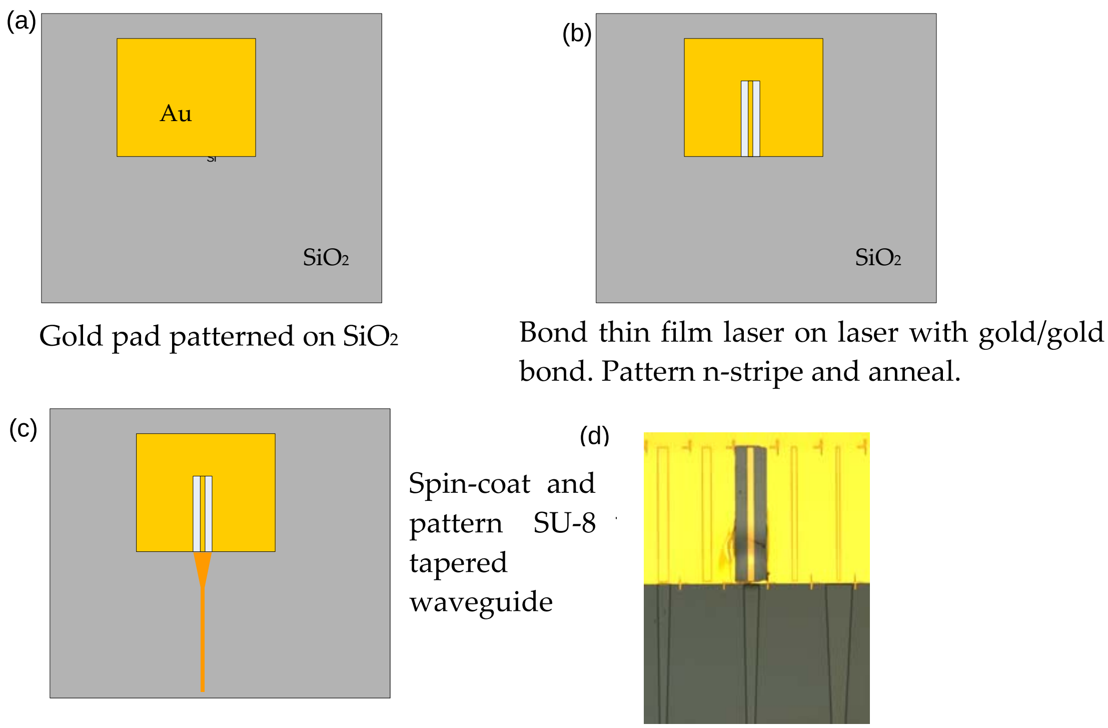

Figure 6-3. (a)-(c) Integration process for a thin film laser with a polymer waveguide on SiO_2/Si; (d) Photomicrograph of the fabricated integrated system.

The integrated system was driven using a current source (ILX Lightwave LDP 3811) with pulsed current (0.01% duty cycle) and a pulse width of 0.1 μs. Figure 6-4 shows infrared images (Sensors Unlimited SU-320MS-1.7RT-RS170 IR CCD Camera) of the laser. Figure 6-4 (a) is a top view of one end of the laser, with light emitting from the facet and reflecting off of the gold coated silicon pad due to the gap between the waveguide and the laser. Figure 6-4 (b) is the output from the waveguide from a side view.

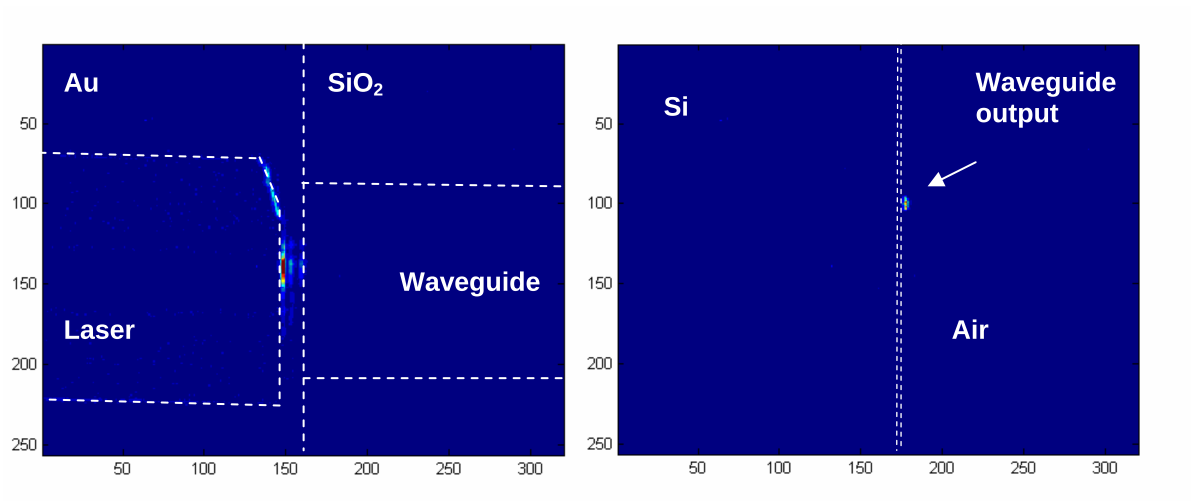

Figure 6-4. (a) Infrared image of light output from the laser. The direction of propagation is along the plane of the paper to the right. Note reflections from the surface of the gold pad on the silicon; (b) Light output from the output port of the cleaved end of the SU-8 waveguide. The direction of propagation is normal to the plane of the paper. In both images, the approximate location of components is shown by dashed lines.

The optical power at the output of the waveguide was collected with a multimode fiber connected to a HP 81521B optical head and a HP 8163A power meter to produce the L-I measurements shown in Figure 6-5. The threshold current density is ~250 A/cm^2. The spectrum, indicating lasing at a wavelength of 990 nm, was captured with an Ando AQ-6315E OSA with a resolution of 50 pm.

(a)

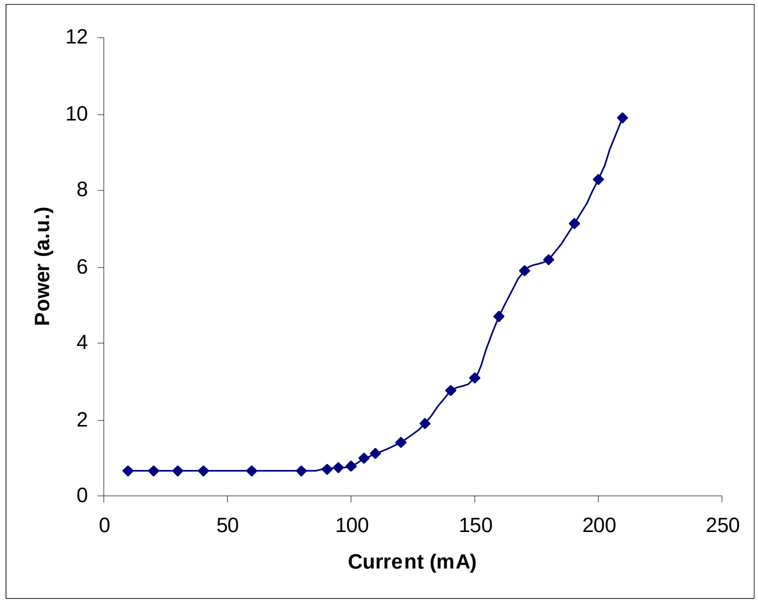

(b)

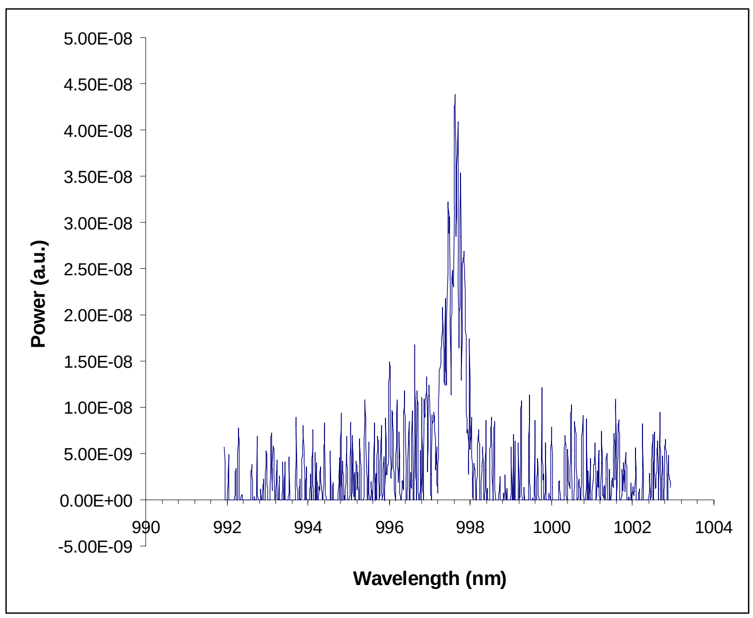

Figure 6-5. (a) Integrated laser/waveguide L-I characteristic as measured at the output of the waveguide. The injected threshold current density is ~250 A/cm^2; (b) The laser spectrum indicates lasing at λ=997 nm.

6.3 Thin Film lasers Embedded into Polymer Waveguides[2]

A critical issue that traditionally faces the coupling of edge coupling lasers and optical fibers and waveguides is the tight tolerance in the placement of the waveguide/fiber facet with respect to the laser facet. As discussed in Section 2.3, a major step toward manufacturable planar photonic integrated systems is to eliminate the separation between the laser and the waveguide, to create an alignment tolerant coupled structure, to and to enable the simultaneous alignment of many optical devices at the wafer scale, i.e. to enable mask-based "optical wiring". The elimination of the laser/waveguide gap removes the Fabry Perot reflections occurring in the air gap, and the precise positioning requirements associated with optical fibers or waveguides on another substrate. In addition, the beam divergence of the laser is also reduced to a value of θ=45.45° from 70.9° due to the higher refractive index of the polymer compared to air. However, the laser facet that is embedded in the waveguide has a reduced reflectivity due to the semiconductor/polymer interface (R=14.7% for the InGaAs/GaAs SQW-SCH lasers in this thesis) as opposed to a semiconductor/air interface (R=31.3% for the same laser.) In this section, it is shown experimentally that lasing is still achieved in spite of the reduced reflectivity, with only a 27.2% increase in threshold current density. It is important to note that this configuration is possible only when the components are

[2] Excerpts appear in: S. Palit, J. Kirch, L. Mawst, N. M. Jokerst, "Thin Film lasers Embedded in Passively Aligned SU8 Waveguides on SiO2/Si" in *CLEO*, OSA, CWP5, May 16-21, 2010, San Jose, CA. and
S. Palit, J. Kirch, M. Huang, L. Mawst, and N. M. Jokerst "Facet Embedded Thin Film III-V Edge Emitting Lasers Integrated with SU-8 Waveguides on Silicon" *Optics Letters*, 2010 (submitted).

integrated in a planar configuration with an on-chip thin film source and waveguide on the same substrate.

Lasers of cavity lengths 800 μm and 1000 μm were integrated on a 4 mm x 4 mm square metal pad on SiO_2/Si consisting of a Ti-30 nm/Pt-40 nm/Au-200 nm stack. The lasers have p-ridges that are 50 μm wide and 1.01 μm deep with 40 μm n-stripes. As shown in Figure 6-6 , the front facet of the laser is kept as close to the edge of the metal pad as possible, to avoid reflections from the metal. Better control over the placement of the laser is possible by the use of automated tool. After this SU-8-2002 is spun on the integrated laser to a thickness of 2.6 μm and patterned with standard I-line photolithography to form a tapered waveguide. The linear taper, part of which overlaps the laser, extends from 86 μm to 8 μm over 1.6 mm as in the previous case.

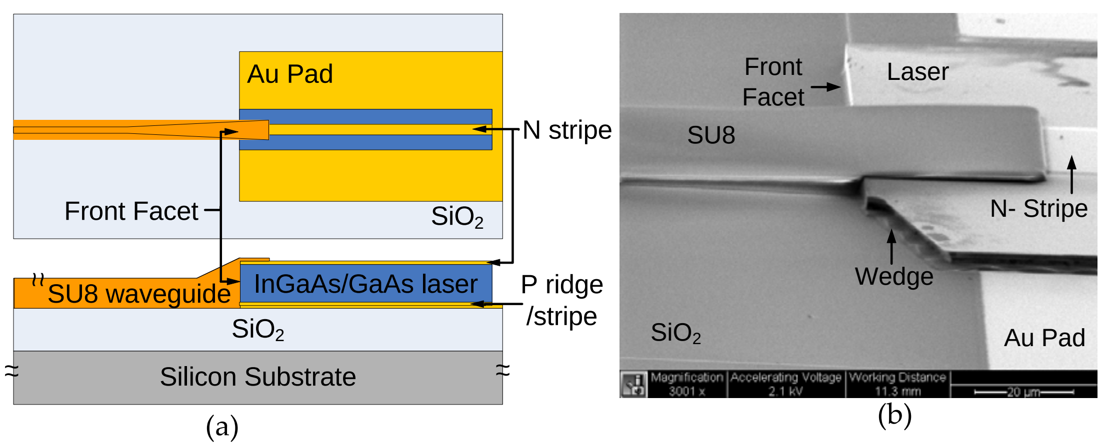

Figure 6-6. (a) Top view and side view illustration of edge emitting laser integrated with overlapping SU-8 waveguide; (b) SEM image of embedded laser facet and waveguide.

The measured power versus current characteristics of an 800 μm laser integrated with a tapered waveguide with separated and embedded configurations are shown in Figure 6-7 (a). A pulsed current of 0.01% duty cycle and a frequency of 1 KHz was used to drive the laser, and the light was collected from the endface of the waveguide (after cleaving off the very end to ensure a smooth surface for coupling) with a multimode fiber connected to an HP 8163A power meter with an HP 81521B optical head. For the case where the edge of the tapered waveguide was spaced away from the laser facet by 24 μm, the L-I characteristics indicated a threshold current of 110 mA corresponding to J_{th}= 275 A/cm^2. An overlapping waveguide was then patterned on top of this existing waveguide, leading to a threshold current of 140 mA (J_{th} = 350 A/cm^2). The change in threshold current by a factor of 27.2% is a result of the reduced reflectivity of the front facet due to the semiconductor-polymer interface. For some applications, such as portable applications where minimum power consumption is critical, the inherently low threshold current density of the laser makes this moderate increase in threshold current is acceptable given the coupling efficiency, reduced divergence and lack of Fresnel reflections due to the absence of an air gap. In addition, the requirement for tight tolerances in patterning the waveguide is also removed, first, by introducing a taper that allows some latitude in the lateral displacement between the laser and waveguide, and second, by eliminating the need to monitor the distance between the laser facet and waveguide facet by simply embedding the laser facet in the waveguide endface. The laser structure was simulated using Silvaco™, as described earlier herein.

(a)

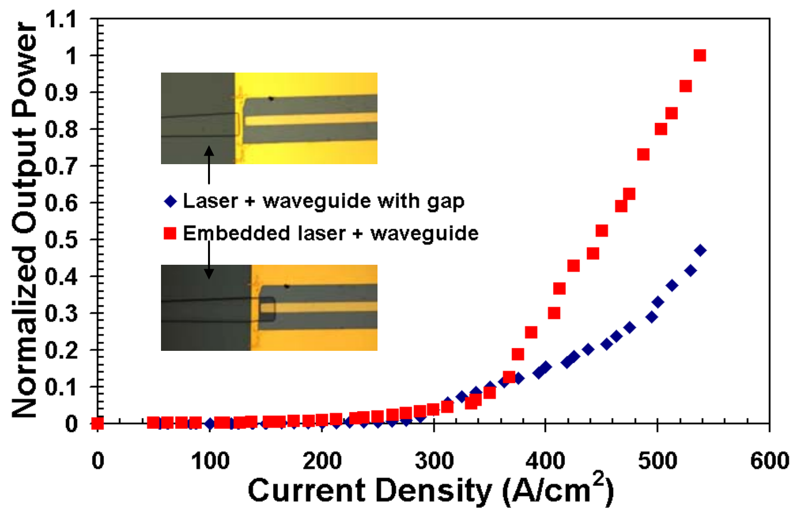

(b)

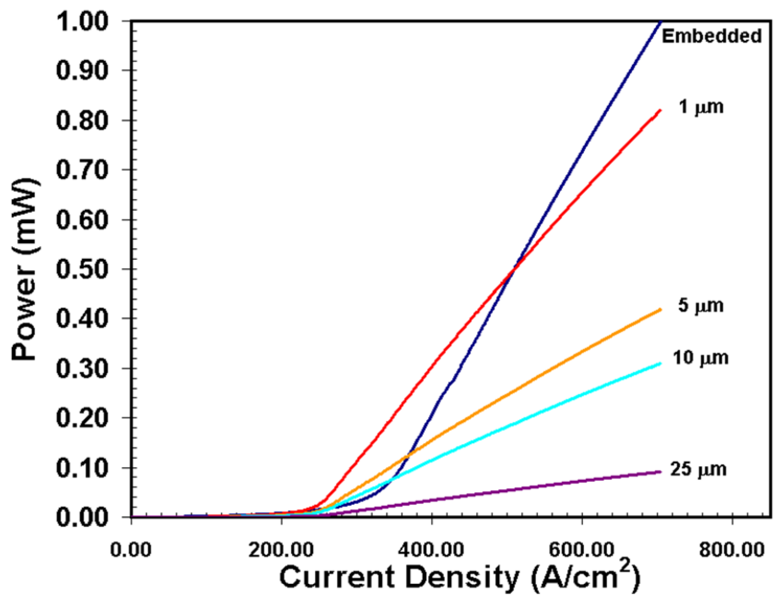

Figure 6-7.(a) Waveguide output power versus current from an 800 μm long laser integrated with SU-8 waveguide. The original integration (blue) with gap has lower threshold and lower waveguide output power. After embedding (red), the L-I has a higher threshold (27.2% more) and higher coupled power from the laser to the waveguide; (b) Simulated plots of waveguide power vs. current density for the embedded case and separated laser/waveguide case using Silvaco™ laser module and COMSOL. A 33% increase in J_{th} is predicted due to embedding the laser facet with SU-8

The front facet reflectivity was calculated to have changed from 31.3% to 4.7% due to the SU-8 interface, resulting in a 33% increase in threshold current density. The coupling of the laser output with the waveguide for different separations was simulated by 2D FEM simulations using COMSOL™, as described earlier herein. Figure 6-7 (b) shows the simulated waveguide power versus injected current density for the embedded waveguide, and for 1, 5, 10, and 25 μm laser/waveguide separations, and indicates a threshold current increase of 33% due to the embedded facet, compared to the experimentally observed change of 27.2%. Figure 6-8 shows the COMSOL simulation for the embedded case.

The single mode laser to waveguide coupling efficiencies based on the separations of the laser and waveguide, as calculated in COMSOL and used in the previous plot, are tabulated in Table 1. The coupling efficiency was calculated as a ratio of the power output in the waveguide 150 μm from the laser facet to the power output at the laser facet. The laser was treated as a passive device in the COMSOL simulation. This is justified because the near field profile in the vertical direction obtained from the Silvaco™ simulations is nearly-Gaussian and comparable to the simulated output from the facet of the laser calculated by COMSOL. The coupling efficiencies in the table are based on a constant laser power input for both the embedded and the separated cases. The coupling efficiency can be improved further by implementing a vertical taper in the waveguide, or also by reflow processes to form a micro lens at the waveguide facet.

Table 1. Single mode coupling efficiency as a function of separation between laser and waveguide.

Separation (μm)	Power Coupling Efficiency (%)
0	77.16
1	70.55
5	35.96
10	26.61
25	7.85

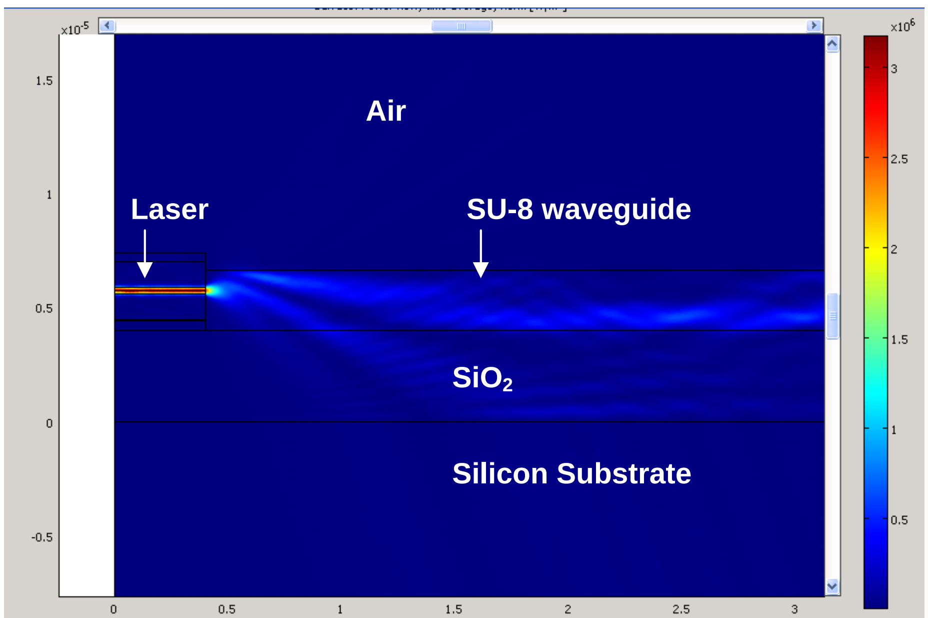

Figure 6-8. 2D COMSOL simulation illustrating propagation of laser light through Air/SU-8/SiO_2/Si waveguide, for the case where no air gap exists. Incorporation of a vertical taper as seen in the actual integrated system would further improve coupling.

As stated earlier, the laser simulations in Silvaco™ can also be performed for multiple longitudinal modes (set LMODES=1). However, solving for multiple transverse modes, while also obtaining spectral information, is computationally intensive. The two cases of simulations give very close values. Figure 6-9 (a) shows J_{th} for the case where only the fundamental transverse mode was calculated. In addition, the J_{th} for the reduced front facet reflectivity due to embedding into polymer (discussed in the next chapter) is also plotted. The shorter cavity length lasers exhibit the largest increase in J_{th} due to an embedded facet due to reduced facet reflectivity, because the loss per unit cavity length increases more for shorter lasers. Since the gain per unit cavity length is constant, this larger increase in loss per unit cavity length results in a larger increase in J_{th}. This is confirmed by the plot of the mirror loss factor (defined in Equation 3-3) as a function of cavity length, shown in Figure 6-9 (b).

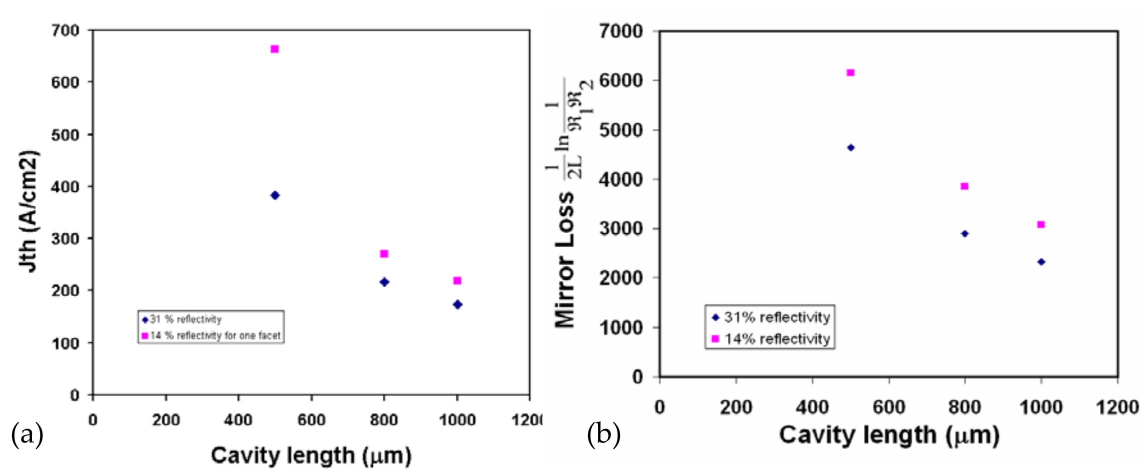

Figure 6-9. (a) Change of threshold current density with cavity length and mirror reflectivity; (b) Plot of mirror loss as a function of cavity length.

A 1000 μm long laser with a ridge 1.01μm deep and 50 μm wide ridge laser was also integrated with the facet extending over the metal pad to prevent reflection of the divergent laser light from the metal surface. The facet was embedded in the waveguide, as shown in Figure 6-10. Figure 6-11 shows infrared images for the same laser. No scattered light, unlike as in the case of Figure 6-4, is visible, thus extension of the laser facet beyond the bonding pad may reduce the reflected optical beam, potentially improving the coupling into the waveguide.

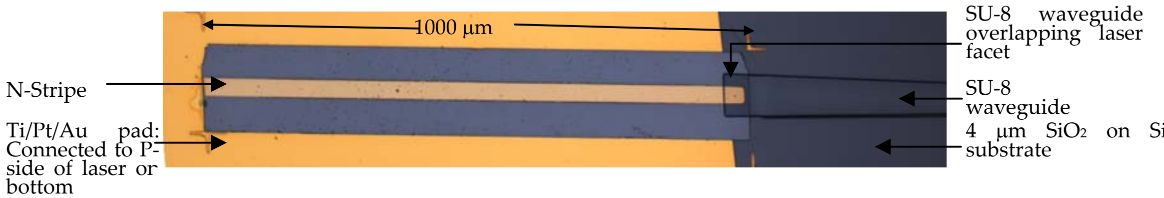

Figure 6-10. 1000 μm p-slotted ridge n-stripe laser with embedded laser facet.

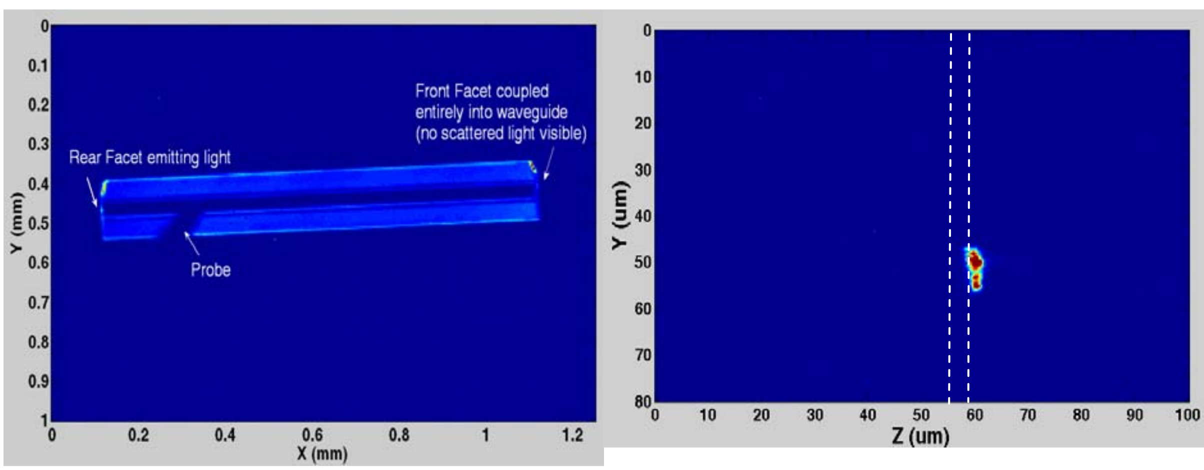

Figure 6-11. (a) Infrared image of 1000 μm embedded laser (top view). The direction of propagation is along the plane of the paper to the right; (b) Side view of light output from the output port of the SU-8 waveguide. The direction of propagation is normal to the plane of the paper.

The L-I characteristics of the laser are shown in Figure 6-12. The threshold current density was J_{th}=260 A/cm^2, and the multimode spectrum had a wavelength of 1002.15 nm for the strongest peak. The peak power of the spectrum for this particular integrated system was also much higher (though it is shown normalized in Figure 6-12). This may be attributed to the laser extending beyond the metal pad and the longer cavity length of the laser.

(a)

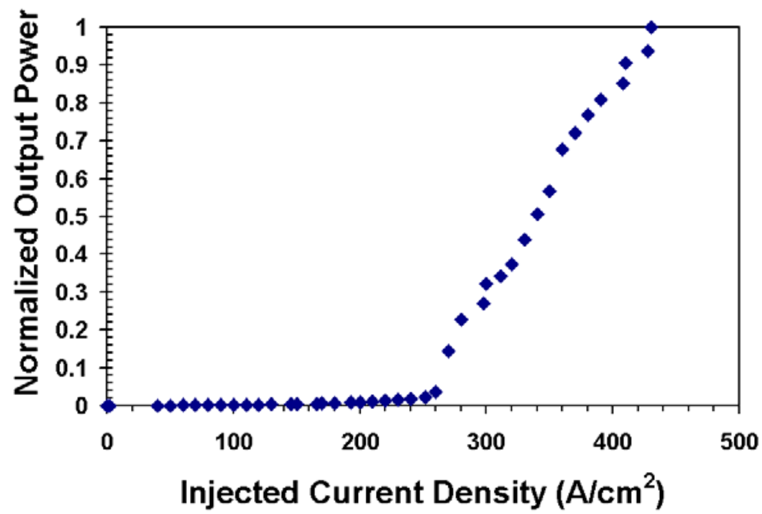

(b)

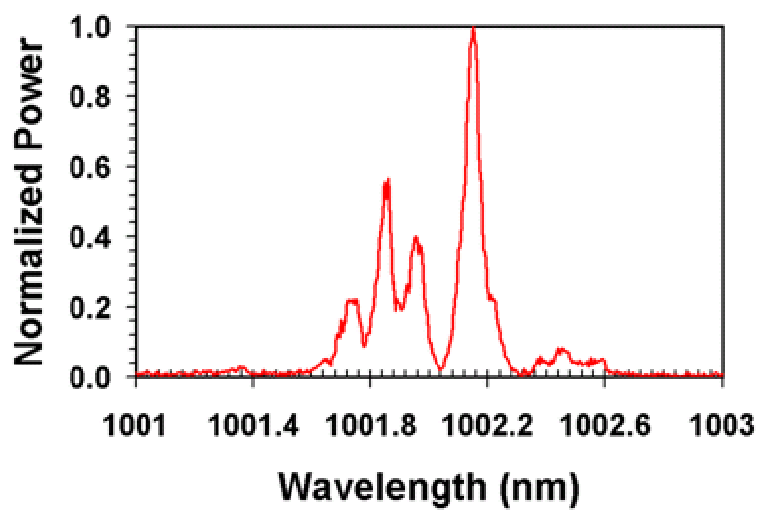

Figure 6-12. (a) Waveguide output power versus current for the 1000 μm laser, showing J_{th}=260 A/cm^2; (b) Laser output spectrum at a current of 210 mA (J=420 A/cm^2).

The previous two sets of results involved first patterning the waveguide with a gap between the laser facet and the waveguide facet, and then patterning the overlapping waveguide on top of the original waveguide. To obtain a more unambiguous result with a single embedded waveguide, and to eliminate substrate modes that can be detected when using a straight waveguide, another set of samples, and a final set of experiments for an 800 μm laser, with a ridge depth of 0.61 μm and width of 50 μm, with a passively aligned SU-8 polymer waveguide, was fabricated and tested. This tapered S-bend waveguide, tapered from 60 μm to 4 μm over 6.25 mm, consists of two 90° bends of 4 mm radii, as shown in the schematic in Figure 6-13. RSoft BeamPROP BPM simulations (similar to those shown in Figure 6-1) indicated that 89.27% of the incident power would get coupled from the laser to the waveguide through this taper. The radius of the S-bend was large enough (4 mm) that bending loss did was insignificant. Figure 6-14 shows an infrared image of the top view of the laser integrated with the waveguide. The dashed gray lines indicate the positions of the waveguide and the pad on the SiO_2/Si substrate. The J_{th} for this integrated structure is 357 A/cm^2, and the lasing wavelength is 995.27 nm, as shown in Figure 6-15.

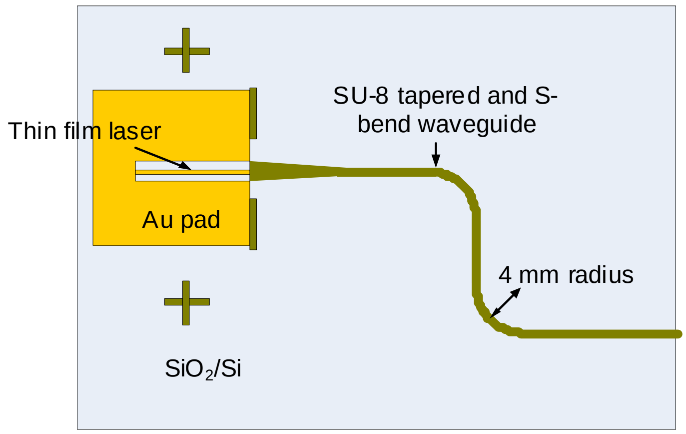

Figure 6-13. Schematic of thin film laser integrated with tapered and S-bend waveguide.

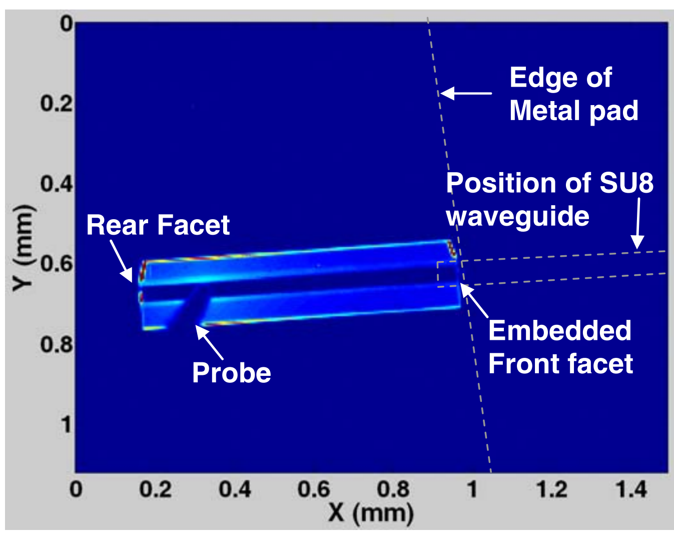

Figure 6-14. Infrared image of an 800 μm (40 μm p-metal stripe, p-ridge width of 50 μm and depth of 0.61 μm and n-metal stripe of 40 μm) laser with front facet embedded in SU-8 tapered S-bent waveguide of 4 μm width and 2.6 μm thickness.

(a)

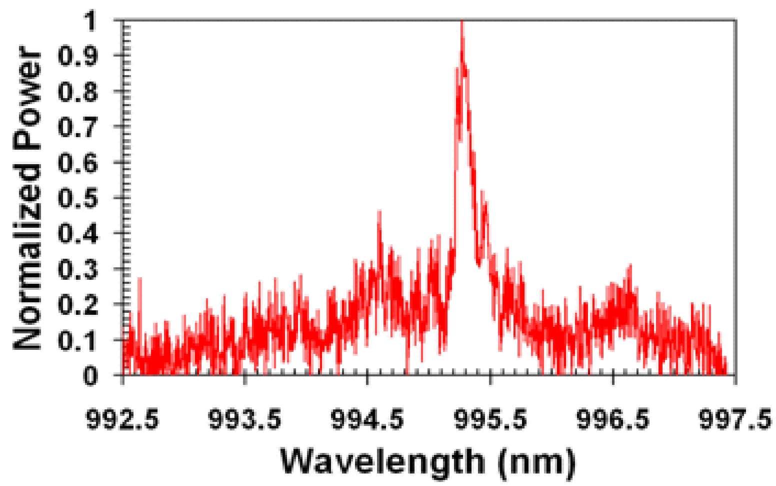

(b)

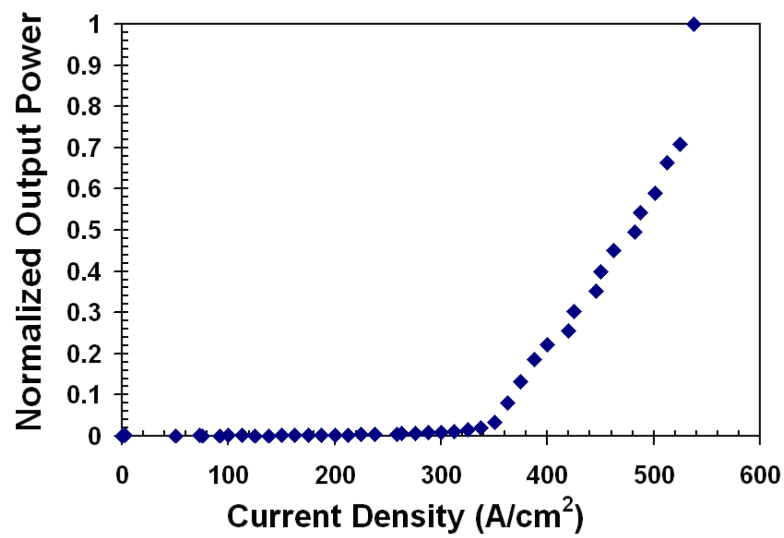

Figure 6-15. (a) L-I characteristics with J_{th} = 357 A/cm^2 and (b) spectrum for the system, with a peak wavelength of 995.27 nm.

From these experimental and theoretical results we see that greater coupling is possible as a result of embedding the front facet of the laser into the tapered polymer waveguide. At the same time, photolithography can be used to pattern the waveguide without trying to maintain strict horizontal and vertical tolerances between the laser and the waveguide as would have been the case for a laser and waveguide on two different substrates. Also, heat sinking could be implemented below the laser, by metal plated in through-Si vias, for example, without interfering with the waveguiding and light distribution functionality of the integrated system.

The embedding of high power laser facets in waveguides for high efficiency coupling may be an issue due to the thermally insulating polymer at the laser facet, which could accelerate catastrophical optical damage (COD). There is also some limit to the distance that the laser can be displaced laterally from the center of the waveguide, as this would lead to exciting only higher order modes in the waveguide. At present, the footprint of the integrated system is fairly large due to the long tapers and large bends. The taper width and length can be reduced for lasers with narrower ridges (single spatial mode). Recent characterization on bending losses in SU-8 waveguides indicates that much smaller bends can be made with minimal effect on the propagated power [118]. A high reflectivity (HR) on the back facet of the laser may further reduce the threshold current for these embedded lasers.

7 Conclusions

On-chip light sources may provide high efficiency sources for portable chip scale photonic sensing systems and optical interconnects. III-V edge emitting lasers integrated on silicon that are designed for low power consumptions and good thermal conduction, while also making it possible to integrate with other optical components with low coupling losses, can open up new avenues for potentially low cost, portable photonic integrated systems.

In this thesis, gain guided and index guided InGaAs/GaAs strain compensated SQW thin film edge emitting lasers, with metal contacts on both sides of the epitaxial layer, were integrated onto Si and SiO_2/Si host substrates. Processes were developed that enabled fabrication under either the support of the growth substrate or the host substrate, ensuring stability and repeatability. Injected threshold current densities of 242 A/cm^2, the lowest for integrated SQW thin film EELs on Si, and for thin film EELs operating at 980 nm wavelengths, were achieved. The index guided lasers implemented have a rectangular cross section, making it easier for planar integration with other optical components.

The ability to integrate diverse photonic components of similar vertical dimensions on the same planar substrate can be leveraged in ways not possible with discrete components. In this thesis, EELs were integrated with SU-8 waveguides on SiO_2/Si in an overlapping configuration that ensured better coupling while still maintaining relatively low threshold current densities for the laser (260 A/cm^2), and removing the requirement for tight tolerances between the laser and the waveguide.

Based on the results in this thesis, it is possible to design thin film edge emitting lasers in ways that are comparable to bulk lasers, and integrate them in a manner that does not necessarily compromise their performance characteristics. In addition, it is also shown that system level strategies for coupling with other components need not be compromised on as well, and in fact, as demonstrated in the latter case, can be implemented on a common Si platform.

8 Future Work

There are many aspects of this thesis that merit deeper exploration. These span electrical characterization, thermal characteristics, and CW operation. In addition, these integrated lasers and waveguides are also a starting point for larger and more complex integrated photonic systems.

As seen from the experimental results, the I-V characteristics indicated poor electrical contacts. This requires further optimization of the metal contacts to reduce the contact resistance. There are three aspects to this. One is that these lasers are being probed directly without packaging. As a result, very high local current densities are generated at the contact point of the probe and metal. Very narrow stripes cannot be probed due to the high sheet resistance, although this effect is mitigated to some extent due to the high conductivity of the n-cap layers, which eventually needs to be etched away outside the stripe for better current confinement. Second, the ohmic contacts to the capping layers need to be characterized (for example through 4-point transmission line measurements), and the high temperature annealing conditions need to be optimized to realize lower contact resistance. Third, the interface between the metallized p-side and the Si or SiO_2/Si needs to be made more robust. At present this is an annealed contact bond with no pressure applied. Thermocompression bonding would be a good direction to take for this interface. Thus, both packaging and process optimization can help to produce better electrical laser characteristics.

Addressing the above mentioned issues would also aid towards CW operation, by enabling low thermal resistance metal paths for drawing away heat from the laser. From the perspective of system integration, electroplated through-Si vias below the laser would also enable CW operation, and would reduce the power requirements for an active cooling (thermoelectric cooling) system.

Investigation of the causes for the low slope efficiency for the p-ridge n-broad area lasers, and measurement of absolute power and slope efficiency of the p-slotted ridge, n-stripe lasers are also required. Reasons for low T_0 include Auger and intervalence band absorption, both of which increase at higher lasing currents [90]. In addition, free carrier absorption and carrier leakage are also known culprits for low T_0 , although all of these have lower values for these material systems at shorter wavelengths [90, 119]. The impact of the handling technique for the laser also needs to be investigated further. If the lasers get stressed during handling and cleaving, then micro defects would be generated throughout the laser, becoming points for traps and hot spots, affecting the thermal behavior of the laser [120]. While the material structure was designed for net zero strain, some residual strain may still have been present in practice. Very slight bowing of the thin film lasers in the case of the gain guided and the p-ridge broad area lasers was seen. The residual strain may have different values in the lasers in this thesis due to the different amounts of strain relaxation due to processing the lasers differently (for example, ridge versus slotted ridge). All of these would have an impact on the thermal characteristics.

Another question that has often come up is the issue of scalability of the transfer process. In this thesis, it led to the investigation of using heat release material for the process, as this can help with both individual device bonding and scalability. One option is spot heating of areas on the sheet using a laser beam. For this, the beam spot size and energy needs to be characterized. This can be used to bond specific devices from an array in an automated manner. A heated substrate can be used for transfer of multiple devices. Heat release and UV release materials are designed for handling thinned bulk components (50-100 μm thick), so the adhesion may prove too strong for the thin film lasers. Thus, research into organic materials to explore low adhesion thermal release sheets designed especially for very thin film devices would be ideal.

There are many opportunities for looking at different laser materials as well. This thesis worked with a 980 nm strain compensated SQW laser. Strain compensated multiple quantum well lasers are challenging from a design perspective, although certainly more advantageous due to the larger gain per volume. Laser materials grown on metamorphic buffer layers could have interesting points of comparison with and without their growth substrates, due to the change in residual strain in the active region [121-123].

The whole concept of planar on-chip lasers comes from the need for chip scale integration with other optical components to enable low power, portable systems. A next step would be integration of the laser and tapered waveguide system with an optical sensing element, for example, a plasmonic waveguide or a microring resonator. Compressively strained quantum wells, such as in this thesis, primarily emit TE polarized light, while plasmonic waveguides need TM excitation, so strategies for incorporating either lasers with tensile strained wells [124], or active/passive mode converters need to be explored [125-129]. For resonance based devices, such as micro ring/disk resonators, the stability of the laser peak wavelength, with no mode hopping, is very important. In this respect, distributed bragg resonator lasers, that have a single narrow linewidth longitudinal mode, could also be investigated to ensure sensitivity in detection.

Appendix A. Fabrication Processes

A.1: Top And Bottom Stripe, Broad Area Bonded Laser

1 Photomask:

1.1 For 500 μm cavity lengths and multiple width p stripes within single reticle: Microtronics Inc, LD_Jan_2008_f8R14 #295

1.2 800, 1000 and 1200 μm cavity lengths and same width p stripes within single reticle: Microtronics Inc. "Thin Film P Ridge N Ridge BA Metal Laser" 12/22/2008 #1664

2 Sample Preparation

2.1 Cleave a scrap piece of silicon to 2 cm x 2 cm piece. Place a 4 mmx4mm piece of double sided Kapton tape on it, offset to one corner.

2.2 Material id: 5903. Cleave a 4 mm x 4 mm square piece. Check back lapped side for direction of oval grains. The laser bars are to be patterned perpendicular to (long axis) the grains.

2.3 Place on kapton tape, and mark laser orientation on the Si.

2.4 Clean sample with TCE, Acetone and Methanol for 20 s each.

2.5 Dry with N_2.

3 P stripe : Negative photolithography , metallization and liftoff

3.1 Spin coat photoresist AZ5214-E with following parameters:

Step	Speed (rpm)	Ramp(rpm/s)	Time(s)
Step 1	1000	1000	5
Step 2	4000	1000	45
Step 3	0	1000	5

3.2 Prebake on Hot plate: 40s@100 °C.

3.3 Suss Microtec MJB3 Mask Aligner, 365 nm, Constant Intensity Control, 9.2mw/cm^2. Run two 5s dummy exposures to stabilize the power.

3.4 Align p stripe mask pattern with sample. Soft contact.
Expose for 3 sec (27.6 mJ)

3.5 Postbake on Hot plate: 30s@100 °C.

3.6 Flood Exposure: 45 s (360-400mJ)

3.7 Develop
354 Developer, 9 s
Rinse in DI water.
N2 dry.

3.8 Electron Beam Evaporation:

Metal	Thickness (Å)	Deposition Rate (Å/s)
Ti	150 Å	2
Pt	150 Å	1
Au	1000 Å	10

3.9 Immerse in covered petri dish with acetone, for liftoff. Allow to soak such that kapton loses adhesion, and you can slide the sample off the kapton and the Si carrier

4 Oxide Isolation: SiO_2 deposition, Positive photolithography, Etch

4.1 PECVD SiO_2 1300 Å. Advanced Vacuum Vision 310. Place sample on chuck with dummy pieces of same thickness flush against all four sides of the sample.

Chuck Temperature	250 °C
Pressure	800 mT
RF setpoint	20 W
3 % SiH_4	400 sccm
N_2O	1420 sccm
Time	3 min. 42 s

4.2 Heat glass microscope cover slip on hotplate at 125 °C, and bond sample with Apiezon W (black wax) on it, offset to one corner.

4.3 Spin coat photoresist AZ5214-E with following parameters:

Step	Speed (rpm)	Ramp(rpm/s)	Time(s)
Step 1	1000	1000	5
Step 2	3500	1000	45
Step 3	0	1000	5

4.4 Prebake on hot plate: 1min@100 °C.

4.5 Suss Microtec MJB3 Mask Aligner, 365 nm, Constant Intensity Control, 9.2mw/cm^2. Run two 5s dummy exposures to stabilize the power.

4.6 Align oxide etch mask pattern with sample. Soft contact.
Expose for 4.89 sec (45 mJ)

4.7 Develop
354 Developer, 15 -18 s
Rinse in DI water.
N2 dry.

4.8 Hard bake on hot plate: 4min@125°C.

4.9 Check height of SiO_2 with Dektak

4.10 BOE etch: 2 min (check with Dektak to ensure the height stabilizes). ~1300 Å etch expected

4.11 Dissolve away photoresist in acetone

4.12 Check height of SiO2 with Dektak

5 Broad Area Metal: Negative Photolithography, Metallization, Liftoff

5.1 Spin coat photoresist AZ5214-E with following parameters:

Step	Speed (rpm)	Ramp(rpm/s)	Time(s)
Step 1	1000	1000	5
Step 2	4000	1000	45
Step 3	0	1000	5

5.2 Prebake on Hot plate: 40s@100 °C.

5.3 Suss Microtec MJB3 Mask Aligner, 365 nm, Constant Intensity Control, 9.2mw/cm^2. Run two 5s dummy exposures to stabilize the power.

5.4 Align broad area metal pattern on mask (square notches) with sample. Soft contact.
Expose for 3 sec (27.6 mJ)

5.5 Postbake on Hot plate: 30s@100 °C.

5.6 Flood Exposure: 45 s

5.7 Develop
354 Developer, 9 s
Rinse in DI water.
N2 dry.

5.8 Electron Beam Evaporation:

Metal	Thickness (Å)	Deposition Rate (Å/s)
Ti	200 Å	2
Pt	300 Å	1
Au	1800 Å	10

5.9 Immerse in acetone for liftoff.

6 Mesa: Positive photolithography, Wet Etch

6.1 Spin coat photoresist AZ5214-E with following parameters:

Step	Speed (rpm)	Ramp(rpm/s)	Time(s)
Step 1	1000	1000	5
Step 2	3500	1000	45
Step 3	0	1000	5

6.2 Prebake on hot plate: 1 min @ 100 °C.

6.3 Suss Microtec MJB3 Mask Aligner, 365 nm, Constant Intensity Control, 9.2mw/cm^2. Run two 5s dummy exposures to stabilize the power.

6.4 Align mesa etch pattern (v - grooves) on mask with sample. Soft contact.
Expose for 4.89 sec (45 mJ)

6.5 Develop
354 Developer, 15 s
Rinse in DI water.
N2 dry.

6.6 Hard bake on hot plate: 3 min 40 s @ 125°C.

6.7 Check height with Dektak

6.8 BOE: 2 min: This cleans the oxide within the wedges.

6.9 Verify that all the oxide has disappeared from the wedges.

6.10 HCl:H20::1:1: 30s, DI Rinse and N2 blow dry.

6.11 H_2SO_4:H_2O_2:H_2O_2::1:8:200: This is a non selective etch, and we want to control how much it etches into the 1.5 μm thick n^+ GaAs contact. Ideally, we want <0.4 μm of the n^+ GaAs contact.

15 m 30 s- 17 m to get a total etch of about ~3.45 μm with the photoresist mask. In this time frame ~0.4 μm of the photoresist also gets etched. So final height after photoresist removal is 3.85 μm.

6.12 Remove photo resist in Acetone.

7 Encapsulation with Apiezon W

7.1 Hotplate 135 °C. Place sample that is still attached to the cover slip on hotplate. Remove sample from cover slip.

7.2 Place sample in covered petri dish filled with TCE to clean off the black wax from the back. Handle tweezers with care to prevent scratching the sample.

7.3 Dunk sample in acetone and methanol and N2 blow dry.

7.4 Place a clean glass cover slip on a flat surface and place the sample on top of it

7.5 Using pointed tweezers, place a small piece of black wax on top of the sample. It should Not extend beyond the edges of the sample.

7.6 Slowly lift the cover slip with sample and wax on top of it and place on hotplate at 135 °C. Also place a piece of Teflon on the hotplate.

7.7 Allow black wax to melt till it forms a dome. Remove the coverslip with the sample on it and place it on a flat surface. Then take the heated piece of Teflon and touch its plane to the top of the dome. Do not press down. The black wax should stick to the Teflon and the sample can be lifted up.

8 Epitaxial Liftoff

8.1 Place Teflon carrier with sample flat at the bottom of the beaker.

8.2 HF:H2O::1:10. ~20 hours (selective etch for AlxGa1-xA where x>0.4)

8.3 Remove sample from beaker holding the Teflon carrier. The substrate will slide off to reveal the back n++ GaAs layer.

8.4 $C_6H_8O_7$: H2O2::4: 1 (Citric acid and hydrogen peroxide) : >4min or till the black wax can be seen between the laser bars.

9 Transfer to Transfer diaphragm

9.1 Nudge the interface between the black wax and Teflon with a razor blade till the black wax containing the laser bars pops off.

9.2 Place face down on transfer diaphragm with a drop of water. Place diaphragm in a wafer case.
9.3 Leave in a stationary location for 2 days. Do not place in desiccators.
9.4 Place transfer diaphragm in petri dish and slowly add TCE with a pipette.
9.5 As the Apiezon W starts dissolving remove the solution with a pipette till the samples on the diaphragm look clean.

10 Cleaving and transfer of lasers

10.1 Using a smooth round surface, (like the end of a diamond scriber cover) to flex the diaphragm.
10.2 This will cause cleaves to be generated along the grooves.
10.3 Under a microscope, use a second transfer diaphragm with a drop of water to pick up individual lasers and transfer them to a metallized SiO_2/Si substrate.
10.4 Heat on a hotplate for 10 min @ 180 °C.

11 N-stripe: Negative Photolithography, Metallization and Liftoff.

11.1 Spin coat Futurrex NR9-3000 PY with following parameters:

Step	Speed (rpm)	Ramp(rpm/s)	Time(s)
Step 1	500	500	5
Step 2	1600	1600	45
Step 3	0	1000	5

11.2 Prebake on hot plate: 1 min @ 150 °C.
11.3 Suss Microtec MJB3 Mask Aligner, 365 nm, Constant Intensity Control, 9.2mw/cm^2. Run two 5s dummy exposures to stabilize the power.
11.4 Align n-stripe of desired width and correct cavity length on mask with sample. Soft contact.
Expose for 35.89 sec (330 mJ)
11.5 Postbake on hot plate: 1 min @ 100 °C.
11.6 Develop
RD6 Developer, 14 s
Rinse in DI water.
N2 dry.
11.7 De-scum in Asher:
O2 flow to give 6x10-1 mbar
45 sec @ 50 W
11.8 BOE: 1 min
11.9 HCl:H2O::1:1 : 30 sec, place in N2, till ready to metallized.

11.10 Metallization

Metal	Thickness (Å)	Deposition Rate (Å/s)
Thermal Evaporation		
AuGe(88%:22%) Alloy	800 Å	1
Electron Beam Evaporation		
Ni	200 Å	1
Au	1000 Å	5

11.11 Place in covered petri dish with acetone for liftoff. Usually takes a while due to the thick resist. Best left overnight.

11.12 RTA on hotplate: 10 s @ 365 °C (Clean room RTA equipment temperature overshoot compromises n-stripe surface)

A.2: Top p-Ridge, Bottom n-Broad Area Laser

1 Photomask

1.1 For longer cavity lengths (SQW lasers): Thin Film LD, Sang Yeon Cho, Run # L00046, Serial #29985

1.2 For short cavity lengths (MQW lasers): Adtek Job # 243100, Georgia Tech, 13 Jan 04

2 Sample Preparation

1.1 Material id: 5903. Cleave a 4 mm x 4 mm square piece. Check back lapped side for direction of oval grains. The laser bars are to be patterned perpendicular to (long axis) the grains

1.2 Hot plate at 125 °C

1.3 Place a glass cover slip on the hotplate and bond the sample on one corner of cover slip with Apiezon W.

1.4 Clean with TCE, Acetone, Methanol, 20 s each

1.5 N2 blow dry.

2 P stripe : Negative photolithography , metallization and liftoff

2.1 Spin coat photoresist AZ5214-E with following parameters:

Step	Speed (rpm)	Ramp(rpm/s)	Time(s)
Step 1	1000	1000	5
Step 2	4000	1000	45
Step 3	0	1000	5

2.2 Prebake on Hot plate: 40s@100 °C.

2.3 Suss Microtec MJB3 Mask Aligner, 365 nm, Constant Intensity Control, 9.2mw/cm^2. Run two 5s dummy exposures to stabilize the power.

2.4 Align p stripe reticle on mask with sample. Soft contact.

Expose for 3 sec (27.6 mJ)

2.5 Postbake on Hot plate: 30s@100 °C.

2.6 Flood Exposure: 45 s (360-400mJ)

2.7 Develop

354 Developer, 9 s

Rinse in DI water.

N2 dry.

2.8 Electron Beam Evaporation:

Metal	Thickness (Å)	Deposition Rate (Å/s)
Ti	150 Å	2
Pt	150 Å	1
Au	1000 Å	10

2.9 Immerse in covered petri dish with acetone, for liftoff. Allow to soak such that kapton loses adhesion, and you can slide the sample off the kapton and the Si carrier

3 Ridge: Wet Etch

3.1 HCl:H20::1:1: 30s

3.2 DI Rinse and N2 blow dry.

3.3 Metal P stripe used as etch mask. Measure thickness with Dektak

3.4 H_2SO_4:H_2O_2:H_2O_2::1:8:200 : 5 min. Etch depth ~1 μm

4 Mesa: Positive photolithography, Wet Etch

4.1 Spin coat photoresist AZ5214-E with following parameters:

Step	Speed (rpm)	Ramp(rpm/s)	Time(s)
Step 1	1000	1000	5
Step 2	3500	1000	45
Step 3	0	1000	5

4.2 Prebake on hot plate: 1 min @ 100 °C.

4.3 Suss Microtec MJB3 Mask Aligner, 365 nm, Constant Intensity Control, 9.2mw/cm^2. Run two 5s dummy exposures to stabilize the power.

4.4 Align mesa etch pattern (V- grooves) on mask with sample. Soft contact.

Expose for 4.89 sec (45 mJ)

4.5 Develop

354 Developer, 15 s

Rinse in DI water.

N2 dry.

4.6 Hard bake on hot plate: 3 min 40 s @ 125°C.

4.7 Measure height with Dektak

4.8 HCl:H20::1:1: 30s

4.9 DI Rinse and N2 blow dry.

4.10 H_2SO_4:H_2O_2:H_2O_2::1:8:200 : This is a non selective etch, and we want to control how much it etches into the 1.5 μm thick n^+ GaAs contact. Ideally, we want <0.4 μm of the n^+ GaAs contact.
15 m 30 s to 17 m to get a total etch of about ~3.45 μm with the photoresist mask. In this time frame ~0.4 μm of the photoresist also gets etched. So final height after photoresist removal is 3.85 μm.

4.11 Remove photoresist in acetone.

5 Encapsulation with Apiezon W

5.1 Hotplate 135 °C. Place sample that is still attached to the cover slip on hotplate. Remove sample from cover slip.

5.2 Place sample in covered petri dish filled with TCE to clean off the black wax from the back. Handle tweezers with care to prevent scratching the sample.

5.3 Dunk sample in acetone and methanol and N2 blow dry.

5.4 Place a clean glass cover slip on a flat surface and place the sample on top of it

5.5 Using pointed tweezers, place a small piece of black wax on top of the sample. It should not extend beyond the edges of the sample.

5.6 Slowly lift the cover slip with sample and wax on top of it and place on hotplate at 135 °C. Also place a piece of Teflon on the hotplate

5.7 Allow black wax to melt till it forms a dome. Remove the coverslip with the sample on it and place it on a flat surface. Then take the heated piece of Teflon and touch its plane to the top of the dome. Do not press down. The black wax should stick to the Teflon and the sample can be lifted up

6 Epitaxial Liftoff

6.1 Place Teflon carrier with sample flat at the bottom of the beaker.

6.2 HF:H2O::1:10. ~20 hours (selective etch for AlxGa1-xA where x>0.4)

6.3 Remove sample from beaker holding the Teflon carrier. The substrate will slide off to reveal the back n++ GaAs layer.

6.4 $C_6H_8O_7$: H2O2::4: 1 (Citric acid and hydrogen peroxide) : >4min or till the black wax can be seen between the laser bars.

7 N Broad Area

7.1 Electron Beam Evaporation

Metal	Thickness (Å)	Deposition Rate (Å/s)
Au	150 Å	2
Ge	150 Å	1
Ni	200 Å	1
Au	1000 Å	10

Note: The thermal evaporator cannot be used for depositing AuGe alloy in this case, as the higher temperature causes the Apiezon W to soften and melt.

8 Transfer to Transfer diaphragm

8.1 Nudge the interface between the black wax and Teflon with a razor blade till the black wax containing the laser bars pops off.

8.2 Place face down on transfer diaphragm with a drop of water. Place diaphragm in a wafer case.

8.3 Leave in a stationary location for 2 days. Do not place in desiccators.

8.4 Place transfer diaphragm in petri dish and slowly add TCE with a pipette.

8.5 As the Apiezon W starts dissolving remove the solution with a pipette till the samples on the diaphragm look clean.

9 Cleaving and transfer of lasers

9.1 Using a smooth round surface, (like the end of a diamond scriber cover) to flex the diaphragm.

9.2 This will cause cleaves to be generated along the grooves.

9.3 Under a microscope, use a second transfer diaphragm with a drop of water to pick up individual lasers and transfer them to a metallized (Ti 200 Å/Pt 300 Å/Au 2000A) SiO_2/Si substrate.

9.4 Heat on a hotplate for 10 min @ 180 °C.

A.3: p-Slotted Ridge, n-Stripe, Broad Area Laser

1 Photomask

1.1 For 500 μm cavity lengths and multiple width p stripes within single reticle: Microtronics Inc, LD_Jan_2008_f8R14 #295

1.2 800, 1000 and 1200 μm cavity lengths and same width p stripes within single reticle, Microtronics Inc. "Thin Film P Ridge N Ridge BA Metal Laser" 12/22/2008 #1664

2 Sample Preparation

1.1 Cleave a scrap piece of silicon to 2 cm x 2 cm piece. Place a 4 mmx4mm piece of double sided Kapton tape on it, offset to one corner.

1.2 Material id: 6752. Cleave a 4 mm x 4 mm square piece. Check back lapped side for direction of oval grains. The laser bars are to be patterned perpendicular to (long axis) the grains.

1.3 Place on kapton tape, and mark laser orientation on the Si.

1.4 Clean sample with TCE, Acetone and Methanol for 20 s each.

1.5 Dry with N_2.

2 P stripe : Negative photolithography , metallization and liftoff

2.1 Spin coat photoresist AZ5214-E with following parameters:

Step	Speed (rpm)	Ramp(rpm/s)	Time(s)
Step 1	1000	1000	5
Step 2	4000	1000	45
Step 3	0	1000	5

2.2 Prebake on Hot plate: 40s@100 °C.

2.3 Suss Microtec MJB3 Mask Aligner, 365 nm, Constant Intensity Control, 9.2mw/cm^2. Run two 5s dummy exposures to stabilize the power.

2.4 Align p stripe pattern on mask with sample. Soft contact.
Expose for 3 sec (27.6 mJ)

2.5 Postbake on Hot plate: 30s@100 °C.

2.6 Flood Exposure: 45 s (360-400mJ)

2.7 Develop
354 Developer, 9 s
Rinse in DI water.
N2 dry.

2.8 De-scum in Asher:
O2 flow to give 6x10-1 mbar
45 sec @ 50 W

2.9 Electron Beam Evaporation:

Metal	Thickness (Å)	Deposition Rate (Å/s)
Ti	150	2
Pt	150	1
Au	1000	10
Pt	150	1

2.10 Immerse in covered petri dish with acetone, for liftoff. Allow to soak such that kapton loses adhesion, and you can slide the sample off the kapton and the Si carrier.

3 Slotted Ridge

3.1 Spin coat photoresist AZ5214-E with following parameters:

Step	Speed (rpm)	Ramp(rpm/s)	Time(s)
Step 1	1000	1000	5
Step 2	3500	1000	45
Step 3	0	1000	5

3.2 Prebake on Hot plate: 40s@100 °C.

3.3 Suss Microtec MJB3 Mask Aligner, 365 nm, Constant Intensity Control, 9.2mw/cm^2. Run two 5s dummy exposures to stabilize the power.

3.4 Align slotted ridge pattern reticle on mask with sample. Soft contact.
Expose for 3 sec (27.6 mJ)

3.5 Postbake on Hot plate: 30s@100 °C.

3.6 Flood Exposure: 45 s (360-400mJ)

3.7 Develop
354 Developer, 9 s
Rinse in DI water.
N2 dry.

3.8 Hard bake 30 m @ 125 °C

3.9 Measure thickness with Dektak. The alignment marks outside the laser array can be used for this purpose, as the slots are too narrow for the Dektak tip.

3.10 HCl:H20:: 1:1: 30 sec

3.11 DI water rinse

3.12 Blow dry aggressively with N2 for 1 min. This is important; as any water residue will call non uniformity in RIE etch.

3.13 Reactive Ion Etch: Etch depth of ~ 0.98-1 μm
First do 2 dummy runs of 60 s each with the following parameters and then put in sample. Manual process control.

Parameter	Value
RIE	75 W
ICP	200 W
Pressure	5 mT
BCl_3	8
Cl_2	2
Time	17 s

3.14 Verify thickness with Dektak

3.15 Remove photo resist with acetone, with sonication at 4000 rpm for 10 s. Verify cleanliness of surface under microscope

4 Oxide Isolation: SiO_2 deposition, Positive photolithography, Etch

4.1 PECVD SiO_2 1450 Å. Advanced Vacuum Vision 310. Place sample on chuck with dummy pieces of same thickness flush against all four sides of the sample.

Chuck Temperature	250 °C
Pressure	800 mT
RF set point	20 W
3 % SiH4	400 sccm
N2O	1420 sccm
Time	4 min. 41 s

4.2 Heat glass microscope cover slip on hotplate at 125 °C, and bond sample with Apiezon W (black wax) on it, offset to one corner.

4.3 Spin coat photoresist AZ5214-E with following parameters:

Step	Speed (rpm)	Ramp(rpm/s)	Time(s)
Step 1	1000	1000	5
Step 2	3500	1000	45
Step 3	0	1000	5

4.4 Prebake on hot plate: 1min@100 °C.

4.5 Suss Microtec MJB3 Mask Aligner, 365 nm, Constant Intensity Control, 9.2mw/cm². Run two 5s dummy exposures to stabilize the power.

4.6 Align oxide etch pattern on mask with sample. Soft contact.
Expose for 4.89 sec (45 mJ)

4.7 Develop
354 Developer, 15 -18 s
Rinse in DI water.
N2 dry.

4.8 Hard bake on hot plate: 4min@125°C.

4.9 Check height of SiO_2 with Dektak

4.10 BOE etch: 2 min (check with Dektak to ensure the height stabilizes). ~1300 Å etch expected

4.11 Dissolve away photoresist in acetone

4.12 Check height of SiO2 with Dektak

5 Broad Area Metal: Negative Photolithography, Metallization, Liftoff

5.1 Spin coat photoresist AZ5214-E with following parameters:

Step	Speed (rpm)	Ramp(rpm/s)	Time(s)
Step 1	1000	1000	5
Step 2	4000	1000	45
Step 3	0	1000	5

5.2 Prebake on Hot plate: 40s@100 °C.

5.3 Suss Microtec MJB3 Mask Aligner, 365 nm, Constant Intensity Control, 9.2mw/cm². Run two 5s dummy exposures to stabilize the power.

5.4 Align broad area metal pattern on mask with sample. Soft contact.
Expose for 3 sec (27.6 mJ)

5.5 Postbake on Hot plate: 30s@100 °C.

5.6 Flood Exposure: 45 s

5.7 Develop
354 Developer, 9 s
Rinse in DI water.

N2 dry.

5.8 Electron Beam Evaporation:

Metal	Thickness (Å)	Deposition Rate (Å/s)
Ti	200 Å	2
Pt	200 Å	1
Au	2000 Å	10

5.9 Immerse in acetone for liftoff.

6 Mesa: Positive photolithography, Wet Etch

6.1 Spin coat photoresist AZ5214-E with following parameters:

Step	Speed (rpm)	Ramp(rpm/s)	Time(s)
Step 1	1000	1000	5
Step 2	3500	1000	45
Step 3	0	1000	5

6.2 Prebake on hot plate: 1 min @ 100 °C.

6.3 Suss Microtec MJB3 Mask Aligner, 365 nm, Constant Intensity Control, 9.2mw/cm^2. Run two 5s dummy exposures to stabilize the power.

6.4 Align mesa etch pattern on mask with sample. Soft contact.
Expose for 4.89 sec (45 mJ)

6.5 Develop
354 Developer, 15 s
Rinse in DI water.
N2 dry.

6.6 Hard bake on hot plate: 5 min @ 125°C.

6.7 Check height with Dektak

6.8 BOE: 2 min: This cleans the oxide within the wedges.
Verify that all the oxide has disappeared from the wedges.

6.9 HCl:H20::1:1: 30s, DI Rinse and N2 blow dry.

6.10 Verify thickness with Dektak.

6.11 H_2SO_4:H_2O_2:H_2O_2::1:8:200 : 16 min 30 sec. Selective etch till $In_{0.49}Ga_{0.51}P$, i.e. no change in thickness observed.

6.12 Remove photo resist in Acetone and verify thickness again. Should be 3.2- 3.6 µm

7 Encapsulation with Apiezon W

7.1 Hotplate 135 °C. Place sample that is still attached to the cover slip on hotplate. Remove sample from cover slip.

7.2 Place sample in covered petri dish filled with TCE to clean off the black wax from the back. Handle tweezers with care to prevent scratching the sample.

7.3 Dunk sample in acetone and methanol and N2 blow dry.

7.4 Place a clean glass cover slip on a flat surface and place the sample on top of it

7.5 Using pointed tweezers, place a small piece of black wax on top of the sample. It should not extend beyond the edges of the sample.
7.6 Slowly lift the cover slip with sample and wax on top of it and place on hotplate at 135 °C. Also place a piece of Teflon on the hotplate.
7.7 Allow black wax to melt till it forms a dome. Remove the coverslip with the sample on it and place it on a flat surface. Then take the heated piece of Teflon and touch its plane to the top of the dome. Do not press down. The black wax should stick to the Teflon and the sample can be lifted up.

8 Substrate Removal
8.1 Place Teflon carrier with sample flat at the bottom of the beaker.
8.2 BOE: 1 min (Very important to do this)
8.3 HCl: H2O: 1:1: 1 min.
8.4 H_2SO_4:H_2O_2:H_2O_2:: 1:8:1: 57 min. Monitor after 50 minutes, till the last of the substrate has been etched off to reveal the InGaP layer.
8.5 Concentrated HCl: 20 sec to etch away the InGaP layer of 300 nm. Monitor closely, no more than 25 sec required.

9 Transfer to Transfer diaphragm
9.1 Nudge the interface between the black wax and Teflon with a razor blade till the black wax containing the laser bars pops off.
9.2 Place face down on transfer diaphragm with a drop of water. Place diaphragm in a wafer case.
9.3 Leave in a stationary location for 2 days. Do not place in desiccators.
9.4 Place transfer diaphragm in petri dish and slowly add TCE with a pipette.
9.5 As the Apiezon W starts dissolving remove the solution with a pipette till the samples on the diaphragm look clean.

10 Cleaving and transfer of lasers (This uses Thermal release tape method)
10.1 Cut a circle of thermal release tape the size of the transfer diaphragm. Peel of the protective plastic covering and cut a donut hole into it and stick back on the thermal release tape. This helps in handling the tape.
10.2 Press down exposed sticky center of thermal tape on the thin film laser array and pull back
10.3 Using a smooth round surface, (like the end of a diamond scriber cover) to flex the diaphragm. This will cause cleaves to be generated along the grooves without the lasers peeling off the transfer diaphragm.
10.4 Hotplate 10 s @ 1 20 °C. Press down the tape with tweezers on the hot plate.

10.5 Under a microscope, use a second transfer diaphragm and a drop of water to pick up individual lasers from the transfer diaphragm, and transfer them to a metallized SiO_2/Si substrate.

10.6 Heat on a hotplate for 10 min @ 180 °C.

11 N-stripe: Negative Photolithography, Metallization and Liftoff.

11.1 Spin coat Futurrex NR9-3000 PY with following parameters:

Step	Speed (rpm)	Ramp(rpm/s)	Time(s)
Step 1	500	500	5
Step 2	1600	1600	45
Step 3	0	1000	5

11.2 Prebake on hot plate: 1 min @ 150 °C.

11.3 Suss Microtec MJB3 Mask Aligner, 365 nm, Constant Intensity Control, 9.2mw/cm^2. Run two 5s dummy exposures to stabilize the power.

11.4 Align n-stripe on mask of desired width and correct length with sample. Soft contact.

Expose for 35.89 sec (330 mJ)

11.5 Postbake on hot plate: 1 min @ 100 °C.

11.6 Develop

RD6 Developer, 14 s

Rinse in DI water.

N2 dry.

11.7 De-scum in Asher:

O2 flow to give 6x10-1 mbar

45 sec @ 50 W

11.8 BOE: 1 min

11.9 HCl:H2O::1:1 : 30 sec, place in N2, till ready to metallize

11.10 Metallization

Metal	Thickness (Å)	Deposition Rate (Å/s)
Thermal Evaporation		
AuGe (88%:22%) Alloy	800 Å	1
Electron Beam Evaporation		
Ni	200 Å	1
Au	1000 Å	5

11.11 Place in covered petri dish with acetone for liftoff. Usually takes a while due to the thick resist. Best left overnight.

11.12 RTA on hotplate: 10 s @ 365 °C (Clean room RTA equipment temperature overshoot compromises n-stripe surface)

A.4: SU-8 Waveguide

1 Photomask:

1.1 Straight tapered waveguide: Microtronics Inc. "Thin Film P Ridge N Ridge BA Metal Laser" 12/22/2008. #1664

1.2 Bent tapered waveguide: Microtronics Inc, "Lase_wg_integration_Sept_2--9_ACAD_R" 9/25/2009 # 2559

2 **SU-8 2002 waveguide patterning**

1.1. Dispense only a small quantity of SU-8 2002 onto substrate next to laser. This is to reduce edge bead

1.2. Spin coat with following parameters:

Step	Speed (rpm)	Ramp(rpm/s)	Time(s)
Step 1	300	100	5
Step 2	950	500	45
Step 3	0	500	5

1.3. Hot plate 1 m @ 65 °C

1.4. Hot plate 2 m 30 s @ 95 °C.

1.5. Suss Microtec MJB3 Mask Aligner, 365 nm, Constant Intensity Control, 9.2mw/cm^2. Run two 5s dummy exposures to stabilize the power.

1.6. Align tapered waveguide pattern from mask (dark area reticle) on sample. Hard contact. Place dummy substrate on opposite side of mask to ensure even contact.

1.7. Hot plate 1 m @ 65 °C

1.8. Hot plate 1 m @ 95 °C.

1.9. Develop in
SU-8 developer for 30 s
Dunk in IPA to stop develop.
N_2 blow dry

1.10. Hotplate 30 min @ 180 °C.

Appendix B. Silvaco™ Code

B.1: p-stripe, n-stripe

```
go atlas
#

mesh space.mult=1.0 ^diag.flip width=800 auto
#

# define electrical mesh
x.mesh loc=0 spac=0.5
x.mesh loc=25 spac=0.2
x.mesh loc=30 spac=2.0
x.mesh loc=69.0 spac=2.0

#

y.mesh loc=0.0 spac=0.035
y.mesh loc=0.07 spac=0.55
y.mesh loc=1.17 spac=0.07
y.mesh loc=1.31 spac=0.000255
#y.mesh loc=1.3151 spac=0.005
y.mesh loc=1.32885 spac=0.000375
#y.mesh loc=1.3426 spac=0.005
y.mesh loc=1.3477 spac=0.000255
y.mesh loc=1.4877 spac=0.07
y.mesh loc=2.5877 spac=0.2
y.mesh loc=2.9877 spac=0.2

#Laser structure with doping

region num=1 material=GaAs x.min=0 x.max=69.0 y.min=0.0 y.max=0.07 \
acceptor=1e19

region num=2 material=AlGaAs x.min=0 x.max=69 y.min=0.07 y.max=1.17 \
x.comp=0.74 acceptor=1e18

region num=3 material=GaAs x.min=0 x.max=69 y.min=1.17 y.max=1.31 \
donor=5e15

region num=4 material=GaAsP x.min=0 x.max=69 y.min=1.31 y.max=1.3151 \
y.comp=0.7 calc.strain

region num=5 material=GaAs x.min=0 x.max=69 y.min=1.3151 y.max=1.3426 \
donor=5e15

region num=6 material=GaAsP x.min=0 x.max=69 y.min=1.3426 y.max=1.347 \
y.comp=0.7 calc.strain
```

```
region num=7 material=GaAs x.min=0 x.max=69 y.min=1.3477 y.max=1.4877 \
donor=5e15

region num=8 material=AlGaAs x.min=0 x.max=69 y.min=1.4877 y.max=2.587
\ 7 x.comp=0.74 donor=1e18

region num=9 material=GaAs x.min=0 x.max=69 y.min=2.5877 y.max=2.9877\
donor=5e18

# dimensions of electrodes
elec num=1 name=anode x.min=0 x.max=25 y.min=0 y.max=0
elec num=2 name=cathode x.min=0 x.max=25 y.min=2.9877 y.max=2.9877

interface y.min=0.07 y.max=0.07 thermionic s.s
interface y.min=1.17 y.max=1.17 thermionic s.s
interface y.min=1.31 y.max=1.31 thermionic s.s
interface y.min=1.3151 y.max=1.3151 thermionic s.s
interface y.min=1.3426 y.max=1.3426 thermionic s.s
interface y.min=1.3477 y.max=1.3477 thermionic s.s
interface y.min=1.4877 y.max=1.4877 thermionic s.s
interface y.min=2.5877 y.max=2.5877 thermionic s.s

mqw ww=0.0075 wb=0.01 nwell=1 nbs=2 nx=29 ny=30 \
    xmin=0 xmax=69 ymin=1.314 ymax=1.3437 xcomp=0.8 material=InGaAs \
    yan resolve mc=0.0565 mhh=0.473

save outfile=5llm50pn800um5v.str

material material=InGaAs eg300=1.21 epsinf=13.23 affinity=4.1984 \
alphaa=15000 taun0=1e-9 taup0=1e-8 copt=1.5e-10 fcn=4e-18 fcp=8e-18

material region=1 eg300=1.424 permittivity=12.9 epsinf=10.89 \
affinity=4.07 fcn=4e-18 fcp=8e-18

material region=2 eg300=2.07 NC300=1.612e+19 NV300=1.448e+19
permittivity=10.79 epsinf=8.8698 affinity=3.6824  fcn=4e-18 fcp=8e-18

material region=3 eg300=1.424 NC300=4.57e+17 NV300=9.50e+18 \
permittivity=12.9 epsinf=10.89 affinity=4.07 taun0=1e-9 taup0=2e-8 \
copt=1.5e-10 fcn=4e-18 fcp=8e-18

material region=4 eg300=1.78 NC300=1.04e+18 NV300=8.54e+18 \
permittivity=12.36 epsinf=10.356 affinity=3.892 taun0=1e-9 taup0=1e-8 \
copt=1.5e-10 fcn=4e-18 fcp=8e-18

material region=5 eg300=1.424 NC300=4.57e+17 NV300=9.50e+18 \
permittivity=12.9 epsinf=10.89 affinity=4.07 taun0=1e-9 taup0=2e-8 \
copt=1.5e-10 fcn=4e-18 fcp=8e-18

material region=6 eg300=1.78 NC300=1.04e+18 NV300=8.54e+18
permittivity=12.36 epsinf=10.356 affinity=3.892 taun0=1e-9 taup0=1e-8 \
copt=1.5e-10  fcn=4e-18 fcp=8e-18
```

```
material   region=7   eg300=1.424   NC300=4.57e+17   NV300=9.50e+18   \
permittivity=12.9  epsinf=10.89  affinity=4.07  taun0=1e-9  taup0=2e-8  \
copt=1.5e-10 fcn=4e-18 fcp=8e-18


models fldmob srh optr auger fermi consrh

mobility material=AlGaAs vsatn=4.5e6 vsatp=4.5e6 mun=409.9 mup=128.45
mobility material=GaAsP mun=2296.2 mup=297.2

output band.param con.band val.band u.srh u.radiat u.auger flowlines


solve init
solve vstep=0.05 vfinal=1.0 name=anode
save outfile=5llm50pn800um5v_0.str

# define laser mesh
lx.m x=0 spac=0.4
lx.m x=69 spac=0.4

ly.m y=0.6625 spac=0.1
ly.mesh loc=1.17 spac=0.07
ly.mesh loc=1.31 spac=0.00255
ly.mesh loc=1.3151 spac=0.005
ly.mesh loc=1.3251 spac=0.000375
ly.mesh loc=1.3326 spac=0.005
ly.mesh loc=1.3426 spac=0.00255
ly.mesh loc=1.3477 spac=0.07
ly.m y=1.9877 spac=0.1


models fldmob srh optr auger fermi consrh gainmod=4 print


laser  trap  maxtrap=10  proj  rf=31.3  rr=31.3  maxch=100  absorption  \
losses=5  photon.energy=1.2524  einit=1.24  efinal=1.28  nmodes=32  \
spec.name=5llm50pn800um5v reflect neff=3.367893 toler=0.1 tauss=0.005 \
cavity.length=800  sin=1.7e5  index.model=1  near.nx=100  near.ny=100  \
fcarrier coupled


solve previous

log outf=5llm50pn800um5v.log

method ^las.proj newton

solve vstep=0.02 vfinal=1.1 name=anode
save outfile=5llm50pn800um5v_1.str

solve vstep=0.02 vfinal=1.35 name=anode
save outfile=5llm50pn800um5v_1a.str
```

```
solve vstep=0.02 vfinal=1.51 name=anode
save outfile=5llm50pn800um5v_1aa.str patterns=lm8patthresh

solve vstep=0.01 vfinal=1.61 name=anode
save outfile=5llm50pn800um5v_1b.str patterns=lm8pafterthresh

solve vstep=0.001 vfinal=1.8 name=anode
save outfile=5llm50pn800um5v_2.str

solve vstep=0.02 vfinal=2.5 name=anode
save outfile=5llm50pn800um5v_3.str
```

B.2: p-ridge, n-broad area

```
go atlas
#

mesh space.mult=1.0 diag.flip width=610 auto
#
x.mesh loc=-90 spac=2.0
x.mesh loc=-58 spac=2.0
x.mesh loc=-35 spac=5.0
x.mesh  loc=-10 spac=2
X.mesh loc=0 spac=2
x.mesh  loc=10 spac=2
x.mesh  loc=35 spac=5.0
x.mesh loc=58.0 spac=2.0
x.mesh loc=90.0 spac=2.0

#

y.mesh loc=0.0 spac=0.035
y.mesh loc=0.07 spac=0.55
y.mesh loc=1.17 spac=0.07
y.mesh loc=1.31 spac=0.000255
#y.mesh loc=1.3151 spac=0.005
y.mesh loc=1.32885 spac=0.000375
#y.mesh loc=1.3426 spac=0.005
y.mesh loc=1.3477 spac=0.000255
y.mesh loc=1.4877 spac=0.07
y.mesh loc=2.5877 spac=0.2
y.mesh loc=2.9877 spac=0.2
#
#
region  num=1  material=GaAs  x.min=-90  x.max=90.0  y.min=0.0  y.max=0.07
acceptor=1e19


region  num=2  material=AlGaAs  x.min=-90  x.max=90  y.min=0.07  y.max=1.17
x.comp=0.74 acceptor=1e18
```

```
region num=3 material=GaAs x.min=-90 x.max=90 y.min=1.17 y.max=1.31
donor=5e15

region num=4 material=GaAsP x.min=-90 x.max=90 y.min=1.31 y.max=1.3151
y.comp=0.7 calc.strain

region num=5 material=GaAs x.min=-90 x.max=90 y.min=1.3151 y.max=1.3426
donor=5e15

region num=6 material=GaAsP x.min=-90 x.max=90 y.min=1.3426
y.max=1.3477 y.comp=0.7 calc.strain

region num=7 material=GaAs x.min=-90 x.max=90 y.min=1.3477 y.max=1.4877
donor=5e15

region num=8 material=AlGaAs x.min=-90 x.max=90 y.min=1.4877
y.max=2.5877 x.comp=0.74 donor=1e18

region num=9 material=GaAs x.min=-90 x.max=90 y.min=2.5877 y.max=2.9877
donor=5e18

region num=14 material=Air x.min=-90 x.max=-12.5 y.min=0.0 y.max=1.01

region num=15 material=Air x.min=12.5 x.max=90 y.min=0.0 y.max=1.01


region material=air x.min=-90 x.max=-90 y.min=0 y.max=2.6577

region material=air x.min=90 x.max=90 y.min=0 y.max=2.9877

elec num=1 name=anode x.min=-12.5 x.max=12.5 y.min=0 y.max=0
elec num=2 name=cathode bottom

interface y.min=0.07 y.max=0.07 thermionic s.s
interface y.min=1.17 y.max=1.17 thermionic s.s
interface y.min=1.31 y.max=1.31 thermionic s.s
interface y.min=1.3151 y.max=1.3151 thermionic s.s
interface y.min=1.3426 y.max=1.3426 thermionic s.s
interface y.min=1.3477 y.max=1.3477 thermionic s.s
interface y.min=1.4877 y.max=1.4877 thermionic s.s
interface y.min=2.5877 y.max=2.5877 thermionic s.s

mqw ww=0.0075 wb=0.01 nwell=1 nbs=2 nx=29 ny=30 \
    xmin=-90 xmax=90 ymin=1.314 ymax=1.3437 xcomp=0.8 material=InGaAs \
    yan resolve mc=0.0565 mhh=0.473

save outfile=5l500um5V.str

material material=InGaAs eg300=1.21 epsinf=13.23 affinity=4.1984 \
alphaa=15000 taun0=1e-9 taup0=1e-8 copt=1.5e-10 fcn=4e-18 fcp=8e-18

material region=1 eg300=1.424 permittivity=12.9 \
```

```
epsinf=10.89 affinity=4.07 fcn=4e-18 fcp=8e-18

material   region=2   eg300=2.07   NC300=1.612e+19   NV300=1.448e+19   \
permittivity=10.79 epsinf=8.8698 affinity=3.6824  fcn=4e-18 fcp=8e-18

material   region=3   eg300=1.424   NC300=4.57e+17   NV300=9.50e+18   \
permittivity=12.9  epsinf=10.89  affinity=4.07  taun0=1e-9  taup0=2e-8  \
copt=1.5e-10 fcn=4e-18 fcp=8e-18

material   region=4   eg300=1.78   NC300=1.04e+18   NV300=8.54e+18   \
permittivity=12.36 epsinf=10.356 affinity=3.892 taun0=1e-9 taup0=1e-8 \
copt=1.5e-10 fcn=4e-18 fcp=8e-18

material   region=5   eg300=1.424   NC300=4.57e+17   NV300=9.50e+18   \
permittivity=12.9   epsinf=10.89   affinity=4.07   taun0=1e-9   taup0=2e-8
copt=1.5e-10 fcn=4e-18 fcp=8e-18

material   region=6   eg300=1.78   NC300=1.04e+18   NV300=8.54e+18   \
permittivity=12.36 epsinf=10.356 affinity=3.892 taun0=1e-9 taup0=1e-8 \
copt=1.5e-10  fcn=4e-18 fcp=8e-18

material   region=7   eg300=1.424   NC300=4.57e+17   NV300=9.50e+18   \
permittivity=12.9  epsinf=10.89  affinity=4.07  taun0=1e-9  taup0=2e-8  \
copt=1.5e-10 fcn=4e-18 fcp=8e-18

material    region=8    eg300=2.07    NC300=1.612e+19    NV300=1.448e+19
permittivity=10.79 epsinf=8.8698 affinity=3.6824 fcn=4e-18 fcp=8e-18 \

models fldmob srh optr auger fermi consrh

mobility material=AlGaAs vsatn=4.5e6 vsatp=4.5e6 mun=409.9 mup=128.45
mobility material=GaAsP mun=2296.2 mup=297.2

output band.param con.band val.band u.srh u.radiat u.auger flowlines


solve init
solve vstep=0.05 vfinal=1.0 name=anode
save outfile=5l500um5V_0.str


# define laser mesh
lx.m x=-90 spac=0.5
lx.m x=90 spac=0.5

ly.m y=0.6625 spac=0.1
ly.mesh loc=1.17 spac=0.07
ly.mesh loc=1.31 spac=0.00255
ly.mesh loc=1.3151 spac=0.005
ly.mesh loc=1.3251 spac=0.000375
ly.mesh loc=1.3326 spac=0.005
ly.mesh loc=1.3426 spac=0.00255
ly.mesh loc=1.3477 spac=0.07
```

```
ly.m y=1.9877 spac=0.1

models fldmob srh optr auger fermi consrh gainmod=4 print


# use laser model, define reflectivties, losses and enable absorption
#model, free carrier absorption carrier density dependent refractive
#index, cavity #length, number of transverse modes
# enit, efinal and spec.name used for frequency dependence enabled by
#lmodes

laser trap maxtrap=10 proj rf=31.3 rr=31.3 maxch=100 absorption \
losses=5 photon.energy=1.2524 einit=1.24 efinal=1.28 nmodes=32 \
spec.name=5l500um5V neff=3.367893 toler=0.1 cavity.length=610 sin=1.7e5
\ index.model=1 near.nx=100 near.ny=100 fcarrier coupled


solve previous

log outf=5l500um5V.log

method ^las.proj newton

solve vstep=0.02 vfinal=1.1 name=anode
save outfile=5l500um5V_1.str

solve vstep=0.02 vfinal=1.35 name=anode
save outfile=5l500um5V_1a.str

solve vstep=0.02 vfinal=1.51 name=anode
save outfile=5l500um5V_1aa.str patterns=atthresh

solve vstep=0.001 vfinal=1.61 name=anode
save outfile=5l500um5V_1b.str patterns=afterthresh

solve vstep=0.02 vfinal=1.8 name=anode
save outfile=5l500um5V_2.str

solve vstep=0.02 vfinal=2.5 name=anode
save outfile=5l500um5V_3.str
```

B.3: p-slotted ridge, n-stripe

```
go atlas
#

mesh space.mult=1.0 diag.flip width=800 auto
```

```
# define electrical mesh
x.mesh loc=-90 spac=5.0
x.mesh loc=-58 spac=5.0
x.mesh loc=-32.5 spac=2.0
x.mesh  loc=-10 spac=1
X.mesh loc=0 spac=1.0
x.mesh  loc=10 spac=1
x.mesh  loc=32.5 spac=2.0
x.mesh loc=58.0 spac=5.0
x.mesh loc=90.0 spac=5.0

#

y.mesh loc=0.0 spac=0.035
y.mesh loc=0.07 spac=0.55
y.mesh loc=1.17 spac=0.07
y.mesh loc=1.31 spac=0.000255
#y.mesh loc=1.3151 spac=0.005
y.mesh loc=1.32885 spac=0.000375
#y.mesh loc=1.3426 spac=0.005
y.mesh loc=1.3477 spac=0.000255
y.mesh loc=1.4877 spac=0.07
y.mesh loc=2.5877 spac=0.2
y.mesh loc=2.9877 spac=0.2

# Laser structure with doping


region num=1 material=GaAs x.min=-90 x.max=90.0 y.min=0.0 y.max=0.07
acceptor=1e19

region num=2 material=AlGaAs x.min=-90 x.max=90 y.min=0.07 y.max=1.17
x.comp=0.74 acceptor=1e18

region num=3 material=GaAs x.min=-90 x.max=90 y.min=1.17 y.max=1.31
donor=5e15

region num=4 material=GaAsP x.min=-90 x.max=90 y.min=1.31 y.max=1.3151
y.comp=0.7 calc.strain

region num=5 material=GaAs x.min=-90 x.max=90 y.min=1.3151 y.max=1.3426
donor=5e15

region num=6 material=GaAsP x.min=-90 x.max=90 y.min=1.3426
y.max=1.3477 y.comp=0.7 calc.strain

region num=7 material=GaAs x.min=-90 x.max=90 y.min=1.3477 y.max=1.4877
donor=5e15

region num=8 material=AlGaAs x.min=-90 x.max=90 y.min=1.4877
y.max=2.5877 x.comp=0.74 donor=1e18
```

```
region num=9 material=GaAs x.min=-90 x.max=90 y.min=2.5877 y.max=2.9877
donor=5e18

region num=14 material=SiO2 x.min=-35 x.max=-25 y.min=0.0 y.max=0.98

region num=15 material=SiO2 x.min=25 x.max=35 y.min=0.0 y.max=0.98

region material=Air x.min=-90 x.max=-90 y.min=0 y.max=2.9877

region material=Air x.min=90 x.max=90 y.min=0 y.max=2.9877

# electrodes
elec num=1 name=anode x.min=-20 x.max=20 y.min=0 y.max=0
elec num=2 name=cathode x.min=-20 x.max=20 y.min=2.9877 y.max=2.9877

# define thermionic interfaces
interface y.min=0.07 y.max=0.07 thermionic s.s
interface y.min=1.17 y.max=1.17 thermionic s.s
interface y.min=1.31 y.max=1.31 thermionic s.s
interface y.min=1.3151 y.max=1.3151 thermionic s.s
interface y.min=1.3426 y.max=1.3426 thermionic s.s
interface y.min=1.3477 y.max=1.3477 thermionic s.s
interface y.min=1.4877 y.max=1.4877 thermionic s.s
interface y.min=2.5877 y.max=2.5877 thermionic s.s

# Define parameters for quatum well by using mqw keyword, yan gain
model,

mqw ww=0.0075 wb=0.01 nwell=1 nbs=2 nx=29 ny=30 \
    xmin=-90 xmax=90 ymin=1.314 ymax=1.3437 xcomp=0.8 material=InGaAs \
    yan resolve mc=0.0565 mhh=0.473

save outfile=800um50r98d.str

# material information and loss constants, define high frequency
dielectric
# constants epsinf
material material=InGaAs eg300=1.21 epsinf=13.23 affinity=4.1984
alphaa=15000 \
taun0=1e-9 taup0=1e-8 copt=1.5e-10 fcn=4e-18 fcp=8e-18

material region=1 eg300=1.424 permittivity=12.9 \
epsinf=10.89 affinity=4.07 fcn=4e-18 fcp=8e-18

material region=2 eg300=2.07 NC300=1.612e+19 NV300=1.448e+19 \
permittivity=10.79 epsinf=8.8698 affinity=3.6824  fcn=4e-18 fcp=8e-18

material region=3 eg300=1.424 NC300=4.57e+17 NV300=9.50e+18
permittivity=12.9 \
epsinf=10.89 affinity=4.07 taun0=1e-9 taup0=2e-8 copt=1.5e-10 fcn=4e-18
fcp=8e-18
```

```
material region=4 eg300=1.78 NC300=1.04e+18 NV300=8.54e+18
permittivity=12.36 \ epsinf=10.356 affinity=3.892 taun0=1e-9 taup0=1e-8
copt=1.5e-10 fcn=4e-18 fcp=8e-18

material region=5 eg300=1.424 NC300=4.57e+17 NV300=9.50e+18
permittivity=12.9 \
epsinf=10.89 affinity=4.07 taun0=1e-9 taup0=2e-8 copt=1.5e-10 fcn=4e-18
fcp=8e-18

material region=6 eg300=1.78 NC300=1.04e+18 NV300=8.54e+18
permittivity=12.36 \
epsinf=10.356 affinity=3.892 taun0=1e-9 taup0=1e-8 copt=1.5e-10
fcn=4e-18 fcp=8e-18

material region=7 eg300=1.424 NC300=4.57e+17 NV300=9.50e+18
permittivity=12.9 \
epsinf=10.89 affinity=4.07 taun0=1e-9 taup0=2e-8 copt=1.5e-10 fcn=4e-18
fcp=8e-18

material region=8 eg300=2.07 NC300=1.612e+19 NV300=1.448e+19 \
permittivity=10.79 epsinf=8.8698 affinity=3.6824 fcn=4e-18 fcp=8e-18

material region=9 eg300=1.424 permittivity=12.9 \
epsinf=10.89 affinity=4.07 fcn=4e-18 fcp=8e-18


# define models, field dependent mobility, SRH, Auger, optoelectronic
etc
models fldmob srh optr auger fermi consrh


mobility material=AlGaAs vsatn=4.5e6 vsatp=4.5e6 mun=409.9 mup=128.45
mobility material=GaAsP mun=2296.2 mup=297.2

# specfy output parameters to be logged
output band.param con.band val.band u.srh u.radiat u.auger flowlines

# ramp up voltage before using laser module
solve init
solve vstep=0.05 vfinal=0.8 name=anode
save outfile=800um50r98d_0.str

# define mesh for Helmholtz equation
lx.m x=-90 spac=0.5
lx.m x=90 spac=0.5

ly.m y=0.6625 spac=0.1
ly.mesh loc=1.17 spac=0.07
ly.mesh loc=1.31 spac=0.00255
ly.mesh loc=1.3151 spac=0.005
ly.mesh loc=1.3251 spac=0.000375
ly.mesh loc=1.3326 spac=0.005
ly.mesh loc=1.3426 spac=0.00255
```

```
ly.mesh loc=1.3477 spac=0.07
ly.m y=1.9877 spac=0.1
#

# define models to be uses with the laser model gainmod=4 used with
#quantum wells
models fldmob srh optr auger fermi consrh gainmod=4 print


# use laser model, define reflectivties, losses and enable absorption
#model, free carrier absorption carrier density dependent refractive
#index, cavity #length, number of transverse modes
# enit, efinal and spec.name used for frequency dependence enabled by
#lmodes

laser trap maxtrap=10 proj rf=31.3 rr=31.3 maxch=100 absorption \
losses=10 photon.energy=1.2524 einit=1.24 efinal=1.28 \ nmodes=32
spec.name=800um50r98d neff=3.36 toler=0.1 cavity.length=800 \ sin=1.7e5
index.model=1 near.nx=100 near.ny=100 fcarrier coupled



solve previous

log outf=800um50r98d.log

method ^las.proj newton

solve vstep=0.02 vfinal=1.1 name=anode
save outfile=800um50r98d_1.str

solve vstep=0.02 vfinal=1.35 name=anode
save outfile=800um50r98d_1a.str

solve vstep=0.02 vfinal=1.51 name=anode
save outfile=800um50r98d_1aa.str patterns=atthresh

solve vstep=0.02 vfinal=1.61 name=anode
save outfile=800um50r98d_1b.str patterns=afterthresh

solve vstep=0.02 vfinal=1.8 name=anode
save outfile=800um50r98d_2.str
```

References

[1] S. Hurtt, A. G. Dentai, J. L. Pleumeekers, A. Mathur, R. Muthiah, C. Joyner, R. P. Schneider, R. Nagarajan, F. A. Kish, and D. F. Welch, "The first commercial large-scale InP photonic integrated circuits: current status and performance," in *65th Annu. Dev. Research. Conf.*, 2007, pp. 183-183.

[2] S.-W. Seo, S.-Y. Cho, and N. M. Jokerst, "A thin-film laser, polymer waveguide, and thin-film photodetector cointegrated onto a silicon substrate," *IEEE Photonics Technol. Lett.*, vol. 17, pp. 2197-2199, 2005.

[3] G. Roelkens, J. Brouckaert, S. Verstuyft, J. Schrauwen, D. Van Thourhout, and R. Baets, "Heterogeneous Integration of III-V Photodetectors and Laser Diodes on Silicon-on-Insulator Waveguide Circuits," in *3rd IEEE Int. Conf. Group IV Photon.*, 2006, pp. 188-190.

[4] Y. Liu, "Heterogeneous integration of OE arrays with Si electronics and microoptics," *IEEE Trans. Adv. Packaging.*, vol. 25, pp. 43-49, 2002.

[5] R. Jones, H. D. Park, A. W. Fang, J. E. Bowers, O. Cohen, O. Raday, and M. J. Paniccia, "Hybrid Silicon Integration," *J. Mat. Sci: Mat. in Electron.*, 2007.

[6] D. A. B. Miller, "Rationale and challenges for optical interconnects to electronic chips," *Proc. IEEE,* vol. 88, pp. 728-749, 2000.

[7] S.-Y. Cho, S.-W. Seo, M. A. Brooke, and N. M. Jokerst, "Integrated detectors for embedded optical interconnections on electrical boards, modules, and integrated circuits," *IEEE J. Sel. Top. Quantum Electron.*, vol. 8, pp. 1427-1434, Nov/Dec 2002.

[8] R. E. Kunz, "Miniature integrated optical modules for chemical and biochemical sensing," *Sens. Act. B*, vol. 38, pp. 13-28, 1997.

[9] S.-Y. Cho and N. M. Jokerst, "Integrated Thin Film Photodetectors with Vertically Coupled Microring Resonators for Chip Scale Spectral Analysis," *Appl. Phys. Lett.*, vol. 90, pp. 101105 1-3, 2007.

[10] F. Fixe, V. Chu, D. M. F. Prazeres, and J. P. Conde, "An on-chip thin film photodetector for the quantification of DNA probes and targets in microarrays," *Nucl. Acids Res.*, vol. 32, 2004.

[11] P. Hyungseok, P. L. Likamwa, and H. J. Cho, "Development of planar waveguide based integrated optic SPR (surface plasmon resonance) sensor array," in *QELS*, 2007.

[12] S. K. Selvaraja, D. Vermeulen, M. Schaekers, E. Sleeckx, W. Bogaerts, G. Roelkens, P. Dumon, D. V. Thourhout, and R. Baets, "Highly Efficient Grating Coupler between

Optical Fiber and Silicon Photonic Circuit," in *Conf. Lasers Electro-Opt.*, Baltimore, MD, 2009, p. CTuC6.

[13] J. Bolten, J. Hofrichter, N. Moll, S. Schönenberger, F. Horst, B. J. Offrein, T. Wahlbrink, T. Mollenhauer, and H. Kurz, "CMOS compatible cost-efficient fabrication of SOI grating couplers," *Microelectron. Engg.*, vol. 86, pp. 1114-1116, 2009/6//.

[14] Y. Irie, J. Miyokawa, A. Mugino, and T. Shimizu, "Over 200 mW 980 nm pump laser diode module using optimized high-coupling lensed fiber," in *Optical Fiber Communication Conference, 1999, and the International Conference on Integrated Optics and Optical Fiber Communication. OFC/IOOC '99. Technical Digest*, 1999, pp. 238-240 vol.2.

[15] H. Ghafoori-Shiraz, "Experimental investigation on coupling efficiency between semiconductor laser diodes and single-mode fibres by an etching technique," *Optical Quantum Electron.*, vol. 20, pp. 493-500, 1988.

[16] Z. Jing, P. V. Ramana, J. L. Hon-Shing, Z. Qingxin, J. Chandrappan, T. C. Wei, J. M. Chinq, C. T. W. Liang, and K. D. Lee, "Design and Characterization of Taper Coupler for Effective Laser and Single-Mode Fiber Coupling With Large Tolerance," *IEEE Photonics Technol. Lett.*, vol. 20, pp. 1375-1377, 2008.

[17] M. Kobayashi and K. Kato, "Hybrid optical integration technology," *Electron. Commun. Japan (Part II: Electron.)*, vol. 77, pp. 67-81, 1994.

[18] T. Hashimoto, Y. Nakasuga, Y. Yamada, H. Terui, M. Yanagisawa, K. Moriwaki, Y. Suzaki, Y. Tohmori, Y. Sakai, and H. Okamoto, "Hybrid integration of spot-size converted laser diode on planar lightwave circuit platform by passive alignment technique," *IEEE Photonics Technol. Lett.*, vol. 8, pp. 1504-1506, 1996.

[19] S. Mino, T. Ohyama, Y. Akahori, Y. Yamada, M. Yanagisawa, T. Hashimoto, and Y. Itaya, "10 Gbit/s hybrid-integrated laser diode array module using a planar lightwave circuit (PLC)-platform," *Electron. Lett.*, vol. 32, pp. 2232-2233, 1996.

[20] D.-J. Kim, Y.-T. Han, Y.-J. Park, S.-H. Park, J.-U. Shin, and H.-K. Sung, "Thermal Characteristics of a Laser Diode Integrated on a Silica-Terraced PLC Platform," *ETRI* vol. 27, pp. 337-340, June 2005.

[21] D. V. Plant, M. B. Venditti, E. Laprise, J. Faucher, K. Razavi, M. teauneuf, A. G. Kirk, and J. S. Ahearn, "256-Channel Bidirectional Optical Interconnect Using VCSELs and Photodiodes on CMOS," *J. Lightw. Technol.*, vol. 19, p. 1093, 2001.

[22] T. Hashimoto, Y. Nakasuga, Y. Yamada, H. Terui, M. Yanagisawa, Y. Akahori, Y. Tohmori, K. Kato, and Y. Suzuki, "Multichip Optical Hybrid Integration Technique with Planar Lightwave Circuit Platform," *J. Lightw. Technol.*, vol. 16, p. 1249, 1998.

[23] D. C. Hall, J. N. Holonyak, D. G. Deppe, M. J. Ries, R. J. Matyi, H. Shichijo, and J. E. Epler, "Low-temperature operating life of continuous 300-K Al[sub x]Ga[sub 1 - x]As-GaAs quantum-well heterostructure lasers grown on Si," *J. Appl. Phys.,* vol. 69, pp. 6844-6849, 1991.

[24] T. Yamada, M. Tachikawa, T. Sasaki, H. Mori, and Y. Kadota, "7000 h continuous wave operation of multiple quantum well laser on Si at 50 [degree]C," *Appl. Phys. Lett.,* vol. 70, pp. 1614-1615, 1997.

[25] M. E. Groenert, C. W. Leitz, A. J. Pitera, V. Yang, H. Lee, R. J. Ram, and E. A. Fitzgerald, "Monolithic integration of room-temperature cw GaAs/AlGaAs lasers on Si substrates via relaxed graded GeSi buffer layers," *J. Appl. Phys.,* vol. 93, pp. 362-367, 2003.

[26] J. Liu, X. Sun, R. Camacho-Aguilera, L. C. Kimerling, and J. Michel, "Ge-on-Si laser operating at room temperature," *Opt. Lett.,* vol. 35, pp. 679-681, 2010.

[27] G. Balakrishnan, A. Jallipalli, P. Rotella, H. Shenghong, A. Khoshakhlagh, A. Amtout, S. Krishna, L. R. Dawson, and D. L. Huffaker, "Room-Temperature Optically Pumped (Al)GaSb Vertical-Cavity Surface-Emitting Laser Monolithically Grown on an Si(1 0 0) Substrate," *IEEE J. Sel Top. Quantum Electron.,* vol. 12, pp. 1636-1641, 2006.

[28] L. Cerutti, J. B. Rodriguez, and E. Tournie, "GaSb-Based Laser, Monolithically Grown on Silicon Substrate, Emitting at 1.55 μm at Room Temperature," *IEEE Photonics Technol. Lett.,* vol. 22, April 15 2010.

[29] S. Sakai and N. Wada, "Monolithic III-V light-emitting devices on Si substrates," *Fiber and Integrated Optics,* vol. 13, pp. 31 - 44, 1994.

[30] P. Vettiger, M. K. Benedict, G. L. Bona, P. Buchmann, E. C. Cahoon, K. Datwyler, H. P. Dietrich, A. Moser, H. K. Seitz, O. Voegeli, D. J. Webb, and P. Wolf, "Full-wafer technology-A new approach to large-scale laser fabrication and integration," *IEEE J. Quantum Electron.,* vol. 27, pp. 1319-1331, 1991.

[31] Monocrom. (2010, Aug 3). "Laser Diode Bar Assemblies", Available: http://www.monocrom.com/PDF/LDBA.pdf

[32] Newport Corporation. (2010, August 30). "Laser Diode Lifetime Requirements", Available: http://www.newport.com/servicesupport/Tutorials/default.aspx?id=141#

[33] W. K. Chan, A. Yi-Yan, and T. J. Gmitter, "Grafted semiconductor optoelectronics," *IEEE J. Quantum Electron.,* vol. 27, pp. 717-725, 1991.

[34] I. Christiaens, G. Roelkens, K. D. Mesel, D. V. Thourhout, and R. Baets, "Thin-Film Devices Fabricated With Benzocyclobutene Adhesive Wafer Bonding," *J. Lightw. Technol.,* vol. 23, p. 517, 2005.

[35] H. Wada and T. Kamijoh, "1.3-μm InP-InGaAsP lasers fabricated on Si substrates by wafer bonding," *IEEE J. Sel Top. Quantum Electron.,* vol. 3, pp. 937-942, 1997.

[36] N. M. Jokerst, M. A. Brooke, J. Laskar, D. S. Wills, A. S. Brown, M. Vrazel, S. Jung, Y. Joo, and J. J. Chang, "Microsystem optoelectronic integration for mixed multisignal systems," *IEEE J. Sel. Top. Quantum Electron.,* vol. 6, pp. 1231-1239, 2000.

[37] S. Blokhin, A. Sakharov, N. Maleev, A. Kuz'menkov, I. Novikov, N. Gordeev, Y. Shernyakov, M. Maximov, V. Ustinov, A. Kovsh, S. Mikhrin, N. Ledentsov, G. Lee, and J. Chi, "Experimental study of temperature dependence of threshold characteristics in semiconductor VCSELs based on submonolayer InGaAs QDs," *Semiconductors,* vol. 40, pp. 1232-1236, 2006.

[38] L. A. D'Asaro, J.-F. Seurin, and J. D. Wynn, "High-power, high effciency VCSELs pursue the goal," in *Photonics Spectra*. vol. 39: Laurin Publishing, 2005, pp. 62-66.

[39] J. H. Shin, B. S. Yoo, W. S. Han, O. K. Kwon, Y. G. Ju, and J. H. Lee, "CW operation and threshold characteristics of all-monolithic InAlGaAs 1.55-μm VCSELs grown by MOCVD," *IEEE Photonics Technol. Lett.,* vol. 14, pp. 1031-1033, 2002.

[40] H. Riechert, A. Ramakrishnana, and G. Steinle, "Development of InGaAsN-based 1.3 um VCSELs," *Semicond. Sci. Technol.,* vol. 17, p. 892, 2002.

[41] R. Pu, C. Duan, and C. W. Wilmsen, "Hybrid integration of VCSELs to CMOS integrated circuits," *IEEE J. Sel Top. Quantum Electron.,* vol. 5, pp. 201-208, 1999.

[42] R.-H. Horng and D.-S. Wuu, "Wafer-Bonded 850-nm Vertical-Cavity Surface-Emitting Lasers on Si Substrate with Metal Mirror," *Jpn. J. Appl. Phys,* vol. 41, pp. 5849-5852, 2002.

[43] S. Matsuo, K. Tateno, T. Nakahara, H. A. T. H. Tsuda, and T. A. K. T. Kurokawa, "Use of polyimide bonding for hybrid integration of a vertical cavity surface emitting laser on a silicon substrate," *Electron. Lett.,* vol. 33, pp. 1148-1149, 1997.

[44] J. H. Choi, L. Wang, H. Bi, and R. T. Chen, "Effects of Thermal-Via Structures on Thin-Film VCSELs for Fully Embedded Board-Level Optical Interconnection System," *IEEE J. Sel. Top. Quantum Electron.,* vol. 12, pp. 1060-1065, 2006.

[45] T. Y. Kondo, S. Kitamura, Y. Nimura, T. A. K. T. Kaneko, and T. A. S. T. Shimoda, "Thin film VCSEL assembly on CMOS IC using ELO and nano paste metallization," in *2004 Dig. LEOS Summer Topical Meetings*, pp. 11-12.

[46] J. M. Perkins, T. L. Simpkins, C. Warde, and J. C. G. Fonstad, "Full Recess Integration of Small Diameter Low Threshold VCSELs within Si-CMOS ICs," *Opt. Exp.,* vol. 16, pp. 13955-13960, 2008.

[47] Bookham Inc. (2010, August 30). "850 nm High power multimode VCSELs", Available: http://www.bookham.com/datasheets/vcsels/vcsels_850_high_power.cfm

[48] U-L-M Photonics. (2010, August 30). "12mW / 24mW VCSEL SMA Receptacle / Chip", Available: http://www.ulm-photonics.com/docs/products_new/datasheets/VCSEL-ULM-TO56-SMA-12mW.pdf

[49] Princeton Optronics Inc. (2010, August 30). "60 W Pulsed Multi-Mode 975 nm VCSEL Single Device", Available: http://www.princetonoptronics.com/pdfs/PSP-CS-60-W0975.pdf

[50] M. Grabherr, M. Miller, R. Jaeger, D. Wiedenmann, and R. King, "Commercial VCSELs reach 0.1-W cw output power " in *Proc. SPIE 5364*, 2004, pp. 174-182.

[51] RPMC Lasers. (2008, August 30). "Multimode Single Emitters Specifications", Available: http://www.rpmclasers.com/Multimode%20Single%20Emitter%20Diode%20Lasers.htm

[52] A. W. Fang, H. Park, O. Cohen, R. Jones, M. J. Paniccia, and J. E. Bowers, "Electrically pumped hybrid AlGaInAs-silicon evanescent laser," *Opt. Exp.*, vol. 14, pp. 9203-9210, 2006.

[53] S.-W. Seo, S.-Y. Cho, and N. M. Jokerst, "Integrated thin film InGaAsP laser and 1x4 polymer multimode interference splitter on silicon," *Opt. Lett.*, vol. 32, pp. 548-550, 2007.

[54] D. Tauber, M. Horita, J. Piprek, P. Abraham, J. A. L. Holmes, and J. E. Bowers, "The Microstrip Laser," *IEEE Photonics Technol. Lett.*, vol. 10, pp. 478-480, 1998.

[55] H.-F. Kuo, S.-Y. Cho, J. Hall, and N. M. Jokerst, "InP/InGaAsP MQW thin film edge emitting lasers for embedded waveguide chip to chip optical interconnections," in *16th Annu. Meeting Lasers and Electro-Optics Soc.*, 2003, pp. 63-64.

[56] H.-H. Chang, A. W. Fang, M. N. Sysak, H. Park, R. Jones, O. Cohen, O. Raday, M. J. Paniccia, and J. E. Bowers, "1310 nm silicon evanescent laser," *Opt. Exp.*, vol. 15, pp. 11466-11470, 2007.

[57] Y. H. Lo, R. Bhat, D. M. Hwang, C. Chua, and C. H. Lin, "Semiconductor lasers on Si substrates using the technology of bonding by atomic rearrangement," *Appl. Phys. Lett.*, vol. 62, pp. 1038-1040, 1993.

[58] E. Yablonovitch, E. Kapon, T. J. Gmitter, C. P. Yun, and R. Bhatt, "Double heterostructure GaAs/AlGaAs thin film diode lasers on glass substrates," *IEEE Photonics Technol. Lett.*, vol. 1, pp. 41-42, 1989.

[59] X. Ji, J. Cai, F.-s. Choa, X. Wang, J. Diep, and T. Le, "Thin-film double-side heat removal laser diodes," in *Conf. Lasers Electro-Opt.*, 2005, pp. 559-561.

[60] J. C. Fan, K. Y. Chen, G. Lin, and C. P. Lee, "Stripe-geometry GaAs-InGaAs laser diode with back-side contact on silicon by epitaxial liftoff," *Electron. Lett.,* vol. 33, pp. 1094-1095, 1997.

[61] J. Fan, C. Tsai, K. Chen, S. Wang, G. Lin, and C. Lee, "Low-resistance vertical conduction across epitaxially lifted-off n-GaAs film and Pd/Ge/Pd coated Si substrate," *J. Electron. Mat.,* vol. 27, pp. 110-113, 1998.

[62] A. W. Fang, H. Park, Y.-H. Kuo, R. Jones, O. Cohen, D. Liang, O. Raday, M. N. Sysak, M. J. Paniccia, and J. E. Bowers, "Hybrid Silicon evanescent devices," *Materials Today,* vol. 10, pp. 28-35, July 1 2007.

[63] J. J. Rumpler and C. G. Fonstad, "Continuous-Wave Electrically Pumped 1.55-μm Edge-Emitting Platelet Ridge Laser Diodes on Silicon," *IEEE Photonics Technol. Lett.,* vol. 21, pp. 827-829, 03 April 2009.

[64] I. Pollentier, L. Buydens, P. V. Daele, and P. Demeester, "Fabrication of a GaAs-AlGaAs GRIN-SCH SQW laser diode on silicon by epitaxial lift-off," *IEEE Photonics Technol. Lett.,* vol. 3, pp. 115-117, 1991.

[65] S.-Y. Cho, S. Palit, D. Xu, G. Tsvid, N. Jokerst, L. Mawst, and T. Kuech, "Strain Compensated InGaAs/GaAsP Single Quantum Well Thin Film Lasers Integrated onto Si Substrates," in *20th Annu. Meeting IEEE Lasers Electro-Optics Soc.*, Orlando, FL, 2007, pp. 829-830.

[66] R. G. Hunsperger, A. Yariv, and A. Lee, "Parallel end-butt coupling for optical integrated circuits," *Appl. Opt.,* vol. 16, pp. 1026-1032, 1977.

[67] H. Bissessur, C. Graver, O. L. Gouezigou, G. Michaud, and F. Gaborit, "Ridge Laser with Spot-Size Converter in a Single Epitaxial Step for High Coupling Efficiency to Single-Mode Fibers," *IEEE Photonics Technol. Lett.,* vol. 10, pp. 1235-1237, 1998.

[68] P. M. DeDobbelaere, F. Vermaerke, G. Vermeire, P. Demeester, P. VanDaele, G. R. Moehlmann, J.-L. P. Heideman, and W. H. G. Horsthuis, "Integration technology for light-source arrays with polymeric optical waveguide arrays," in *Proc. SPIE 2285*, 1994, pp. 352-359.

[69] M. Yanagisawa, H. Terui, K. Shuto, T. Miya, and M. Kobayashi, "Film-level hybrid integration of AlGaAs laser diode with glass waveguide on Si substrate," *IEEE Photonics Technol. Lett.,* vol. 4, pp. 21-23, 1992.

[70] G. Roelkens, D. Van Thourhout, R. Baets, R. Nötzel, and M. Smit, "Laser emission and photodetection in an InP/InGaAsP layer integrated on and coupled to a Silicon-on-Insulator waveguide circuit," *Opt. Exp.,* vol. 14, pp. 8154-8159, 2006.

[71] M. N. Sysak, H. Park, A. W. Fang, J. E. Bowers, R. Jones, O. Cohen, O. Raday, and M. J. Paniccia, "Experimental and theoretical thermal analysis ofa Hybrid Silicon Evanescent Laser," *Opt. Exp.*, vol. 15, pp. 15041-15046, 2007.

[72] T. Chen, T. Hong, J.-Q. Pan, W.-X. Chen, Y.-B. Cheng, Y. Wang, X.-B. Ma, W.-L. Liu, L.-J. Zhao, G.-Z. Ran, W. Wang, and G.-G. Qin, "Electrically Pumped Room-Temperature Pulsed InGaAsP-Si Hybrid Lasers Based on Metal Bonding," *Chin. Phys. Lett.*, vol. 26, p. 064211, 2009.

[73] A. W. Fang, E. Lively, Y.-H. Kuo, D. Liang, and J. E. Bowers, "A distributed feedback silicon evanescent laser," *Opt. Exp.*, vol. 16, pp. 4413-4419, 2008.

[74] B. E. Saleh and M. C. Teich, *Fundamanetals of Photonics*: Wiley-Interscience, 1991.

[75] T. A. DeTemple and C. M. Herzinger, "On the semiconductor laser logarithmic gain-current density relation," *IEEE J. Quantum Electron.*, vol. 29, pp. 1246-1252, 1993.

[76] K. Y. Lau, "Ultralow threshold quantum well lasers," in *Quantum Well Lasers*, J. Peter S. Zory, Ed. San Diego, CA: Academic Press, Inc., 1993, p. 504.

[77] T. R. Chen, B. Zhao, L. Eng, J. A. Feng, Y. H. Zhuang, and A. Yariv, "Parametric study of cavity length and mirror reflectivity in ultralow threshold quantum well InGaAs/AlGaAs lasers," *Electron. Lett.*, vol. 31, pp. 285-287, 1995.

[78] O. Hess, S. W. Koch, and J. V. Moloney, "Filamentation and beam propagation in broad-area semiconductor lasers," *IEEE J. Quantum Electron.*, vol. 31, pp. 35-43, 1995.

[79] K. J. Beernink, J. J. Alwan, and J. J. Coleman, "Antiguiding in narrow stripe gain-guided InGaAs-GaAs strained-layer lasers," *J. Appl. Phys.*, vol. 69, pp. 56-60, 1991.

[80] C. Shieh, J. mantz, H. Lee, D. Ackley, and R. Egelmann, "Anomalous dependencce of threshold current on stripe width in gain guided strained-layer InGaAs/GaAsquantum we;; ;asers," *Appl. Phys. Lett.*, vol. 54, pp. 2521-2523, 1989.

[81] J. J. Coleman, "Strained Layer Quantum Well Heterostructure Lasers," in *Quantum Well Lasers*, J. Peter S. Zory, Ed. San Diego, CA: Academic Press, Inc., 1993, p. 504.

[82] P. Bhattacharya, *Semiconductor Optoelelectronic Devices*. Delhi: Pearson Education, 1997.

[83] M. Achtenhagen and A. Hardy, "Lateral current spreading in ridge waveguide laser diodes," *Appl. Phys. Lett.*, vol. 74, pp. 1363-1365, 1999.

[84] N. Tansu, J.-Y. Yeh, and L. J. Mawst, "Extremely low threshold-current-density InGaAs quantum-well lasers with emission wavelength of 1215--1233 nm," *Appl. Phys. Lett.*, vol. 82, pp. 4038-4040, 2003.

[85] N. K. Dutta, W. S. Hobson, D. Vakhshoori, H. H. A.-H. Han, P. N. F. A.-P. N. Freeman, J. F. d. J. A.-J. F. d. Jong, and J. L. A.-J. Lopata, "Strain compensated InGaAs-GaAsP-InGaP laser," *IEEE Photonics Technol. Lett.*, vol. 8, pp. 852-854, 1996.

[86] M. Sagawa, T. Toyonaka, K. Hiramoto, K. Shinoda, and K. Uomi, "High-power highly-reliable operation of 0.98-μm InGaAs-InGaP strain-compensated single-quantum-well lasers with tensile-strained InGaAsP barriers," *IEEE J. Sel Top. Quantum Electron.*, vol. 1, pp. 189-194, 1995.

[87] M. D. Feit and J. J. A. Fleck, "Light propagation in graded-index optical fibers," *Appl. Opt.*, vol. 17, pp. 3990-3998, 1978.

[88] R. Scarmozzino, A. Gopinath, R. Pregla, and S. Helfert, "Numerical techniques for modeling guided-wave photonic devices," *IEEE J. Sel Top. Quantum Electron.*, vol. 6, pp. 150-162, 2000.

[89] Silvaco, "ATLAS User's Manual," Santa Clara: Silvaco, 2008.

[90] J. Piprek, *Semiconductor Optoelectronic Devices - Introduction to Physics and Simulation*. San Diego: Academic Press, 2003.

[91] I. Vurgaftman, J. R. Meyer, and L. R. Ram-Mohan, "Band parameters for III--V compound semiconductors and their alloys." vol. 89: AIP, 2001, pp. 5815-5875.

[92] T. Ishikawa and J. E. Bowers, "Band lineup and in-plane effective mass of InGaAsP or InGaAlAs on InP strained-layer quantum well," *Quantum Electronics, IEEE Journal of,* vol. 30, pp. 562-570, 1994.

[93] M. Levinstein, S. Rumyantsev, and M. Shur, *Elementary Semiconductors and A3B5 compounds* vol. 1. London: World Scientific 1999.

[94] M. Levinstein, S. Rumyantsev, and M. Shur, *Ternary and quaternary III-V compounds* vol. 2. London: World Scientific 1999.

[95] M. Huang, "MS Project Report: Analysis and Simulation of Strain Compensated InGaAs Laser," Duke University, Durham, NC2008.

[96] P. G. Eliseev, "Stripe-geometry lasers and their properties," *Czechoslovak J. Phys.*, vol. 30, pp. 300-317, 1980.

[97] K. Gurnett and T. Adams, "Ultra-thin semiconductor wafer applications and processes," *III-Vs Review,* vol. 19, pp. 38-40, 2006.

[98] C. Landesberger, S. Scherbaum, and K. Bock, "Carrier techniques for thin wafer processing," in *CSMantech Conf.* Austin, TX, 2007, pp. 33-36.

[99] B. E. Schmidt, S. Mohrdiek, and C. S. Harder, "Pump Laser Diodes," in *Optical Fiber Telecommunications IV-A: Components (Optics and Photonics)*. vol. IV-A, I. Kaminow and T. Li, Eds.: Elsevier Academic Press, 2002, pp. 1-876.

[100] L. F. Feng, D. Li, C. Y. Zhu, C. D. Wang, H. X. Cong, X. S. Xie, and C. Z. Lu, "Simultaneous sudden changes of electrical behavior at the threshold in laser diodes," *J. Appl. Phys.*, vol. 102, p. 063102, 2007.

[101] G. Zhang, M. Pessa, and D. Ahn, "Gain Characteristics of Strained-Layer InGaAs/GaAs Quantum Well Lasers," *physica status solidi (b),* vol. 176, pp. K75-K79, 1993.

[102] N. Shomura, M. Fujimoto, and T. Numai, "Fiber Pump Semiconductor Lasers With Optical Antiguiding Layers for Horizontal Transverse Modes," *IEEE J. Quantum Electron.*, vol. 44, pp. 819-825, 2008.

[103] C. H. Gao, H. Y. Ong, W. J. Fan, and S. F. Yoon, "Analysis of optical gain and threshold current density of 980 nm InGaAs/GaAs compressively strained quantum well lasers," *Computational Mat. Sci.,* vol. 30, pp. 296-302, 2004.

[104] (2008, August 24). "TexLoc refractive index of polymers", Available: http://www.texloc.com/closet/cl_refractiveindex.html

[105] R. S. Stein and R. S. Finkelstein, "Optical Properties of Polymers." vol. 24, 1973, pp. 207-234.

[106] J. E. Mark, *Physical Properties of Polymers Handbook*: Springer, 2006.

[107] S.-Y. Cho, G. Dobbs, N. Jokerst, B. Mizaikoff, and T. Cooper, "Optical microring resonator sensors with selective membrane surface customization," in *Proc. 6th IEEE Conf. Sensors*, 2007.

[108] L. Luan, R. D. Evans, N. M. Jokerst, and R. B. Fair, "Integrated optical sensor in a digital microfluidic platform," *IEEE Sens. J,* vol. 8, pp. 628-635, May 2008.

[109] S.-Y. Cho and N. Jokerst, "A polymer microdisk photonic sensor integrated onto silicon," *IEEE Phot. Tech. Lett.*, vol. 18, pp. 2096-2098, September 2006.

[110] A. Yalcin, K. C. Popat, J. C. Aldridge, T. A. Desai, J. Hryniewicz, N. Chbouki, B. E. Little, O. King, V. Van, S. Chu, D. Gill, M. Anthes-Washburn, and M. S. Unlu, "Optical sensing of biomolecules using microring resonators," *IEEE J. Sel Top. Quantum Electron,* vol. 12, pp. 148-155, Jan/Feb 2006.

[111] K. D. Vos, I. Bartolozzi, E. Schacht, P. Bienstman, and R. Baets, "Silicon-on-insulator microring resonator for sensitive and label-free biosensing," *Opt. Expr.,* vol. 15, pp. 7610-7615, 2007.

[112] S.-Y. Cho and N. M. Jokerst, "Polymer Microrings Integrated with Thin Film InGaAs MSM Photodetectors for Sensor-On-a-Chip Applications," in *IPRM*, Princeton, NJ, 2006, pp. 222-225.

[113] M. A. Thomas, J. Lillie, K. Dae-Ik, S. Ralph, N. Jokerst, M. Brooke, K.Dennis, B. Comeau, and C. L. Henderson, "An interferometric sensor for integration with Si CMOS signal processing circuitry: Sensor on a Chip," in *Conf. Lasers and Electro-opt.* San Francisco, CA, 2004.

[114] B. J. Luff, J. S. Wilkinson, J. Piehler, U. Hollenbach, J. Ingenhoff, and N. Fabricius, "Integrated optical Mach-Zehnder biosensor," *J. Lightwave. Tech.*, vol. 16, pp. 583-592, April 1998.

[115] N. Fabricius, G. Gauglitz, and J. Ingenhoff, "A gas sensor based on an integrated optical Mach-Zehnder interferometer," *Sens. Act. B*, vol. 7, pp. 672-676, 1992.

[116] P. Rabiei, W. Steier, C. Zhang, and L. Dalton, "Polymer micro-ring filters and modulators," *J. Lightwave. Tech.*, vol. 20, pp. 1968-1975, November 2002.

[117] R. Marie, S. Schmid, A. Johansson, L. E. Ejsing, M. Nordstrom, D. Hafliger, C. B. V. Christensen, A. Boisen, and M. Dufva, "Immobilisation of DNA to polymerised SU-8 photoresist," *Biosensors & Bioelectronics*, vol. 21, pp. 1327-1332, January 2006.

[118] B. Yang, L. Yang, R. Hu, Z. Sheng, D. Dai, Q. Liu, and S. He, "Fabrication and Characterization of Small Optical Ridge Waveguides Based on SU-8 Polymer," *J. Lightw. Technol.*, vol. 27, pp. 4091-4096, 2009.

[119] J. I. Pankove, *Optical processes in semiconductors*. New York: Dover Publications Inc., 1975.

[120] J. Jiménez, "Laser diode reliability: crystal defects and degradation modes," *Comptes Rendus Physique*, vol. 4, pp. 663-673, 2003/8//.

[121] Y. Jeong, M. Shindo, M. Akabori, and T.-k. Suzuki, "Epitaxial Lift-Off of InGaAs/InAlAs Metamorphic High Electron Mobility Heterostructures and Their van der Waals Bonding on AlN Ceramic Substrates," *Applied Physics Express*, vol. 1, p. 021201, 2008.

[122] P. Dudley, J. Kirch, T. Garrod, S. Kim, L. Mawst, K. Radavich, S. Ruder, T. Kuech, S. Palit, and N. Jokerst, "InxGa1-xAs Metamorphic Buffer Layers for Lattice Mismatched Multi-Junction Solar Cells," in *Electron. Mat. Conf.* Notre Dame Indiana., 2010.

[123] O. Moutanabbir and U. GÃ¶sele, "Heterogeneous Integration of Compound Semiconductors." vol. 40, pp. 469-500.

[124] C. E. Zah, R. Bhat, B. Pathak, C. Caneau, F. J. Favire, N. C. Andreadakis, D. M. Hwang, M. A. Koza, C. Y. Chen, and T. P. Lee, "Low threshold 1.5 μm tensile-strained single quantum well lasers," *Electron. Lett.*, vol. 27, pp. 1414-1416, 1991.

[125] Z. Huang, R. Scarmozzino, G. Nagy, J. Steel, and R. M. J. Osgood, "Realization of a compact and single-mode optical passive polarization converter," *IEEE Photonics Technol. Lett.,* vol. 12, pp. 317-319, 2000.

[126] Y. Shani, R. Alferness, T. Koch, U. Koren, M. Oron, B. I. Miller, and M. G. Young, "Polarization rotation in asymmetric periodic loaded rib waveguides," *Appl. Phys. Lett.*, vol. 59, pp. 1278-1280, 1991.

[127] J.-J. Kim, W.-Y. Hwang, M.-C. Oh, and S.-Y. Shin, "TE-TM polarization converters based on electro-optic poled polymer," *Proc. SPIE* vol. 2527, pp. 397-403, 1995.

[128] M. Kotlyar, L. Bolla, M. Midrio, L. O'Faolain, and T. Krauss, "Compact polarization converter in InP-based material," *Opt. Express,* vol. 13, pp. 5040-5045, 2005.

[129] C. Li, "Complete polarization conversion using one crystal with dual transverse Pockels effect," *Appl. Opt.,* vol. 47, pp. 2241-2251, 2008.

Biography

Sabarni Palit was born in Pune, Maharashtra, India, on December 5, 1978. She received her Bachelor of Engineering Degree in Electronics and Telecommunications Engineering from MKSSS' Cummins College of Engineering for Women, University of Pune, in 2000, and a Master of Science Degree in Electrical and Computer Engineering from Rose-Hulman Institute of Technology, Terre Haute, Indiana in 2003, specializing in Photonic Systems. She joined the doctoral program in the Department of Electrical and Computer Engineering, Duke University, Durham, NC in 2005, where she also obtained an MS specializing in terahertz metamaterials, in 2008.

Journal Publications

[1] **S. Palit**, J. Kirch, M. Huang, L. Mawst, N. M. Jokerst, "Facet Embedded Thin Film III-V Edge Emitting Lasers Integrated with SU-8 Waveguides on Silicon" *Opt. Lett*, 2010 (accepted).

[2] **S. Palit**, J. Kirch, L. Mawst, T. Kuech, N. M. Jokerst, "Thermal Characteristics of III/V Thin Film Edge Emitting Lasers on Silicon" Intr. J. Microwave. Opt. Tech., 2010 (submitted).

[3] **S. Palit**, J. Kirch, G. Tsvid, L. Mawst, T. Kuech, N. M. Jokerst, "Low Threshold Thin Film III-V Lasers Bonded to Silicon with Front and Back Side Defined Features" Opt. Lett., vol. 34, 2802-2804, Sep 2009.

[4] T. Driscoll, H. T. Kim, B. G. Chae, Y. W. Lee, B. J. Kim, N. M. Jokerst, **S. Palit**, D. R. Smith, M. Di Ventra, D. N. Basov, "Memory Metamaterials" Science, vol. 325, 1518 – 1521, Sep 2009.

[5] N. Jokerst, L. Luan, **S. Palit**, M. Royal, S. Dhar, M. Brooke, T. Tyler, "Progress in Chip-Scale Photonic Sensing," IEEE Transactions on Bio Circuits and Systems (BioCAS), vol. 3, 202-211, Aug 2009.

[6] N. Jokerst, M. Royal, **S. Palit**, L. Luan, S. Dhar, and T. Tyler, "Chip scale integrated microresonator sensing systems," J. Biophoton., vol. 2, 212-226, 2009.

[7] Y. Yuan, C. Bingham, T. Tyler, **S. Palit**, T. H. Hand, W. J. Padilla, N. M. Jokerst, and S. A. Cummer, "A dual-resonant terahertz metamaterial based on single-particle electric-field-coupled resonators" Appl. Phys. Lett., vol 93, 191110, 2008.

[8] H-T. Chen, **S. Palit**, T. Tyler, C. M. Bingham, J. M. O. Zide, J. F. O'Hara, D. R. Smith, A. C. Gossard, R. D. Averitt, W. J. Padilla, N. M. Jokerst, and A. J. Taylor, "Hybrid metamaterials enable fast electrical modulation of freely propagating terahertz waves" Appl. Phys. Lett., vol. 93, 091117, 2008.

[9] Y. Yuan, C. Bingham, T. Tyler, **S. Palit**, T. H. Hand, W. J. Padilla, D. R. Smith, N. M. Jokerst, and S. A. Cummer, "Dual-band planar electric metamaterial in the terahertz regime," Opt. Express, vol. 16, 9746-9752, 2008.

[10] T. Driscoll, **S. Palit**, M.M. Qazilbash, M.Brehm, F. Keilmann, B. G. Chae, H.-T. Kim, S.Y. Cho, N. Jokerst, D. Smith, D.N. Basov, "Dynamic tuning of an infrared hybrid-metamaterial resonance using vanadium dioxide," Appl. Phys. Lett., vol. 93, 024101, 2008.

[11] T. Driscoll, G.O. Andreev, D. Basov, **S. Palit**, S.Y. Cho, N.M. Jokerst, D.R. Smith, "Tuned Permeability in Terahertz Split-Ring Resonators for devices and sensors" Appl. Phys. Lett., vol. 91, 062511, 2007.

[12] T. Driscoll, G. O. Andreev, D. N. Basov , **S. Palit**, T. Ren, J. Mock, S.-Y. Cho, N. M. Jokerst, and D. R. Smith. "Quantitative investigation of a terahertz artificial magnetic resonance using oblique angle spectroscopy", Appl. Phys. Lett., vol. 90, 092508, 2007.

[13] **S. Palit**, M. Jaeger, S. Granieri, B. Black, J. Chestnut and A. Siahmakoun , "5-bit programmable Binary and Ternary Architectures for an optical transmit/receive beamformer", IEICE Trans Electron., vol. E86-C, 7, July 2003.

[14] Conference Presentations with Proceedings or Digests

[15] **S. Palit**, J. Kirch, L. Mawst, N. M. Jokerst, "Thin Film lasers Embedded in Passively Aligned SU8 Waveguides on SiO2/Si" in Conf. on Lasers and Electro-optics, Optical Society of America, CWP5, San Jose, CA, USA, May 16-21, 2010.

[16] (Invited) N. Jokerst, **S. Palit**, J. Kirch, G. Tsvid, L. Mawst, T. Kuech, "Thin Film III-V Edge Emitting Lasers Integrated Onto Silicon," in SPIE Photon. West, San Francisco, CA, USA, Jan 25-28, 2010.

[17] **S. Palit**, J. Kirch, L. Mawst, T. Kuech and N. M. Jokerst, "Heterogeneous integration of thin-film compound semiconductor lasers and Su-8 waveguides on SiO2/Si", in SPIE Photon. West, San Francisco, CA, Jan 25-28, 2010.

[18] **S. Palit**, J. Kirch, L. Mawst, T. Kuech, and N. Jokerst, "Thin Film P-Ridge N-Stripe III-V Laser Broad Area Metal-Metal Bonded to Silicon," in Conf. on Lasers and Electro-Optics/International Quantum Electronics Conf., OSA Technical Digest (Optical Society of America, 2009), JWA38, Baltimore, MD, USA, June1-5, 2009.

[19] **S. Palit**, G. Tsvid, J. Kirch, Juno Yu-Ting Huang, L. Mawst, T. Kuech, N. M. Jokerst, "Broad area metal/metal bonding of thin film edge emitting lasers to silicon," in 21st Ann. Mtng. of the IEEE Lasers and Electro-Optics Society, 123-124, Newport Beach, CA, USA, Nov 9-13, 2008.

[20] **S. Palit**, G. Tsvid, J. Kirch, J. Y.-T. Huang, T. Tyler, S.-Y. Cho, N. Jokerst, L. Mawst, and T. Kuech, "Top-Bottom Stripe Thin Film InGaAs/GaAsP Laser integrated on Silicon," in IEEE Device Research Conf., 137-138, Santa Barbara, CA, USA, June 23-25, 2008.

[21] T. H. Hand, Y. Yuan, **S. Palit**, C. Bingham, M. Rahm, D. R. Smith, W. J. Padilla, N. Jokerst, and S. A. Cummer, "Dual-Band Planar Electric THz Metamaterial with Resonator Yield Analysis," in Conf. on Lasers and Electro-Optics/Quantum Electron. and Laser Sci. Conf. and Photonic Applications Systems Tech., OSA Technical Digest (Optical Society of America, 2008), JWA56, San Jose, CA, USA, May 4-9, 2008.

[22] (Invited) N. M. Jokerst, S-Y. Cho, L. Luan, M. Royal, and **S. Palit**," Chip scale integrated microresonators for sensing applications", Proc. SPIE Photon. West, 6872, 68720Q, San Jose, CA, USA, Jan 19-24, 2008.

[23] S-Y. Cho, **S. Palit**, D. Xu, G. Tsvid, N. Jokerst, L. Mawst, T. Kuech, "Strain Compensated InGaAs/GaAsP Single Quantum Well Thin Film Lasers Integrated onto Si Substrates" in 20th Ann. Mtng. of the IEEE Lasers and Electro-Optics Society, 829-830, Lake Buena Vista, FL, USA, Oct 21-25, 2007.

[24] **S. Palit**, T. Driscoll, T. Ren, J Mock, Sang-Yeon Cho, N. M. Jokerst, D. Smith, D Basov, "Toward Artificial Magnetism Using Terahertz Split Ring Resonator Metamaterials" in 19th Ann. Mtng. of the IEEE Lasers and Electro-Optics Society, 248-249, Montreal, Canada, Oct 29-Nov 2, 2006.

[25] B. A. Black, S. Granieri, M. Jaeger, **S. Palit**, A. Siahmakoun, and D. Thelen, "A ternary programmable dispersion matrix for receive/transmit optical beamforming," Proc. SPIE Photonics North 2003 Conf., 5260, 16-21, Montreal, Canada, May 25-29, 2003.

[26] **S. Palit**, S. Granieri, A. Siahmakoun, and B. A. Black, "Performance characteristics of a 5-bit optical receive beamformer", Proc. SPIE Photonics North 2002 Conf., 4833, 348-353, Quebec City, Canada, Jun 2-6, 2002.

[27] **S. Palit**, S. Granieri, A. Siahmakoun, B. Black, K. Johnson and J. Chestnut, "Binary and ternary architectures for a two-channel 5-bit optical receive beamformer", Tech. Digest of

International Topical Mtng. on Microwave Photonics (MWP), IEEE, 273-276. Awaji, Japan, Nov 5-8, 2002.

Other Conference Presentations

[28] (Invited) **S. Palit**, "Integration of thin film compound semiconductor edge emitting lasers on silicon substrates" in CMOS Emerging Technologies Workshop, Whistler, BC, Canada, May 19-21, 2010.

[29] **S. Palit**, J. Kirch, L. Mawst, T. Kuech and N. M. Jokerst, "Integration of III/V Thin Film Ed ge Emitting Lasers on Silicon", 12th International Symposium on Microwave and Optical Technology, New Delhi, India, Dec 16-19, 2009.

[30] (Invited) N. M. Jokerst, L. Luan, M. Royal, **S. Palit**, T. Tyler, M. A. Brooke, "Chip Scale Integrated Photonic Sensing Systems", 14th IEEE Int. Mixed Signals, Sensors and System Testing Workshop, Vancouver, Canada, June 18-20, 2008.

[31] T. Driscoll, **S. Palit**, M. Qazilbash, M. Brehm, F. Keilmann, B. Chae, H. Kim, D. Basov, N. M. Jokerst, D. Smith, "Hybrid metamaterials for dynamic tuning," 2008 APS March Meeting, New Orleans, LA, USA, Mar 10–14, 2008.

[32] G. Andreev, T. Driscoll, D. Basov, M. Diventra, **S. Palit**, S. Y. Cho, N. M. Jokerst, D. Smith, "Tuned permeability in terahertz split-ring resonators for devices and sensors," 2008 APS March Meeting, New Orleans, LA, USA, Mar 10–14, 2008.

[33] T. Driscoll , **S. Palit** , W. Padilla , T. Ren , J. Mock , G. Andreev , S-Y. Cho , N. M. Jokerst , D. Smith , D. Basov, "A spectroscopic multi-angle probe of metamaterial permeability" 2007 APS March Meeting, Denver, CO, USA, Mar 5–9, 2007.